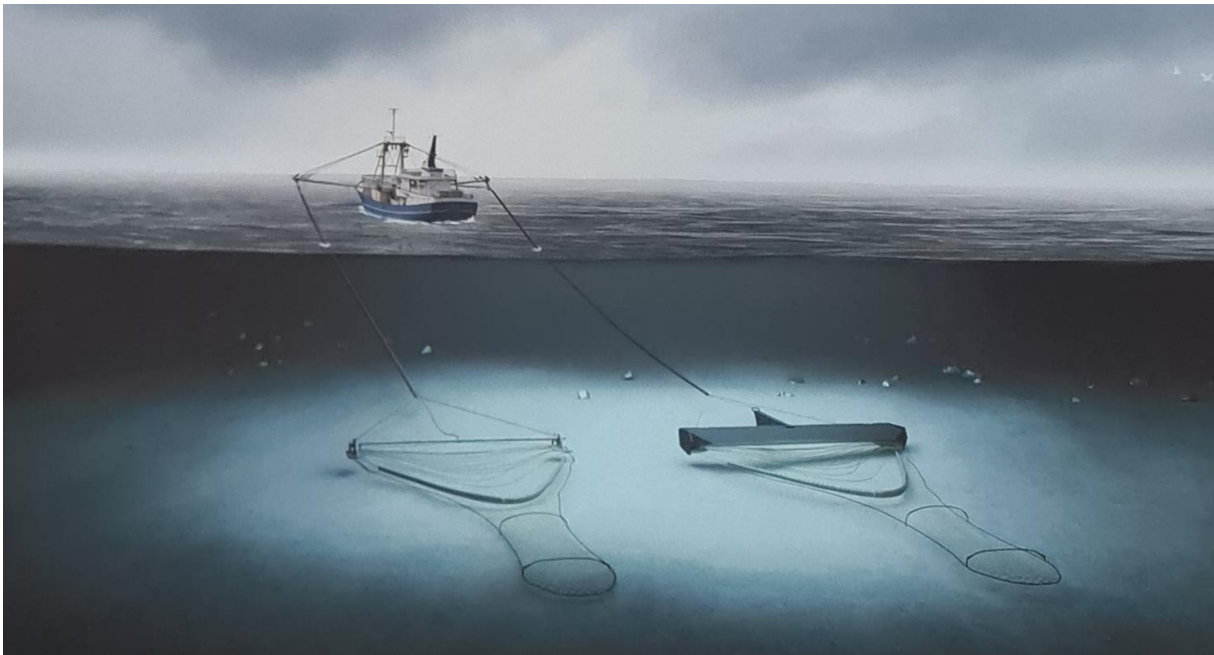


Understanding of the resistance of tickler chains of beam trawl fishing



Course code: OE54030
Course name: Thesis
Student name: ing. N.J. Koorn
Student number: 4331826
Supervisor: dr. ir. G.H. Keetels

Preface

This report represents the results of my graduation project in the field of beam trawl fishery, within the master Offshore & Dredging Engineering. Questions that came up from the literature are being researched by experiments that are done at TU Delft.

I would like to thank Geert Keetels for his guidance, Bithin Ghorai for his knowledge on soil mechanics, assistance with the experiment and additional guidance, Sape Miedema for his explanation on cutting theories, André van den Bosch and Ed Stok for their technical support for the experiment, VIC for the experiments that are done in Stellendam and VUC for the explanation of the fishermen's point of view. Furthermore I would like to thank my family, especially my father and grandfather, for their support and interest during the process.

The Hague, April 2023

Table of contents

Preface	2
Table of contents	3
Abstract	6
List of figures and tables	7
Nomenclature	11
Introduction.....	13
Part I	14
1. Beam trawl fishing	15
2.2. Multiple tickler chains	17
2.3. Penetration depth	18
2.4. Fish behaviour	19
3. Fishing gear experiments.....	20
3.1. Chain experiment.....	20
3.2. Demersal fishing gears	21
3.3. Overview.....	23
4. Numerical model.....	24
5. Hydrodynamic drag.....	26
6. Consolidation	27
7. Plate anchors.....	28
8. Offshore pipelines.....	31
8.1. Influence of the relative density.....	31
8.2. Influence of the dilatancy angle.....	32
9. Laterally loaded piles	33
9.1. Bearing capacity	33
9.2. Influence of internal friction angle	35
9.3. Effect of scaling	36
10. Ploughing	37
10.1. Plough with a forecutter.....	37
10.2. Ploughing experiments.....	40
10.3. Multi-blade plough.....	40
11. Cutting in sand	42
11.1. Dry sand.....	42
11.2. Saturated sand.....	43
11.3. Wedge theory.....	44

12.	Further approach based on the literature.....	50
12.1.	Conclusions from literature.....	50
12.2.	Further approach.....	51
12.3.	Expectations	51
Part II	52
13.	Experimental design.....	53
13.1.	Goal	53
13.2.	Setup	53
13.3.	Process.....	58
13.4.	Force sensors	58
13.5.	Parameters	59
13.6.	Reference case	63
14.	Results.....	64
14.1.	Force calculation	64
14.2.	Comparisons with respect to the reference case	66
14.3.	Additional comparisons	74
14.3.	Differences between the three chains	77
14.4.	Final calibration	79
15.	Comparison with theories.....	82
15.1.	Ploughing theory	82
15.2.	Cutting theory.....	83
15.3.	Consolidation	85
15.4.	Influence of the internal friction angle	85
16.	Dimensionless forces	87
17.	Conclusion and discussion	92
	Bibliography.....	93
	Appendix I: Soil mechanical scaling.....	95
	Appendix II: Mapping of the density of silica sands	96
	Appendix III: Cutting coefficients.....	97
	Appendix IV: Water pressure forces and grain forces	101
	Appendix V: Scaling laws.....	103
	V.1. Reynolds scaling.....	103
	V.2. Froude scaling	103
	V.3. Peclet scaling	104
	Appendix VI: Overview of the experiment	105
	Appendix VII: Technical data sand.....	108

Appendix VIII: Technical data force sensor	110
Appendix IX: Drawings of the setup	111
Appendix X: Additional plots front chain	113
Appendix XI: Consolidation and confining pressure calculations	118

Abstract

The electric pulse fishing technique is no longer an option for fishermen. Therefore, they have to fall back on beam trawl fishing. This method has several disadvantages such as high fuel consumption and much soil disturbance. This system therefore deserves an investigation into improvement.

There is various literature on interaction of offshore structures with the soil. Processes in which a structure is also towed through the seabed are ploughing and cutting. Experiments with tickler chains are done and also numerical models are created.

Experiments were performed to acquire the required information that could not be retrieved from literature. In these experiments a chain element is towed through a sand layer in various configurations in a controlled way. Parameters that are varied are: velocity, chain link diameter, angle of attack, density, grain size.

A decrease of the angle of attack leads to a decrease of the tow force. The force per unit length is defined by dividing the tow force by the projected length. The projected length perpendicular to the towing direction, decreases for a decrease of angle of attack. However, the force per unit length also decreases for a decrease of the angle of attack. That means that the projected length is not the only explanation for the decrease in force.

The experiments indicate that the forces for higher penetration depths and higher chain link diameters are very high. An increase of density leads to a significant increase of the internal friction angle for low confining pressures. The increase of the internal friction angle leads to a higher passive soil pressure coefficient. The increase of this coefficient can certify the high forces.

Two dimensionless parameters are defined: the dimensionless force and the Froude number. An estimate for the increase of the passive pressure coefficient is integrated in the dimensionless force to clarify the high values for dense soil. After plotting the experimental results expressed in these dimensionless parameters, a linear trend line representing the data with reasonable accuracy of $R^2 = 0.611$.

List of figures and tables

Figure 1: Schematic view of the beam trawl system (Bruns, 2020)	15
Figure 2: Tickler chains and the ground rope as applied by the Visserij Coöperatie Urk (VCU)	16
Figure 3: Depletion rate against penetration depth for different types of fishing gear (Rijnsdorp & e.a., Assessing and mitigating impact of bottom trawling, 2017)	17
Figure 4: Percentage of total catch against number of tickler chains for sole (Creutzberg, Duineveld, & Noort, 1987)	17
Figure 5: Percentage of total catch against number of tickler chains for common dab. left for sand and right for mud (Creutzberg, Duineveld, & Noort, 1987)	18
Figure 6: Modelled beam trawl system (Depestele & e.a., 2016)	18
Figure 7: Schematic view of the test setup for the Sintef experiment	20
Figure 8: Test setup with long linked chain (Enerhaug, 2011).....	20
Figure 9: Dimensionless force plotted against the angle of attack (Enerhaug, 2011)	21
Figure 10: Gear components on the rod (Ivanovic & e.a., 2015).....	22
Figure 11: The mean drag force for an otter-door model plotted against the towing velocity for three different penetration depths (Ivanovic & e.a., 2015).....	22
Figure 12: Drag force for different angles of attack	23
Figure 13: Dimensionless force against dimensionless weight for two different gear shapes	24
Figure 14: Dimensionless force against dimensionless penetration depth for two different gear shapes	25
Figure 15: Degree of consolidation, where c_v is indicated by c on the x-axis (Verruijt, 2006).	27
Figure 16: Strength versus the confining pressure (Bolton, The strength and dilatancy of sands, 1986)	29
Figure 17: Pipe geometry with uplift resistance P , diameter D , penetration depth H and unit weight γ' (White, Cheuk, & Bolton, 2008).....	31
Figure 18: The normalised peak uplift resistance versus the (normalised) burial depth for different relative densities for fixed values of critical internal friction angle, natural logarithm of the grain-crushing strength Q and unit weight (submerged example) (White, Cheuk, & Bolton, 2008).....	31
Figure 19: The normalised soil resistance against the normalised burial depth for different dilatancy angles (Guo & Stolle, Lateral pipe-soil interaction in sand with reference to scale effect, 2005)	32
Figure 20: Schematic view of a axial (H) and lateral (V) loaded pile with diameter D (Foglia & Ibsen, 2014)	33
Figure 21: Bearing capacity against normalised depth (Foglia & Ibsen, 2014)	34
Figure 22: Soil pressure coefficients against the internal friction angle (Miedema, 2014)	35
Figure 23: Plough model of Lauder (Lauder, Brown, Bransby, & Boyes, 2013).....	37
Figure 24: Tow force against the plough velocity (Lauder, Brown, Bransby, & Boyes, 2013)	39
Figure 25: Dimensionless form of the rate effect.....	39
Figure 26: Test setup for ploughing experiments (Lauder, 2010).....	40
Figure 27: Different views of the multi-blade plough (Rhee & Steeghs, 1991)	40
Figure 28: Tow force against plough velocity for different penetration depths (Rhee & Steeghs, 1991).....	41
Figure 29: The shear type cutting mechanism (Miedema, 2014)	42
Figure 30: The flow type cutting mechanism (Miedema, 2014)	42

Figure 31: The shear type cutting mechanism including a wedge (Miedema, 2014)	45
Figure 32: Forces acting on the layer cut including a wedge for the dry sand case (Miedema, 2014).....	45
Figure 33: Forces acting on the wedge for the dry sand case (Miedema, 2014)	46
Figure 34: The forces acting on the layer cut including a wedge for the saturated sand case (Miedema, 2014)	48
Figure 35: The forces acting on the wedge for the saturated sand case (Miedema, 2014) ...	48
Figure 36: Beam trawl system at model scale	53
Figure 37: Schematic front view of the chain holder in the flume	54
Figure 38: Total overview of the setup (figure by B. Ghorai)	55
Figure 39: Schematic top view of the setup (figure by B. Ghorai)	56
Figure 40: Three chain holders with different chain link diameters.....	57
Figure 41: Picture of the experimental setup in the Waterlab.....	57
Figure 42: The wooden plate that is used to level the sandbed	58
Figure 43: Towing the chain at an angle of 60 degrees with respect to the towing direction .	60
Figure 44: Three different chain link diameters, from top to bottom: 16 mm, 10 mm, 6 mm ..	61
Figure 45: Definitions of penetration depth h_i and chain link height h_b	62
Figure 46: Forces for the case with rotated chains	64
Figure 47: The projected length of the chain.....	65
Figure 48: Force versus time different velocities in loose sand (test 1, 2 and 3)	66
Figure 49: Normal force versus time for different angles of attack (test 2d, 14b and 15c)	67
Figure 50: Force versus time for different angles of attack (test 2, 14 and 15)	68
Figure 51: Force per unit length versus time for different angles of attack (test 2, 14 and 15)	69
Figure 52: Force versus time for different chain link diameters (test 2 and 12)	70
Figure 53: Force versus time for additional penetration depth (test 2, 5 and 6).....	71
Figure 54: Loose versus dense for the fine grain (test 2 and 17)	72
Figure 55: Fine versus coarse grain for loose sand (test 2d and 22e).....	73
Figure 56: Force versus time for presence and absence of a chain (test 2 and 23)	74
Figure 57: Force versus velocity of attack for different chain link diameters (test 2 and 12a-g) in loose soil	75
Figure 58: Force against angle of attack for different chain link diameters (test 2, 12h-k, 14, 15) in loose soil	75
Figure 59: Force per unit length versus time for different angles of attack for the sixteen millimeter chain (test 12a,b,h-k).....	76
Figure 60: Force against velocity for two different density cases (test 2 and 17).....	77
Figure 61: Tow forces for the individual chains in dense sand (test 17g)	78
Figure 62: Calibration setup.....	79
Figure 63: Calibration of the sensors at the back.....	80
Figure 64: Calibration of the sensors at the middle.....	80
Figure 65: Calibration of the sensors at the front	81
Figure 66: Plough force versus plough velocity for two chain link diameters, experimental data (test 1, 2, 3 and 12) and ploughing theory	82
Figure 67: Plough force versus penetration depth, experimental data (test 2, 5 and 6) and ploughing theory for a velocity of 0.3 m/s.....	83
Figure 68: The tow force against the tow velocity for different chain link diameters, experimental data (test 1, 2, 3 and 12) and cutting theory	84

Figure 69: The tow force against the penetration depth for the experimental data (test 2, 5 and 6) and the cutting theory for a velocity of 0.3 m/s.....	84
Figure 70: Pressure coefficients versus internal friction angle	85
Figure 71: The tow force against the tow velocity for different chain link diameters, experimental data (test 1, 2, 3 and 12) and cutting theory for an internal friction angle of 50°	86
Figure 72: The tow force against the penetration depth, experimental data (test 2, 5 and 6) and cutting theory for an internal friction angle of 50°	86
Figure 73: Definition in 2D of the beam of soil that needs to be removed	88
Figure 74: Dimensionless force versus the Froude number for experimental data (test 1, 2, 3, 5, 6, 12, 17, 22)	89
Figure 75: Dimensionless force versus the Froude number for experimental data (test 1, 2, 3, 5, 6, 12, 17, 22)	90
Figure 76: Dimensionless force versus the Froude number corrected with passive pressure coefficient for experimental data (test 1, 2, 3, 5, 6, 17, 22)	91
Figure 77: Dimensionless force versus the Froude number corrected with passive pressure coefficient for experimental data (test 1, 2, 3, 5, 6, 17, 22)	91
Figure 78: Horizontal cutting force coefficient for $h_b/h_i = 2$ (Miedema, 2014).....	97
Figure 79: Vertical cutting force coefficient for $h_b/h_i = 2$ (Miedema, 2014).....	98
Figure 80: Horizontal cutting force coefficient for inertia effects (Miedema, 2014)	98
Figure 81: Vertical cutting force coefficient for inertia effects (Miedema, 2014).....	99
Figure 82: Overview of the setup (drawing by B.A. van den Bosch).....	111
Figure 83: Chain holder (drawing by B.A. van den Bosch).....	111
Figure 84: Chain connected to the chain holder (drawing by B.A. van den Bosch)	112
Figure 85: Figure 9: Force versus time for different velocities in loose sand	113
Figure 86: Force versus time for different velocities in dense sand.....	113
Figure 87: Figure 9: Force versus time for different angles of attack.....	114
Figure 88: Force versus time for the 16 mm chain	114
Figure 89: Force versus time for additional penetration depth	115
Figure 90: Loose versus dense for the fine grain	115
Figure 91: Loose versus dense for the coarse grain	116
Figure 92: Fine versus coarse grain for loose sand	116
Figure 93: Fine versus coarse grain for dense sand	117

Table 1: Modelled penetration depths for different chain link diameters (Depestele & e.a., 2016).....	19
Table 2: Overview of parameters and whether or not they are varied within the experiment.....	23
Table 3: Values for the tow coefficients (Cathie & Wintgens, 2001)	38
Table 4: Dimensions of the setup	56
Table 5: Position of the force sensors.....	59
Table 6: Masses for chain parts including strips for each chain link diameter	61
Table 7: Initial penetration depths for different chain link diameters.....	62
Table 8: Overview of different parameters and corresponding tests	63
Table 9: Reference case	63
Table 10: Differences between the three chains	77
Table 11: Parameters and corresponding units	87

Table 12: Scale factors (Lauder, 2010).....	95
Table 13: Relative density and cone resistance (Lauder, 2010).....	96
<i>Table 14: Minimum value of the consolidation coefficient for both chain link diameters</i>	<i>118</i>
<i>Table 15: Maximum value of the consolidation coefficient for both chain link diameters</i>	<i>118</i>
Table 16: Minimum and maximum value for the confining pressure.....	118

Nomenclature

Symbol	Quantity
A	area
B	foundation width
c	cohesion
C_D	drag coefficient
C_d	dynamic rate effect coefficient
C_{dn}	dimensionless rate effect coefficient
C_i	non-cavitating cutting coefficient
C_s	dimensionless passive pressure coefficient
C_v	coefficient dependent on d_{10} and relative density
C_w	dimensionless friction coefficient
D	diameter
D_c	hydrodynamic drag force per unit length
D_L	longitudinal hydrodynamic dispersion coefficient
d	displacement
d_i	cavitating cutting coefficient
d'	depth of excavation
E	elasticity modulus
e	void ratio
F	force
Fr	Froude number
f_i	contribution of the inertia force to the total force
G_1	weight of the layer cut
G_2	weight of the wedge
g	gravitational constant
H	embedment / burial depth / penetration depth
h	height of the soil
h_b	blade height
h_i	initial layer thickness / penetration depth
I	Inertial force on the shear plane
I_f	displacement influence factor
I_D	relative density index
I_R	relative dilatancy index
K_a	active soil pressure coefficient
K_p	passive soil pressure coefficient
K_1	grain force on the shear plane
K_2	grain force on the pseudo blade
K_3	gran force on the bottom of the wedge
K_4	grain force on the blade
k	permeability
L	length
m_c	amount of mobilized sediment
N	bearing capacity factor
N_h	maximum dimensionless force, bearing capacity factor
n_e	effective porosity for advection
Pe	Peclet number
p'	confining pressure
p'_f	mean effective confining pressure at failure
p_{1m}	average pore pressure on the shear zone
p_{2m}	average pore pressure on the pseudoblade
p_{4m}	average pore pressure on the blade

Q	natural logarithm of the grain-crushing strength
q_u	bearing capacity
Re	Reynolds number
S	dilation potential
s	shape factor
s_f	silt fraction
U	velocity in x-direction
V	velocity
V_c	cutting velocity
V_D	Darcy velocity
W_1	pore pressure force on the shear plane
W_2	pore pressure force on the pseudo blade
W_3	pore pressure force on the bottom of the wedge
W_4	pore pressure force on the blade
w	width of the blade
α	blade angle
α_a	angle of attack
β	shear angle
γ	unit weight of the soil
γ'	effective unit weight of the soil
δ	soil/steel interface / external friction angle
δ_e	mobilized effective external friction angle
ε	volume strain
θ	wedge angle
λ	angle of internal friction between wedge and layer cut
λ_i	dimensionless inertial effect parameter
λ_{iD}	cutting force coefficient for direction i
λ_{il}	cutting force coefficient for direction i
ν	kinematic viscosity
ρ	density
φ	angle of internal friction
φ'_p	peak friction angle
φ'_c	critical state friction angle
ψ	dilatancy angle

Abbreviation Meaning

NIOZ	Koninklijk Nederlands Instituut voor Onderzoek der Zee (English: Royal Netherlands Institute for Sea Research)
TU Delft	Technisch Universiteit Delft
VCU	Visserij Coöperatie Urk
VIC	Visserij Innovatie Centrum

Introduction

The electric pulse fishing technique has been getting more and more discredited these days. On 15 April 2021 the Court of Justice of the European Union pronounced a ban on this method in the European Union (Penca, 2022). About 79 Dutch cutters make use of the electric pulse fishing technique (Totaalverbod op pulsvisserij kan vissers duizenden euro's per jaar kosten, 2021). These fishermen need to return to the 'old-fashioned' beam trawl catch system, using tickler chains instead of electric pulses, which results in a lower financial net result. The beam trawl system has disadvantages such as high fuel consumption and much soil disturbance.

For improving the beam trawl method, it is necessary to understand the physics involved. This research focusses on the friction forces caused by towing one or multiple layer through the sandbed and the influence of different (soil) parameters. The research questions are:

- What kind of research on this topic has already been done in the past?
- Which theories from literature could be compared with towing the chains through a sand layer?
- Which parameters influence the tow force and if they do, what influence do they have?

Part I is about literature on this topic and similar theories. In the literature review, first a description of the beam trawl fishing system is given. Then a numerical model and some experiments that are done on this topic are described. the hydrodynamical part of beam trawl fishing is described. Then the focus is more shifted to the soil mechanical part of beam trawl fishing. Different insights from other offshore engineering disciplines related to structure-soil interaction are studied. Theories about static offshore structures like plate anchors, buried pipelines and piles are described to understand soil parameters that could influence the tow force. Dynamic processes like ploughing and cutting / dredging theories are described to get an idea of the force and which parameters are related to it.

Part II is about the experiment that followed on the conclusions of part I. First details on the setup and the test procedure are described, followed by the results. Than a comparison will be made with ploughing and cutting theory and a dimension analysis will be done, followed by conclusions and discussion.

Part I

1. Beam trawl fishing

In the beam trawl fishing method a system of tickler chains is used to mobilise the fish. The system consists of a funnel shaped net which is towed next to the fishing vessel. A beam is attached at the aperture of the net. At both ends of the beam a so-called shoe is attached, carrying a system of chains. (Boomkor, 2022) These chains are towed through the upper layer of the seabed to stimulate the fish to leave the seabed and be caught by the net provided that the sailing velocity is sufficiently high. An impression of this system can be seen in Figure 1.

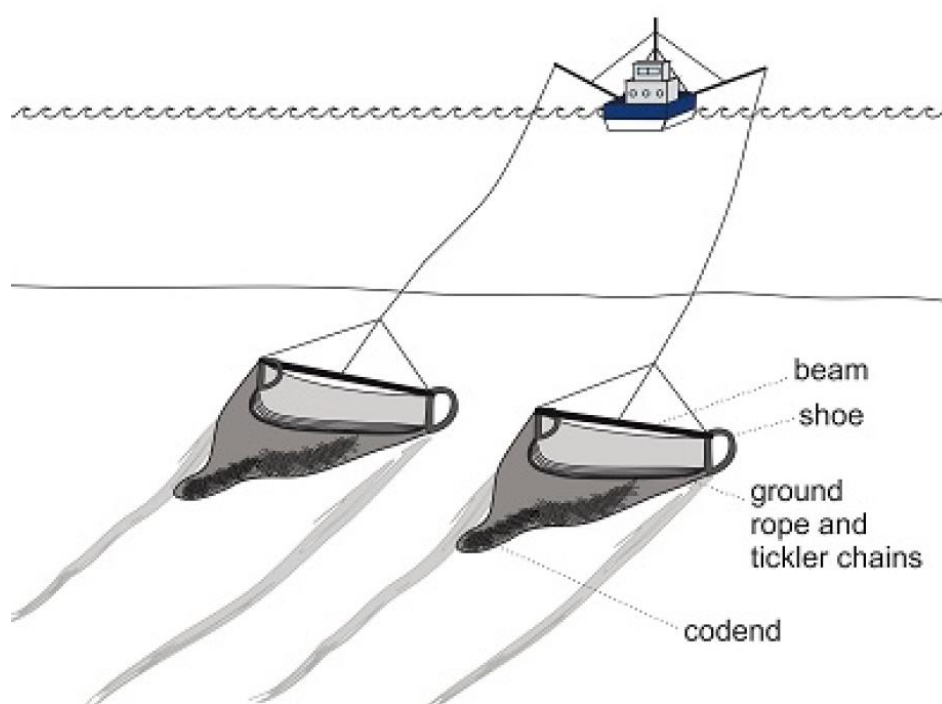


Figure 1: Schematic view of the beam trawl system (Bruns, 2020)

In Figure 2 an example of the tickler chains and the ground rope at the Visserij Coöperatie Urk (VCU) is shown.

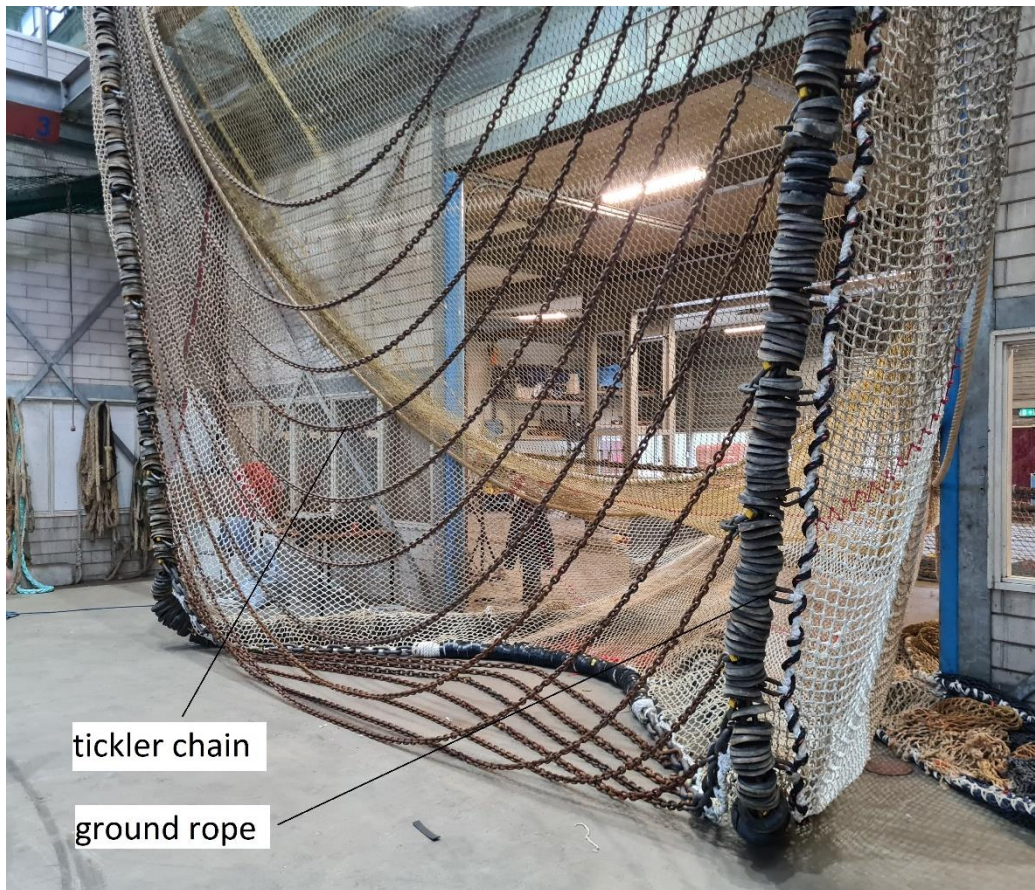


Figure 2: Tickler chains and the ground rope as applied by the Visserij Coöperatie Urk (VCU)

Tickler chains can be divided in two subcategories: shoe ticklers and net ticklers. Shoe ticklers are connected to the shoes at the end of the beam. Net ticklers are connected to the ground gear or footrope of the net (Rijnsdorp & e.a., Sediment mobilization by bottom trawls: a model approach applied to the Dutch North Sea beam trawl fishery, 2021).

The beam trawl method has several disadvantages. The fuel consumption is very high, typically 30,000-35,000 l a week, due to the physical interaction with the soil, while pulse fishing has decreased the fuel consumption with 37-49% (Marlen, Wiegerinck, Os-Koomen, & Barneveld, 2012). Increasing fuel prices aggravates this disadvantage, the seabed is largely impacted due to the soil interaction with the tickler chains (Enerhaug, 2011), leading to ecological disturbance. An increase of penetration depth leads to a higher depletion rate (mortality) of benthos as shown in Figure 3 (OT = otter door, BT = beam trawl, TD = dredges, HD = hydraulic dredges) (Rijnsdorp & e.a., Assessing and mitigating impact of bottom trawling, 2017).

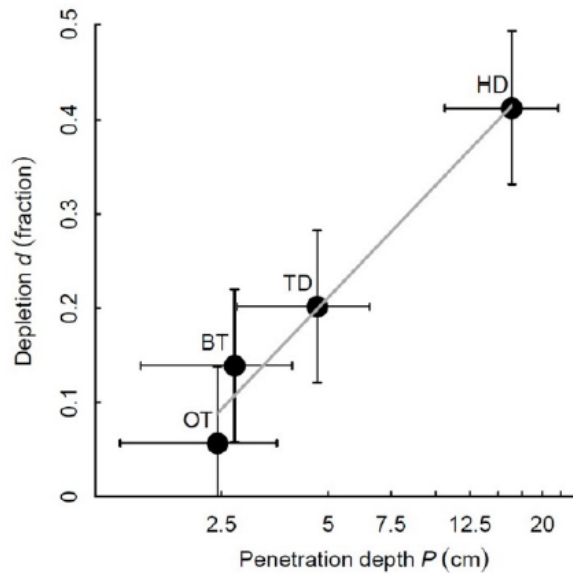


Figure 3: Depletion rate against penetration depth for different types of fishing gear (Rijnsdorp & e.a., *Assessing and mitigating impact of bottom trawling*, 2017)

2.2. Multiple tickler chains

The Royal Netherlands Institute for Sea Research (NIOZ) conducted a study on the effect of the different numbers of tickler chains according to the total catch (Creutzberg, Duineveld, & Noort, 1987). In Figure 4 the percentage of total catch for one specific species per 10,000 m² is plotted against the number of tickler chains for sole (*Solea solea*) with a seabed of sand. Increasing the number of tickler chains leads to a higher percentage of total catch for the specific species.

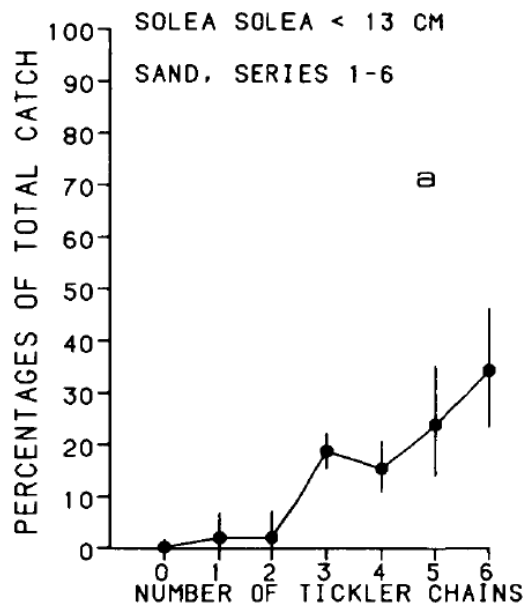


Figure 4: Percentage of total catch against number of tickler chains for sole (Creutzberg, Duineveld, & Noort, 1987)

For the common dab (*Limanda limanda*) a comparison is made for both a sandy seabed as well as a muddy seabed. In sandy seabed a similar trend as for the sole can be seen. Whereas in muddy seabed, increasing the number of tickler chains seems to be disadvantageous, as the percentage of total catch for the specific species decreases as shown in Figure 5. The mud disturbances might cause this effect according to NIOZ.

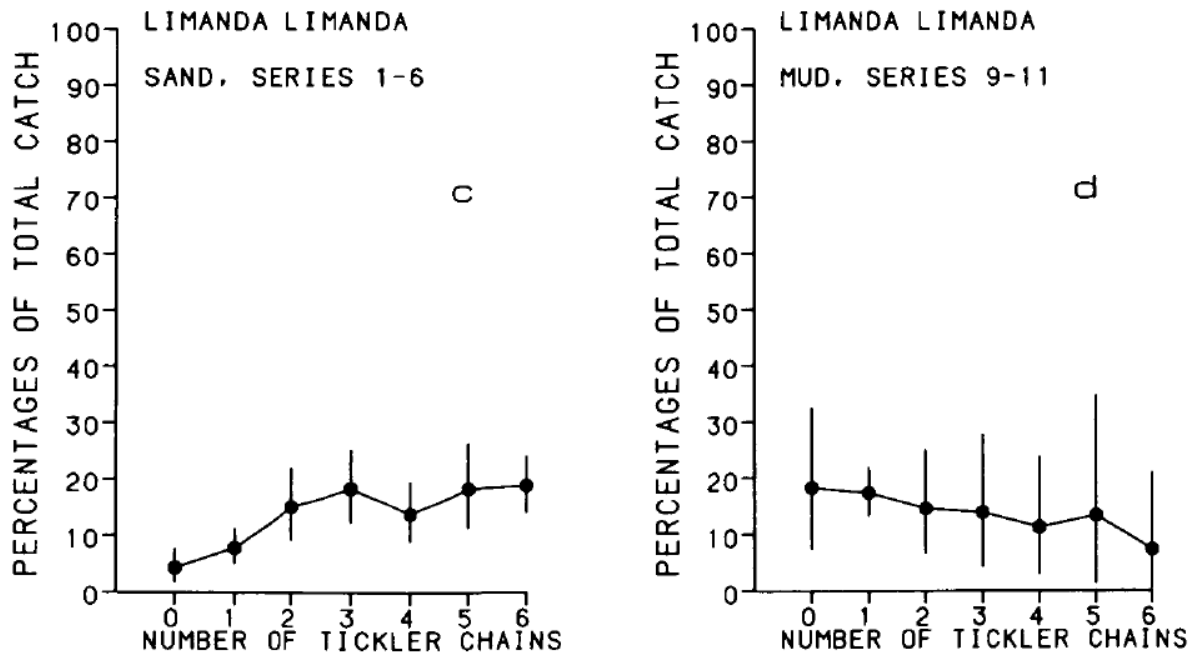


Figure 5: Percentage of total catch against number of tickler chains for common dab. left for sand and right for mud (Creutzberg, Duineveld, & Noort, 1987)

2.3. Penetration depth

Depestele studied the impact of beam trawl fishing at the seabed on the basis of the penetration depth. The beam trawl system model is shown in Figure 6

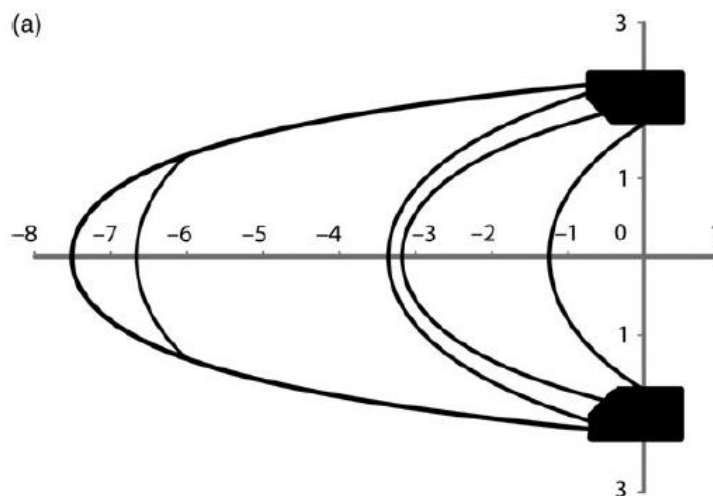


Figure 6: Modelled beam trawl system (Depestele & e.a., 2016)

The chain link diameter of the chain connected to the trawl shoe (right side in the figure) is 28 mm, while the chain link diameters of the chains connected to the ground rope (left side, only one is shown in the figure) are 11 and 16 mm. A numerical model presents the penetration depth for the different chain link diameters shown in Table 1 (Depestele & e.a., 2016). For the tickler chains connected to the ground rope a relatively high difference in penetration depth is shown compared to the tickler chain connected to the trawl shoe.

Chain link diameter [mm]	Penetration depth [mm]
11	2
16	7
28	9

Table 1: Modelled penetration depths for different chain link diameters (Depestele & e.a., 2016)

2.4. Fish behaviour

The natural fish behaviour is trying to escape when an obstacle is coming at them. (Vissen met korren, 2022) Tickler chains are used to release the fish from the sediment and swim into the net. They stimulated some fish to contract their abdomen and propel themselves upward (Broadhurst, 2021). A sailing velocity in the range of 2.5 – 7 knots (Eigaard & e.a., 2016), with the higher velocity for catching flatfish, is used to prevent the fish from escaping the net.

3. Fishing gear experiments

Experiments to study fishing gear-soil interaction are done in the past. In this chapter two examples are given. Finally a comparison is made on the basis of test parameters.

3.1. Chain experiment

Contact forces between the seabed and fishing gear components are modelled before by Sintef (Enerhaug, 2011). In their experiment a carriage is used to tow a fishing gear through a sand layer in a flume. A schematic view of their setup is shown in Figure 7.

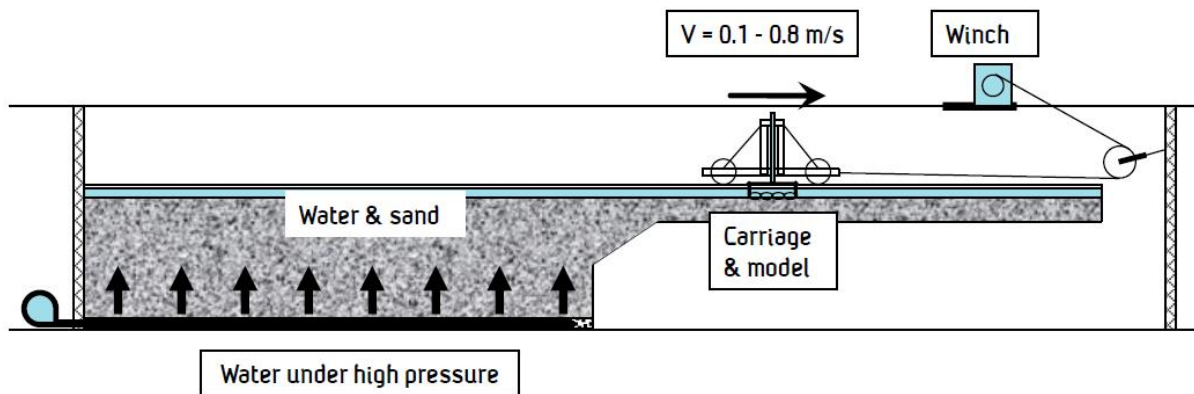


Figure 7: Schematic view of the test setup for the Sintef experiment

In this experiment four different types of fishing gear components, a chain (short and long links), a rope, a rock hopper and bobbins, are towed in a flume filled with saturated sand. A picture of their chain suspension with a long-linked chain is shown in Figure 8.



Figure 8: Test setup with long linked chain (Enerhaug, 2011)

The geometry of the gears (for the chain: short linked and long linked), the penetration depth and the angles of attack were varied in the experiment. With a fixed penetration depth during the test, force components are measured. The forces are normalised by dividing by the vertical force component. In Figure 9 an example of Enerhaug's results is given. The dimensionless forces are plotted against the angle of attack for the two types of the chain. Enerhaug observed a minimal effect. However, the penetration of the chain was limited in the experiment, resulting in very little transport of sand (Enerhaug, 2011).

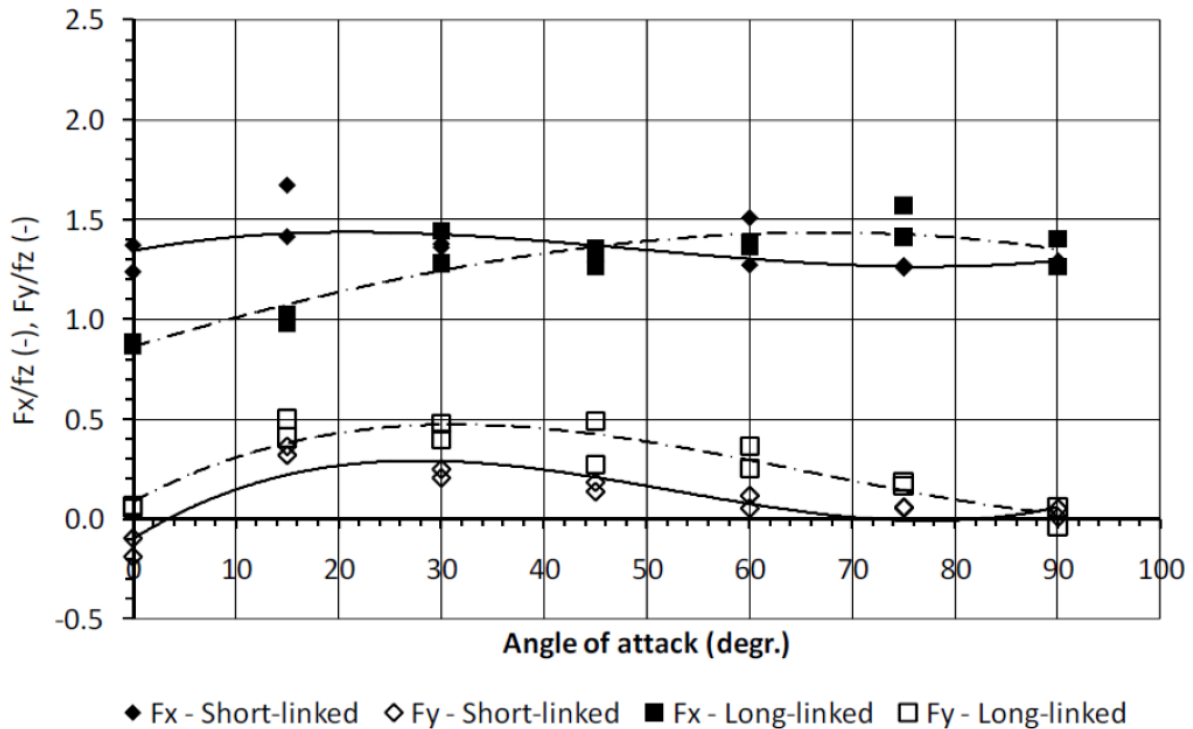


Figure 9: Dimensionless force plotted against the angle of attack (Enerhaug, 2011)

3.2. Demersal fishing gears

A study on another type of fishing gear has been done in a project called Benthis for demersal nets, containing a set of disks mounted on a rod (Ivanovic & e.a., Predicting the physical impact by towed demersal gears from fishing gear characteristics, 2015). This group towed a model of the rod with the gear components called the otter-door as shown in Figure 10 at different scales through a dry and a saturated sand bed at fixed penetration depths in a flume.

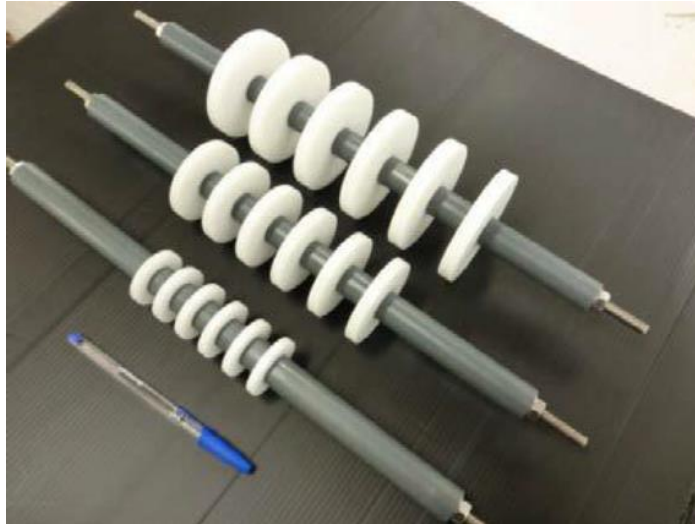


Figure 10: Gear components on the rod (Ivanovic & e.a., 2015)

The group measured the vertical, lateral and drag force of an otter-door model for different towing velocities and penetration depths. The experiment demonstrates an increase of the drag force for increasing penetration depths and towing velocities as shown in Figure 11 (Ivanovic & e.a., Predicting the physical impact by towed demersal gears from fishing gear characteristics, 2015). For higher penetration depths the curve becomes much steeper.

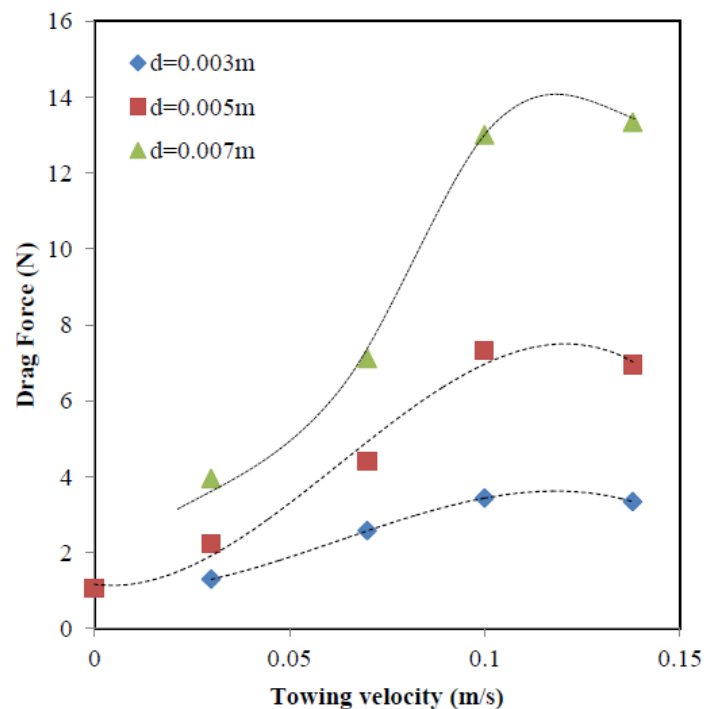


Figure 11: The mean drag force for an otter-door model plotted against the towing velocity for three different penetration depths (Ivanovic & e.a., 2015)

The group also did tests with the otter-door for different angles of attack with respect to the towing direction. In Figure 12 the drag force versus the angle attack is shown for a velocity of 0.03 m/s and a penetration depth of 5 mm.

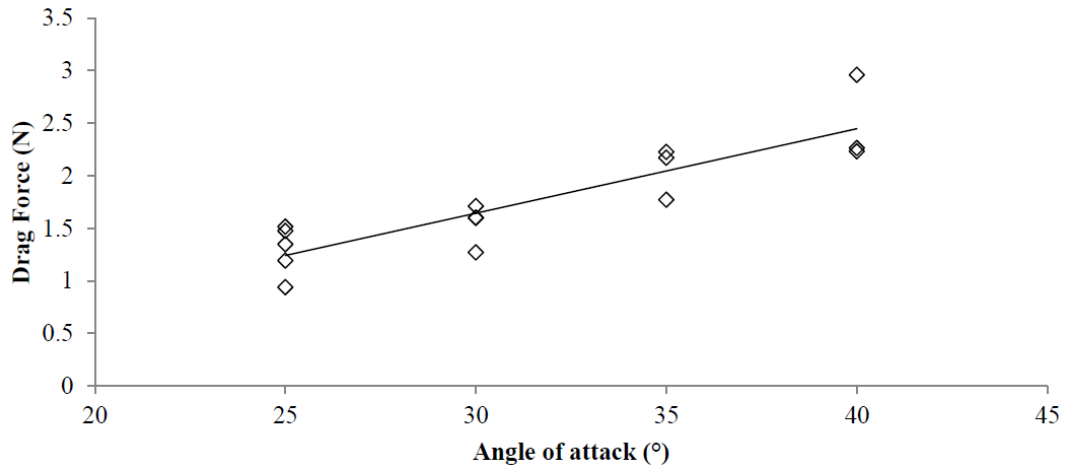


Figure 12: Drag force for different angles of attack

3.3. Overview

The experiments of Sintef and Benthis give an impression of the chain / soil interaction, although there are still some gaps to fill. In Table 2 an overview of parameters is given and whether they are varied within the experiment.

Parameter	Sintef chain experiment	Benthis demerseal fishing gear experiment
Towing velocity	No	Yes
Chain dimensions	Yes	Yes
Angle of attack	Yes	Yes
Penetration depth	Yes	Yes
Multiple chains	No	No
Grain size	No	No
Density	No	No

Table 2: Overview of parameters and whether or not they are varied within the experiment.

4. Numerical model

Fishing gear is studied by numerical models. In a study the gear component is modelled by a cylinder (Ivanovic & O'Neill, Towing cylindrical fishing gear components on cohesive soils, 2015). A finite element model is used to study the drag force and the penetration depth of the gear during towing through a cohesive soil, such as clay. The radius, width and the weight of the gear are varied in the model. Also, an aerofoil profile has been used. The velocity is not changed, so the rate effect is not incorporated in this model. The drag force turned out to be a combination of bottom surface contact and passive resistance as a result accumulation of soil in front of the cylinder.

Increase of the weight leads to a non-linear increase of the drag force and the penetration depth. Also, a dimensionless analysis has been done. The drag force and the weight are made dimensionless by dividing the force by the multiplication of the Young's modulus, radius and width of the cylinder. The penetration depth is made dimensionless by dividing the penetration depth by the radius of the cylinder. The non-dimensional drag force and penetration depth are dependent on the non-dimensional weight for the studied geometry parameters. In Figure 13 the dimensionless drag force is plotted against the dimensionless weight for the cylindrical (circle) and the aerofoil (rhombus) shape. The increase of the force is steeper for the cylinder than for the aerofoil shape.

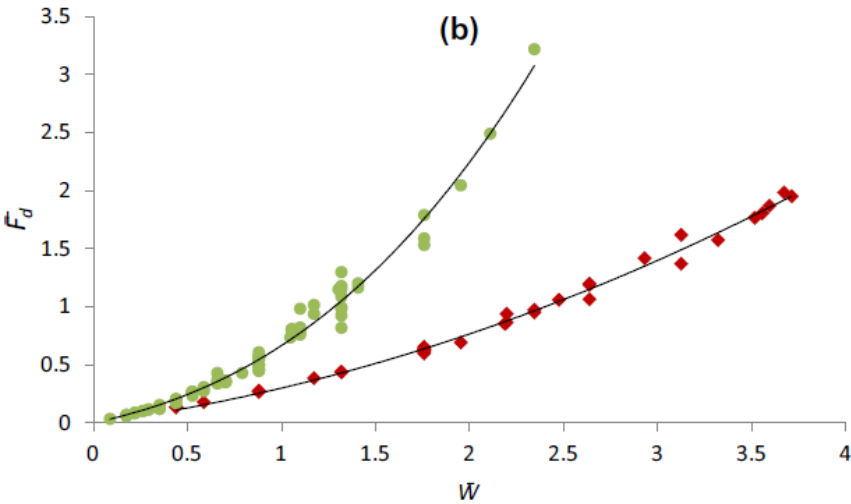


Figure 13: Dimensionless force against dimensionless weight for two different gear shapes

In Figure 14 the dimensionless force is plotted against the dimensionless penetration depth. The increase of the force is now steeper for the aerofoil shape.

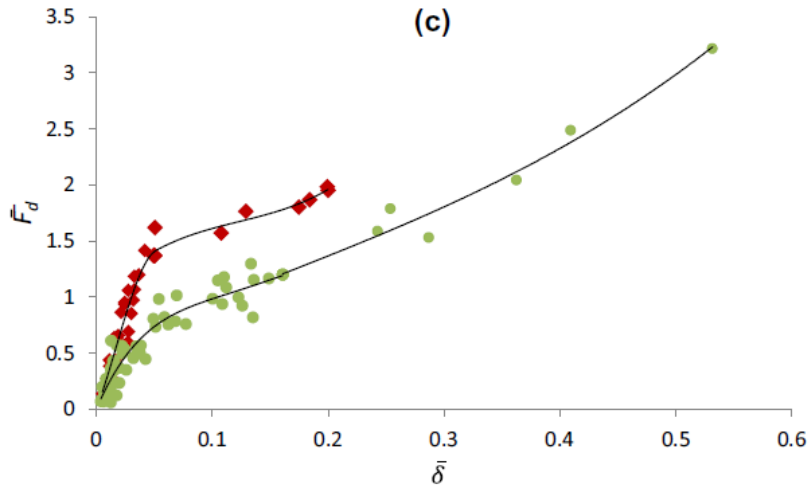


Figure 14: Dimensionless force against dimensionless penetration depth for two different gear shapes

5. Hydrodynamic drag

The hydrodynamical drag of the beam trawl system on the seabed is the the tow force caused by the fluid (in this case water). The hydraulic drag of a body can be described according to Equation 1 (Rijnsdorp & e.a., 2021). The properties of the specific gear are caught in the drag coefficient.

$$F_D = \frac{1}{2} \rho A_f U^2 c_D \quad (1)$$

F_D	drag force [N]
ρ	density of the fluid [kg/m^3]
A_f	projected frontal area [m^2]
U	towing velocity [m/s]
c_D	drag coefficient [-]

Tickler chains have a catenary shape when they are being towing through the sea (bed). Therefore an angle of attack is introduced to Equation 1, resulting in Equation 2 (Rijnsdorp & e.a., Sediment mobilization by bottom trawls: a model approach applied to the Dutch North Sea beam trawl fishery, 2021).

$$F_D = \frac{1}{2} \rho dL U^2 c_D (\sin \alpha_a)^3 \quad (2)$$

d	diameter [m]
L	length of a cylinder [m]
α_a	angle of attack [rad]

The drag coefficient is a dimensionless coefficient depending on geometry of the body, the Reynolds number and the surface roughness. The drag coefficient for the tickler chain is 2.3 (Rijnsdorp & e.a., Sediment mobilization by bottom trawls: a model approach applied to the Dutch North Sea beam trawl fishery, 2021).

6. Consolidation

In soil mechanics a distinction is made for drained and undrained soil behaviour. For undrained conditions water pore pressures play a role, which is not the case for drained conditions. The degree of consolidation will go to 1 with the progression of time. In Figure 15 the degree of consolidation for a cylinder is given as a function of time, where $U = 0$ stands for totally undrained and $U = 1$ for totally drained (Verruijt, Offshore soil mechanics, 2006). It is a function of the consolidation coefficient c_v , characteristic time t and penetration depth h .

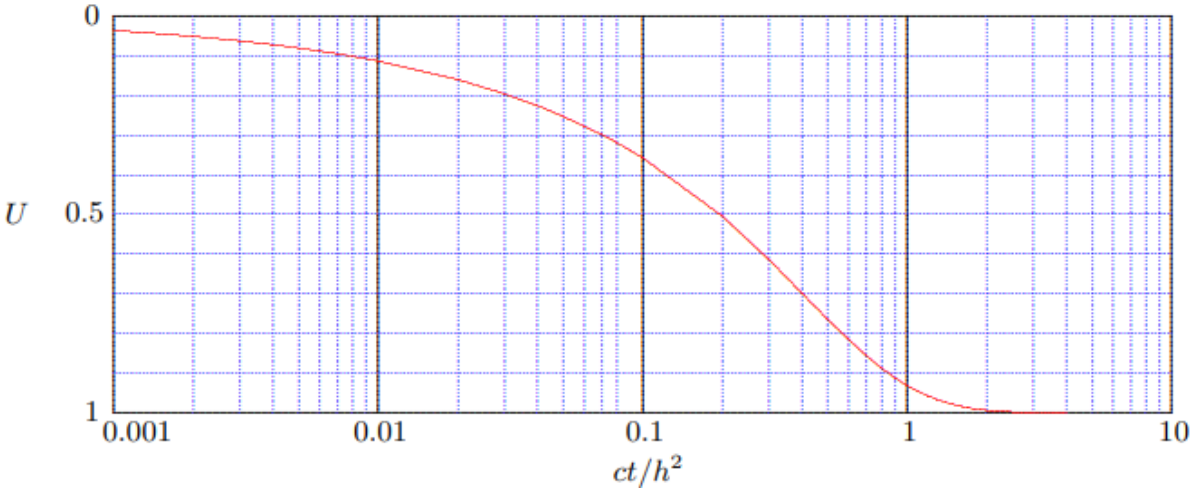


Figure 15: Degree of consolidation, where c_v is indicated by c on the x-axis (Verruijt, 2006)

The range of the consolidation coefficient for sand is $0.01 - 0.1 \text{ m}^2/\text{s}$. The characteristic time is the ratio between the penetration depth and velocity. The degree of consolidation indicates whether water pore pressures should be included in the soil resistance theories.

7. Plate anchors

In the next chapters some civil offshore engineering applications, namely stationary constructions, will be discussed, that may provide more insight in structure / soil interaction. Plate anchors are generally used to moor a floating structure to the seabed. Physical model tests are done to optimize the anchor performance. Bradshaw described scaling equations for a vertically loaded plate anchor. The scaling equations could be compared with the scaling of the soil in towing applications.

Bradshaw starts with Equation 3 (Bradshaw & e.a., 2016) describing the displacement.

$$d = \frac{q B I_f}{E} \quad (3)$$

d	displacement [m]
q	bearing capacity [Pa]
B	foundation width [m]
I_f	displacement influence factor [-]
E	elasticity modulus [Pa]

The displacement influence factor contains several effects that are equal for model and prototype. Dividing both sides of the equations by the unit weight and the embedment depth and rearranging the terms yields the dimensionless bearing pressure given in Equation 4.

$$Q'' = \frac{q}{\gamma H} = \frac{E D}{I_f B \gamma H} \quad (4)$$

Q''	dimensionless bearing pressure
γ	unit weight [N]
H	embedment depth [m]

The state of compaction of sand is defined by the relative density as shown in Equation 5 (Bolton, The strength and dilatancy of sands, 1986).

$$I_D = \frac{e_{max} - e}{e_{max} - e_{min}} \quad (5)$$

I_D	relative density index
e	void ratio

Bolton developed an empirical model from laboratory experiments of different types of sand that incorporates the confining pressure and the relative density. The relative dilatancy index determines the state of the soil and is given in Equation 6. This index should be the same for the model and the prototype.

$$I_R = I_D \left(Q - \ln(p'_f) \right) - R \quad (6)$$

I_R	relative dilatancy index
I_D	relative density index
p'_f	mean effective confining pressure at failure [Pa]
Q, R	constants

In Figure 16 the relation between the strength (difference maximum friction angle and critical friction angle) and the confining pressure is given for different values of the relative density (Bolton, The strength and dilatancy of sands, 1986).

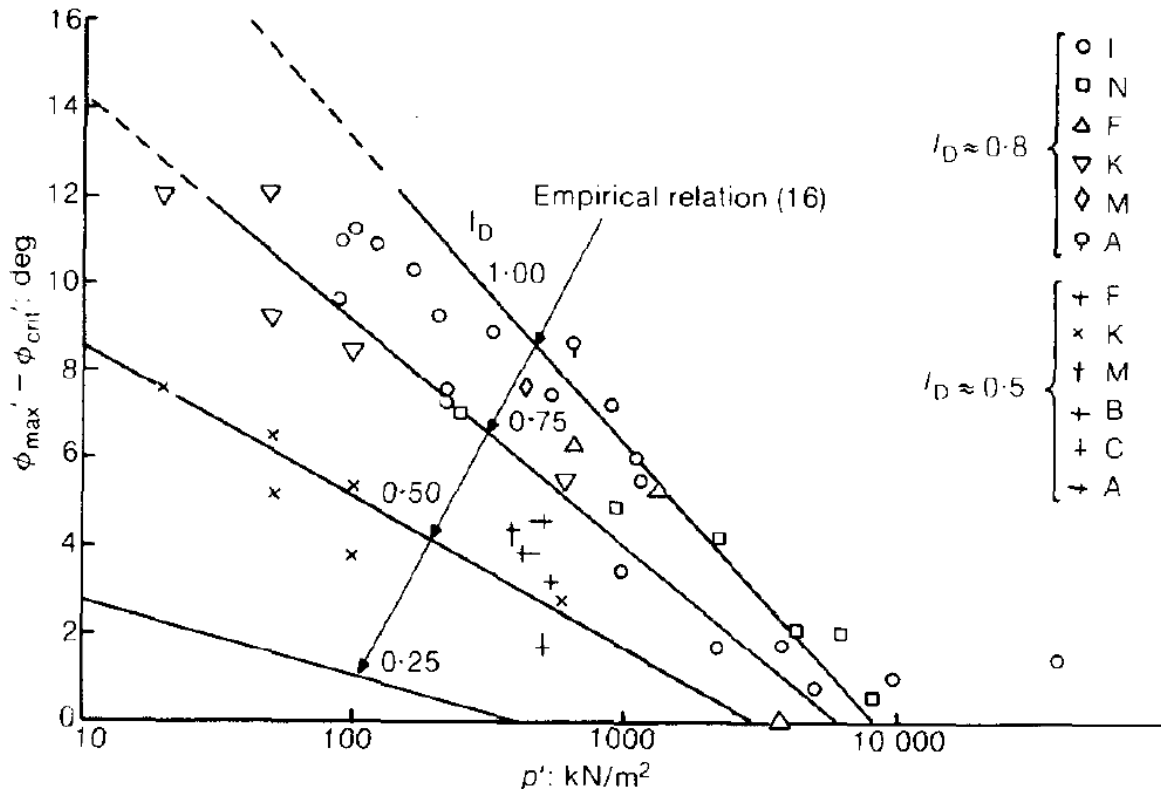


Figure 16: Strength versus the confining pressure (Bolton, The strength and dilatancy of sands, 1986)

Equation 7 establishes an empirical relation between the relative dilatancy and the strength.

$$\varphi'_p - \varphi'_c = \alpha_c I_R \quad (7)$$

α_c constant
 φ'_p peak friction angle
 φ'_c critical state friction angle

The relation between the relative density and the peak dilation angle is given in Equation 8.

$$\varphi'_p - \varphi'_c = \beta_c \psi_p \quad (8)$$

β_c constant
 ψ_p peak dilation angle

If the pull-out resistance for the prototype and the model is the same the relative dilatancy indices should be similar. This yields the void ratio of the model soil could be determined using scaling Equation 9.

$$e_m = e_{max} - \frac{Q - \ln(p'_{fp})}{Q - \ln(p'_{fm})} (e_{max} - e_p) \quad (9)$$

e void ratio

Alternatively, the void ratio of the model can be determined on the basis of the elasticity modulus. The elasticity modulus is given in Equation 13.

$$E = A e^m \sqrt{p'} \quad (10)$$

E elasticity modulus
A, m constants

For a similar dimensionless deformation response and the assumption that the displacement influence factor is the same for the model and the prototype, Bradshaw came up with the scaling of the elasticity modulus given in Equation 11.

$$\frac{E_m}{E_p} = \frac{p'_{fm}}{p'_{fp}} = \frac{\gamma_m H_m}{\gamma_p H_p} \quad (11)$$

This ends up in Equation 12 for the model void ratio.

$$e_m = e_p \left(\sqrt{\frac{p'_{fm}}{p'_{fp}}} \right)^{1/m} \quad (12)$$

8. Offshore pipelines

Pipelines buried in the seabed are used to transport water and hydrocarbons offshore (Roy, Hawlader, Kenny, & Moore, 2016). The uplift resistance is an important parameter in the design. The influence of the internal friction angle and the dilatancy of sand has been studied to understand the soil strength in relation to this uplift resistance for drained soil. In Figure 17 the pipe geometry is given.

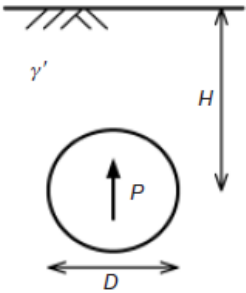


Figure 17: Pipe geometry with uplift resistance P , diameter D , penetration depth H and unit weight γ' (White, Cheuk, & Bolton, 2008)

8.1. Influence of the relative density

The uplift resistance of the pipeline is defined as a function of the critical internal friction angle, the relative dilatancy index and the overburden force. Based on Bolton’s stress dilatation relations and the limit equilibrium solution for his equations, design charts for pipelines are made. An example of this is shown in Figure 18; the normalised uplift resistance is plotted against the burial depth for different relative density indices (White, Cheuk, & Bolton, 2008). An increase of the relative density index leads to a steeper curve for the estimated normalised peak uplift resistance.

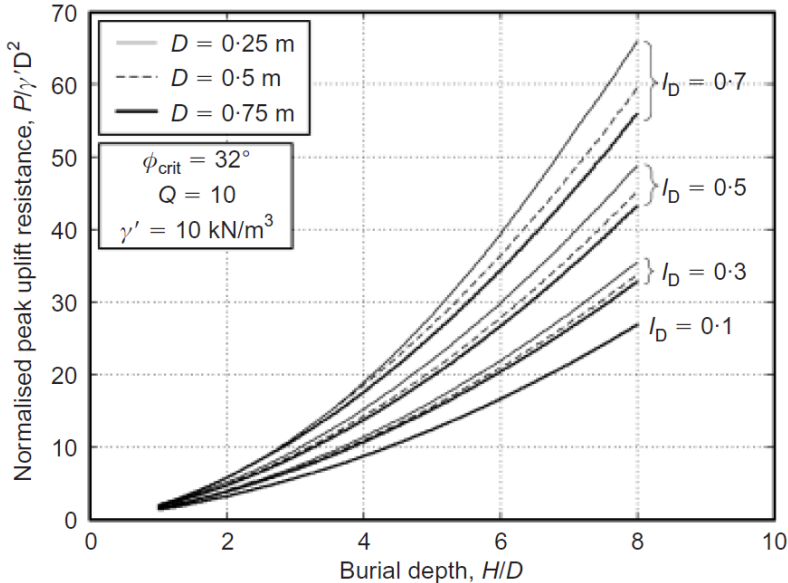


Figure 18: The normalised peak uplift resistance versus the (normalised) burial depth for different relative densities for fixed values of critical internal friction angle, natural logarithm of the grain-crushing strength Q and unit weight (submerged example) (White, Cheuk, & Bolton, 2008)

8.2. Influence of the dilatancy angle

A study to lateral pipeline-soil interaction in sand based on finite element analysis states that the soil dilatancy has a significant effect on the pipeline resistance. In Figure 19 the influence of the variation of the dilatancy angle on the normalised soil resistance is shown for different normalised burial depths (Guo & Stolle, Lateral pipe-soil interaction in sand with reference to scale effect, 2005). An increase of the dilatancy angle leads to higher values for the normalised soil resistance. The normalised soil resistance is the ratio between the soil resistance and the gravity force acting on the soil. The maximum dimensionless force is given in Equation 13.

$$N_h = \frac{P_{ult}}{\gamma H D} \quad (13)$$

N_h	maximum dimensionless force [-]
P_{ult}	ultimate lateral soil load [N/m]
γ	unit weight [N/m ³]
H	burial depth [m]
D	pipeline diameter [m]

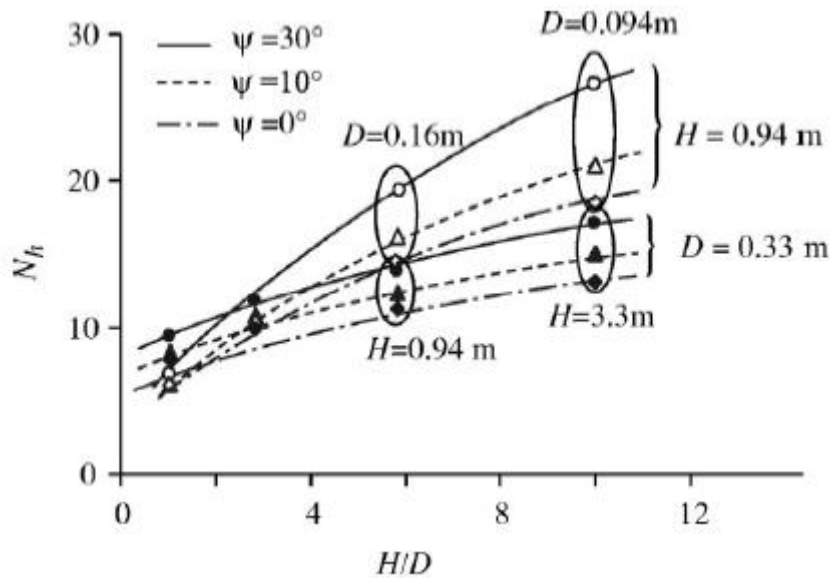


Figure 19: The normalised soil resistance against the normalised burial depth for different dilatancy angles (Guo & Stolle, Lateral pipe-soil interaction in sand with reference to scale effect, 2005)

Guo & Stolle came up with the dilation factor that describes the influence of the dilatancy angle on the soil resistance. It is defined in Equation 14 (Guo & Stolle, Lateral pipe-soil interaction in sand with reference to scale effect, 2005).

$$R_\psi = \frac{N_h}{N_{h,\psi=0}} = 1 + 0.23 \left(1 + 0.24 \frac{H}{D} \right) \sin \psi \quad (14)$$

R_ψ	dilation factor
N_h	soil resistance
$N_{h,\psi=0}$	soil resistance for dilatancy angle of 0°
H	burial depth [m]
D	pipeline diameter [m]
ψ	dilatancy angle [rad/°]

9. Laterally loaded piles

Laterally loaded piles are often used in offshore applications as a foundation for several constructions. Although it seems different from chain soil interaction in sand, some aspects could be similar. In Figure 20 a schematic view is given for a axial and lateral loaded pile.

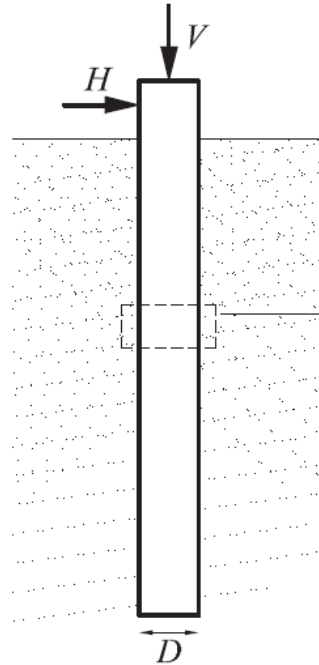


Figure 20: Schematic view of a axial (H) and lateral (V) loaded pile with diameter D (Foglia & Ibsen, 2014)

9.1. Bearing capacity

A common practice in geotechnical engineering to assess the structure-soil interaction is to predict the bearing capacity of foundations. The bearing capacity for a vertically loaded shallow foundation on a flat embedded footing in drained soil can be determined according to Equation 15 (Foglia & Ibsen, 2014).

$$q_u = cN_c s_c + \gamma' d' N_q + 0.5 \gamma' D N_\gamma s_\gamma \quad (15)$$

q_u	bearing capacity [Pa]
c	cohesion of the material [Pa]
D	width of the flat embedded footing [m]
N	bearing capacity factor [-]
γ'	effective unit weight of the soil [N/m ³]
d'	depth of excavation [m]
s	shape factor [-]

In Figure 21 the bearing capacity is plotted against the normalised depth for different methods.

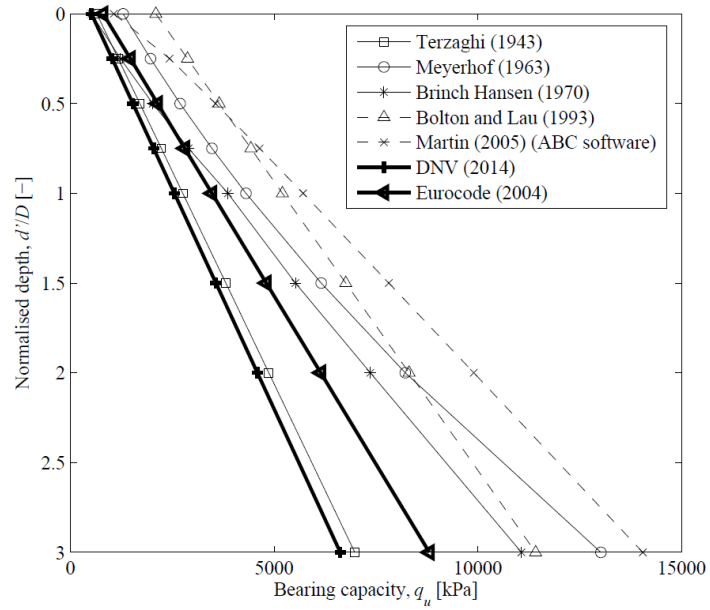


Figure 21: Bearing capacity against normalised depth (Foglia & Ibsen, 2014)

All methods show that a higher penetration depth d' or a smaller width D yields to a higher bearing capacity.

9.2. Influence of internal friction angle

In soil mechanics a distinction is made between two types of soil pressure: the active and passive soil pressure. When the soil exerts a force on an object, the related pressure is called active soil pressure. When an external force acts on the soil, the related pressure is called passive soil pressure (Verruijt & Broere, Grondmechanica, 2012). According these two definitions two pressure coefficients are defined, K_a stands for active soil pressure coefficient and K_p stands for passive soil coefficient. These coefficients represent the soil strength. They are a function of the internal friction angle as shown in Equations 16 & 17. An increase of the internal friction angle yields a small decrease of the active pressure coefficient and a rising increase of the passive pressure coefficient (Verruijt, Offshore soil mechanics, 2006).

$$K_a = \frac{1 - \sin \varphi}{1 + \sin \varphi} \tag{16}$$

$$K_p = \frac{1 + \sin \varphi}{1 - \sin \varphi} \tag{17}$$

- K_a active pressure coefficient
- K_p passive pressure coefficient
- φ internal friction angle

In Figure 22 the coefficients are plotted against the internal friction angle (Miedema, 2014).

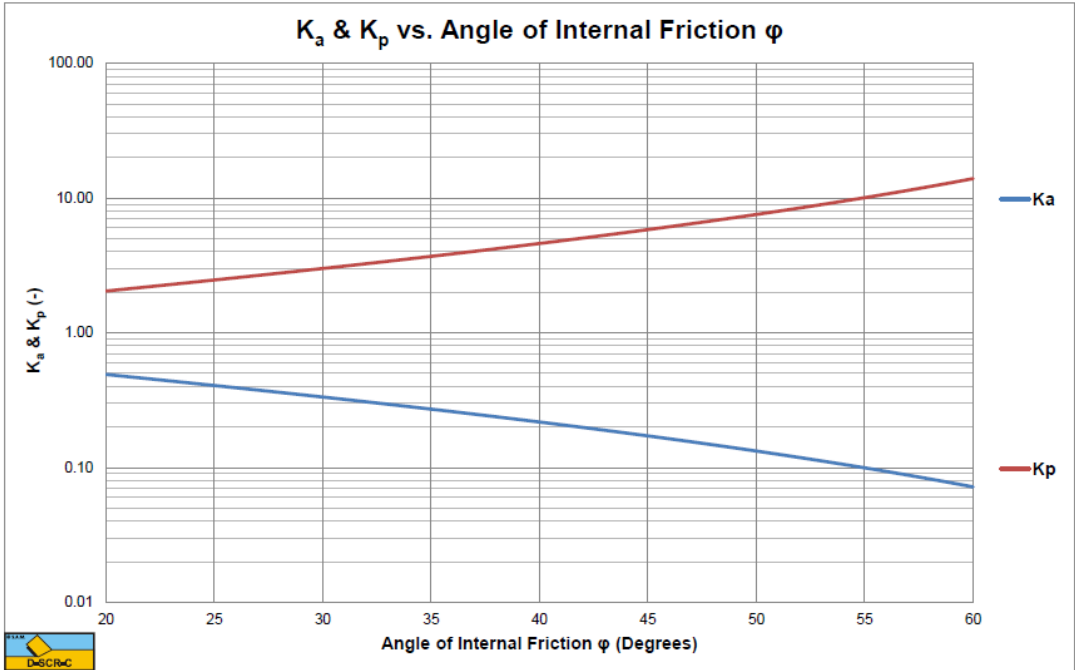


Figure 22: Soil pressure coefficients against the internal friction angle (Miedema, 2014)

According to Verruijt's theory related to laterally loaded piles, the lateral force acting on the pile is a function of these two coefficients as shown in Equation 18.

$$P = \frac{1}{6}(K_p - K_a)\gamma' D h^2 \quad (18)$$

P	lateral force [N]
K_p	passive pressure coefficient [-]
K_a	active pressure coefficient [-]
γ'	submerged unit weight of the soil [N/m ³]
D	diameter of the pile [m]
h	height of the soil [m]

9.3. Effect of scaling

Albiker studied the cyclic response of laterally loaded piles by conducting 1g model tests in the laboratory (Albiker, Achmus, Frick, & Flindt, 2017). It is almost impossible to scale down the soil without changing the material properties. Therefore, Albiker found a minimum ratio of pile diameter to mean particle size (d_{50}) varying from 55 to 88 to reduce the effect of scaling.

10. Ploughing

In the upcoming chapters some mechanical engineering offshore applications, namely moving structures, will be discussed to provide some insight in the structure / soil interaction. Ploughing is a common practice to install offshore pipelines into the seabed. Lauder conducted some experiments to study the tow force on the plough at different scales (see Appendix I for scaling parameters) and the effect of the use of a fore cutter. This could be compared to a system of multiple chains, where the chain in the front acts like a fore cutter relative to the chain behind it.

10.1. Plough with a forecutter

The forecutter is installed to reduce the drag force on the main cutter. Experiments are done to see if this is indeed the case for different types of sand. A sketch of this plough is shown in Figure 23.

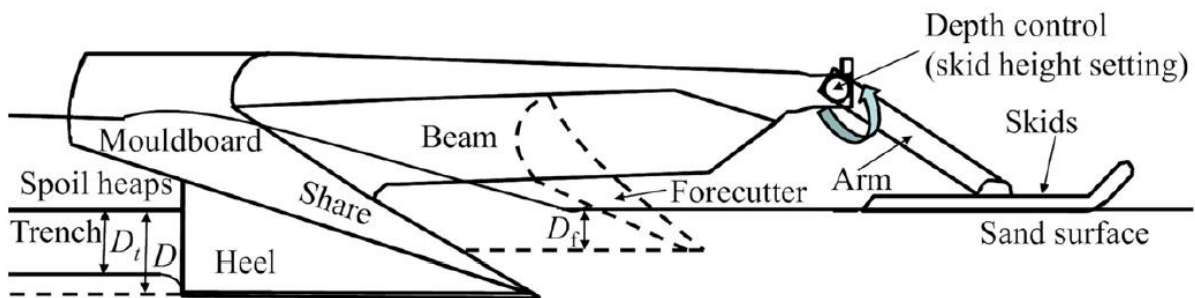


Figure 23: Plough model of Lauder (Lauder, Brown, Bransby, & Boyes, 2013)

Cathie and Wintgens performed large scale tests in the field (Cathie & Wintgens, 2001), and developed a semi-empirical relationship based on the soil mechanics theory (Equation 19) to determine the tow force for a plough.

$$F = c_w W' + c_s \gamma' D^3 + c_d V D^2 \quad (19)$$

F	tow force [t]
c_w	dimensionless friction coefficient [-]
W'	submerged plough weight [t]
c_s	dimensionless passive pressure coefficient [-]
γ'	submerged unit weight of the soil [t/m^3]
D	depth from sand surface to share base [m]
c_d	dynamic rate effect coefficient [$(t \cdot h)/m^3$]
V	plough velocity [m/h]

The first and the second term jointly represent the static force component. The first term describes the frictional resistance of the plough and the second term is the passive resistance of the soil berm formed in front of the plough (bulldozing effect). The third term is the dynamic force component and is related to soil dilation. When the velocity increases this term plays an important role. The friction coefficient c_w depends on the soil type, density and plough roughness. The passive pressure coefficient increases with density. Some tow coefficient values for different density regimes are given in Table 3 (Cathie & Wintgens, 2001).

Coefficient	Density	Value
C_w	All	0.4
C_s	Low	5
	Medium dense	10
	Dense	15
	Very dense	20

Table 3: Values for the tow coefficients (Cathie & Wintgens, 2001)

The dynamic rate coefficient c_d is not dimensionless, it depends on the type of soil and is defined in t^*h/m^3 by Cathie & Wintgens. Therefore the units of other parameters are not SI units, which should be considered when the results are compared with the results of other equations.

Palmer came up with the dimensionless group VD/c_v , where c_v is the consolidation coefficient for soil and is a function of permeability, void ratio and mean effective stress. The dilation potential is the expansion in the soil skeleton from the in-situ density to the critical density (Cathie & Wintgens, 2001). Its definition is given in Equation 20.

$$S = \frac{\Delta e}{1+e} \quad (20)$$

S dilation potential
e in-situ void ratio
 Δe change in void ratio from in-situ state to critical state

The rate effect in saturated sand is influenced by the soil response to shearing. The pore-water pressure in saturated sand continuously decreases due to the forced deformation of dilatant sand (Esmaili & Ivanovic, 2014). As a result, the effective stress and shear strength increases and so the plough resistance. To incorporate this rate effect, Lauder described the plough force in a multiplicative form instead of an additive form. This is shown in Equation 21.

$$F = (c_w W' + c_s \gamma' D^3) \left(1 + c_{dn} \frac{S V D^2}{c_v} \right) \quad (21)$$

c_{dn} dimensionless rate effect coefficient [-]
 c_v consolidation coefficient [-]

For sand the consolidation coefficient varies between $0.01 \text{ m}^2/\text{s}$ and $0.1 \text{ m}^2/\text{s}$ (Verruijt, Offshore soil mechanics, 2006). In Figure 24, Lauder showed his results of model tests for the tow force for different grain sizes and two different cases; forecutter and no forecutter, plotted against the plough velocity. The use of the forecutter yields lower forces at velocities above 60 m/h for the fine sand. In the medium sand the use of the forecutter shows less advantageous results. In Appendix II a mapping of density of silica sands is given.

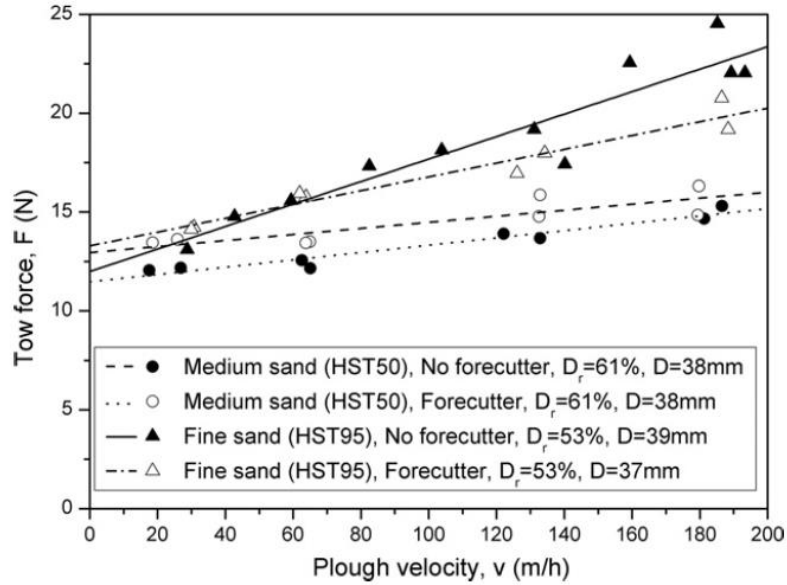


Figure 24: Tow force against the plough velocity (Lauder, Brown, Bransby, & Boyes, 2013)

Lauder made his results dimensionless by dividing the tow force by the static force (first term of Equation 20) to obtain the normalised force and using the normalised velocity as defined in Equation 20. In Figure 25 this dimensionless form of the rate effect is shown for tests with different densities without a forecutter.

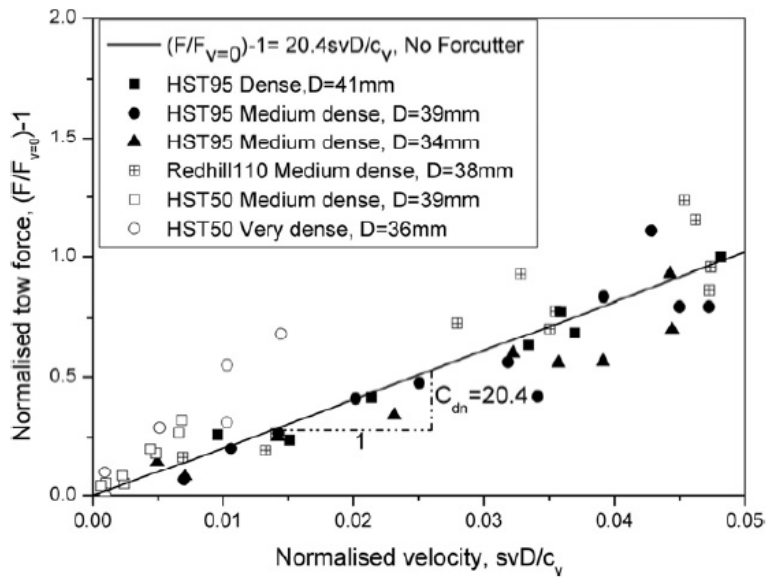


Figure 25: Dimensionless form of the rate effect

10.2. Ploughing experiments

Lauder did experiments on ploughs at different scales with different grain sizes of silica sand. Lauder used a linear variable differential transformer (LVDT) to measure the penetration depth of the plough and a load cell to measure the drag force (Lauder, 2010). The setup of this experiment is shown in Figure 26.

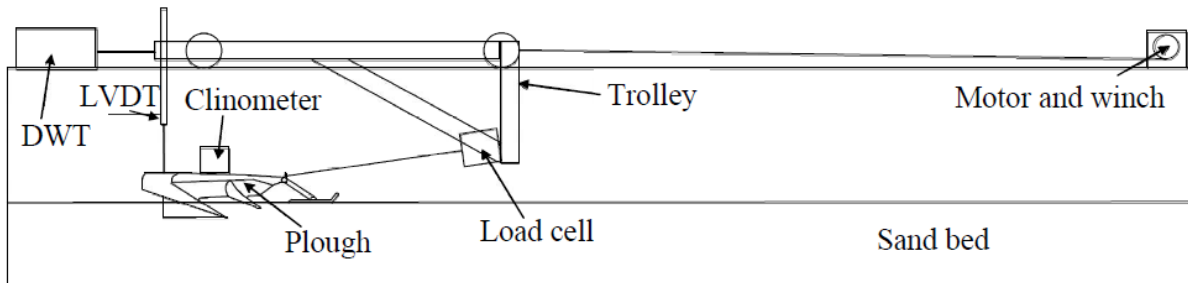


Figure 26: Test setup for ploughing experiments (Lauder, 2010)

10.3. Multi-blade plough

A study about a multi-blade plough states that the force on one blade at penetration depth h_c is higher than the sum of the forces on two blades at penetration depth $0.5 h_c$, because the force increases more than proportional with the penetration depth (Rhee & Steeghs, 1991). An example of a multi-blade plough is given in Figure 27.

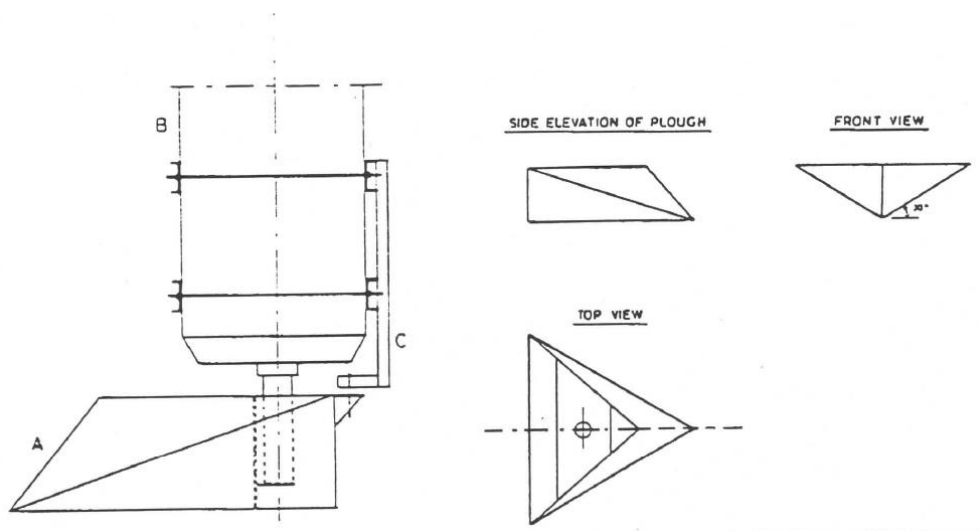


Figure 27: Different views of the multi-blade plough (Rhee & Steeghs, 1991)

To check the assumption that a multi-blade plough reduces the total cutting force, Van Rhee performed tests with ploughs in saturated sand. The multi bladed plough was done by two runs; for the second run the blade was lowered to model the multi-blade plough. In Figure 28 the force against the velocity is shown for different penetration depths.

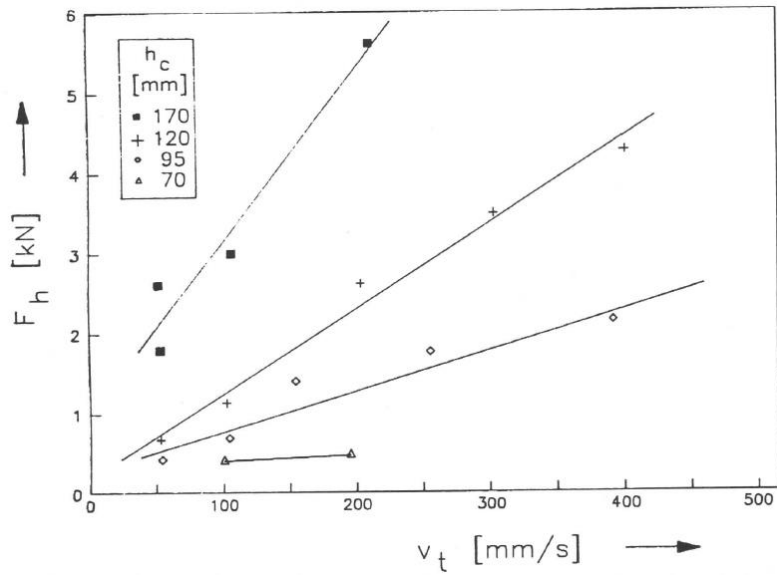


Figure 28: Tow force against plough velocity for different penetration depths (Rhee & Steeghs, 1991)

11. Cutting in sand

Cutting is applied in dredging applications to remove sand, clay or rock from the seabed. The blade forces the soil to fail by shear (Schrieck, 2014). The towing of a chain could be compared to a cutting process with a blade at an angle of 90° . Miedema describes different cutting mechanisms for different types of soil and different conditions (dry, saturated) (Miedema, 2014). For sand the cutting mechanism is called the shear type, which is shown in Figure 29.

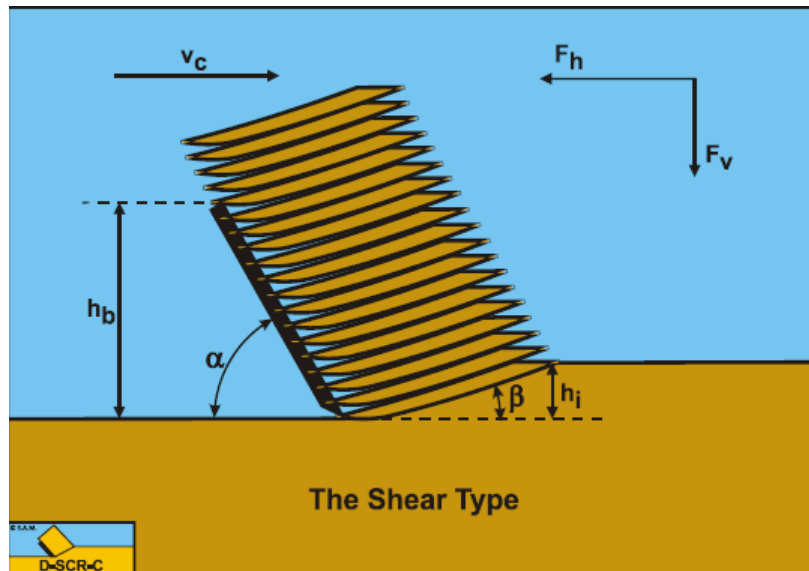


Figure 29: The shear type cutting mechanism (Miedema, 2014)

11.1. Dry sand

For dry sand the inertia forces and gravity are dominant. Adhesion, cohesion and pore pressures are negligible. Miedema uses a model that describes the cutting process as the flow type as shown in Figure 30, while in reality the process is of the shear type.

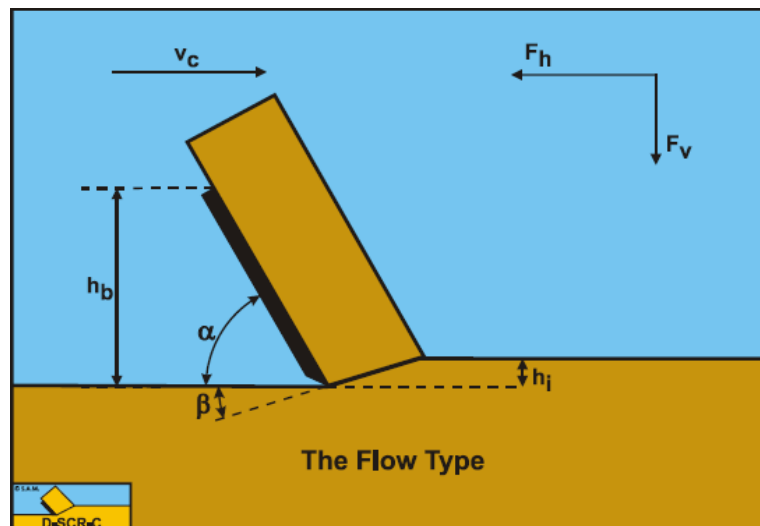


Figure 30: The flow type cutting mechanism (Miedema, 2014)

The model results in an estimate of the maximum cutting forces. The average cutting forces are in a range of 30-50% of the maximum cutting forces. The horizontal cutting force is determined by Equation 22.

$$F_i = (\rho_s - \rho_w) g h_i^2 w \left((1 - f_i) \lambda_{iD} + f_i \lambda_i \lambda_{iI} \right) \quad (22)$$

F_i	cutting force in direction i [N]
ρ_s	density of the soil [kg/m ³]
ρ_w	density of water [kg/m ³]
g	gravitational constant [m/s ²]
h_i	initial thickness of the layer cut [m]
w	width of the blade [m]
f_i	contribution of the inertia force to the total force [-]
λ_i	dimensionless inertial effect parameter [-]
λ_{iD}	cutting force coefficient in direction i [-]
λ_{iI}	cutting force coefficient in direction i [-]

The coefficients λ and f can be found in Appendix I.

11.2. Saturated sand

For the cutting of saturated sand, the vacuum pore pressure forces and the internal and external friction angles are dominant. When the blade is cutting the soils, dilation takes place in the sand. The pore volume in the sand increases due to shear stresses in the deformation zone. This increase is filled up with water, resulting in increase of grain stresses and decreases of water pressure, with the result under-water pressures. The permeability of the water flow is very low, therefore dilatancy dominates the stresses and forces. Miedema uses literature from Meijer, Van Os and Joanknecht for describing this cutting process. He starts with the so-called transformed storage equation to describe the relation between the water pressure and the cutting velocity as shown in Equation 23.

$$\left| \frac{\partial^2 p}{\partial x^2} \right| + \left| \frac{\partial^2 p}{\partial y^2} \right| = \frac{\rho_w g V_c}{k} \left| \frac{\partial e}{\partial x} \right| - \frac{\rho_w g}{k} \left| \frac{\partial e}{\partial t} \right| \quad (23)$$

ρ_w	density of water [kg/m ³]
g	gravitational constant [m/s ²]
V_c	cutting velocity [m/s]
k	permeability [m/s]

Substituting the volume strain rate in the partial time derivative results in the following qualitative relation between water sub-pressures and the average volume strain rate given in Equation 24.

$$p \propto \frac{V_c h_i \epsilon}{k} \quad (24)$$

ϵ	volume strain [-]
------------	-------------------

The influence of geometrical parameters is given in the qualitative relation in Equation 25.

$$F_{ci} \propto V_c h_i^2 w \quad (25)$$

w	width of the blade
-----	--------------------

At low velocities the cutting forces depend on gravitation, cohesion and adhesion. At a certain velocity cavitation occurs. Miedema combined the equations from Van Os and Joanknecht. If only the water under-pressures are taken into account, for the non-cavitating cutting process the cutting force in direction i can be determined according to Equation 26.

$$F_{ci} = \frac{c_i \rho_w g V_c h_i^2 \epsilon w}{k_m} \quad (26)$$

F_{ci}	cutting force in direction i [N]
c_i	dimensionless coefficient for direction i [-]
ρ_w	density of water [kg/m ³]
g	gravitational constant [m/s ²]
V_c	cutting velocity [m/s]
h_i	initial layer thickness [m]
ϵ	volume strain
w	width of the blade [m]
k_m	effective permeability [m/s]

For the cavitating cutting process the cutting force in direction i can be determined according to Equation 27. The velocity at which cavitation occurs can be determined by equalizing Equation 26 and 27.

$$F_{ci} = d_i \rho_w g (z + 10) h_i w \quad (27)$$

d_i	dimensionless coefficient for direction i [-]
-------	---

In these equations c_i and d_i are coefficients that can be found in Appendix III. They contain the sinus of the blade angle, shear angle, steel-sand interaction friction angle (also called external friction angle) and internal friction angle in the denominator, which is relevant for the validity. In Miedema's calculations the external friction angle is assumed to be two third of the internal friction angle. Miedema calculates the pore pressures using a finite element model.

11.3. Wedge theory

Unfortunately, these equations are not applicable for all situations. For large blade angles the sum of the four angles approaches or exceeds 180°. Knowing that $\sin(180^\circ)$ equals zero, this results in infinite coefficients and so on in infinite cutting forces, which is not the case in reality. When the sum of the four angles is larger than 180°, the cutting forces become negative, which is also not the case in reality. To cover these situations, Miedema describes a mechanism using a wedge, shown in Figure 31 for the shear type.

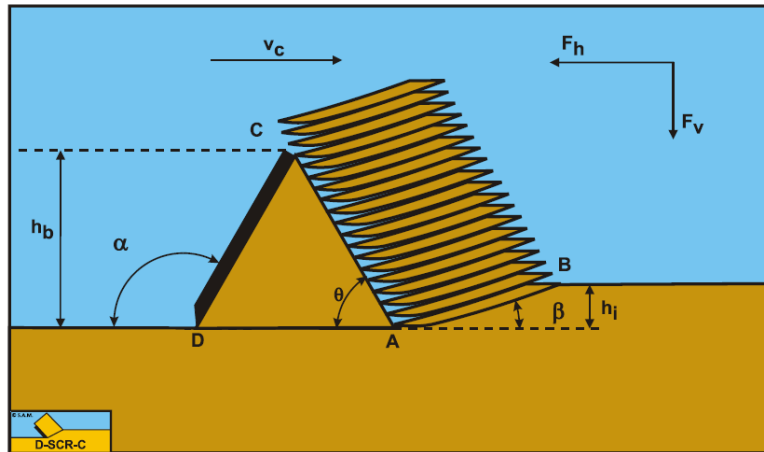


Figure 31: The shear type cutting mechanism including a wedge (Miedema, 2014)

The wedge acts like a blade with a smaller blade angle, travelling with the same velocity as the real blade, resulting in a lower sum of the four angles. Laboratory experiments showed a dynamic wedge system. Note that there is now sand-sand interaction instead of sand-steel interaction. The wedge model reduces the sum of the four angles to a smaller value than 180° (Miedema, 2014) and introduces an extra plane, the pseudo blade, and a new parameter, the wedge angle. This angle is indicated by θ . In Figure 32 and Figure 33 the forces on the layer cut and the wedge are shown in dry sand.

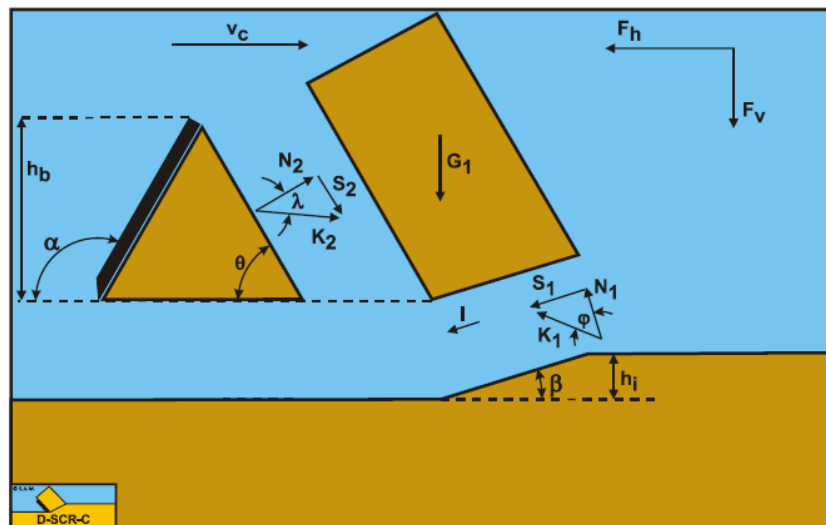


Figure 32: Forces acting on the layer cut including a wedge for the dry sand case (Miedema, 2014)

First the shear angle and the wedge angle need to be calculated. For the shear angle Equation 28 can be used.

$$\beta = \frac{\pi}{2} - \frac{2\alpha + \delta + \varphi}{2} \quad (28)$$

β	shear angle [rad]
α	blade angle [rad]
δ	external friction angle [rad]
φ	internal friction angle [rad]

For the wedge angle an empirical equation can be used as shown in Equation 29.

$$\theta = \left(\frac{\pi}{2} - \varphi\right) \left(0.73 + 0.0788 \frac{h_b}{h_i}\right) \quad (29)$$

θ	wedge angle [rad]
h_i	initial layer thickness [m]
h_b	blade height [m]

Then the weight of the layer cut and the wedge needs to be calculated. The weight of the layer cut G_1 can be calculated according to Equation 30.

$$G_1 = \rho_s g h_i w \frac{\sin(\alpha+\beta)}{\sin \beta} \left(\frac{h_b+h_i \sin \alpha}{\sin \alpha} + \frac{h_i \cos(\alpha+\beta)}{2 \sin \beta}\right) \quad (30)$$

G_1	weight of the layer cut [N]
ρ_s	density of the soil [kg/m ³]
g	gravitational constant [m/s ²]
w	width of the blade [m]
α	blade angle [rad]
β	shear angle [rad]

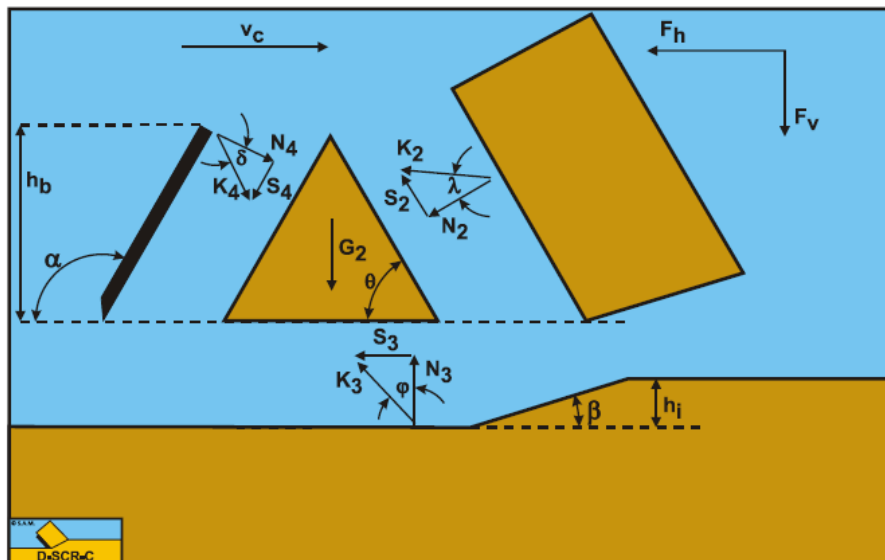


Figure 33: Forces acting on the wedge for the dry sand case (Miedema, 2014)

The weight of the wedge, indicated with G_2 , can be calculated according to Equation 31.

$$G_2 = \rho_s g \frac{h_b^2}{2} \left(\frac{1}{\tan \theta} - \frac{1}{\tan \alpha} \right) w \quad (31)$$

G_2 weight of the wedge [N]
 θ wedge angle [rad]

The inertia force depends on the cutting velocity and is also necessary for determining the cutting force. It can be calculated according to Equation 32.

$$I = \rho_s V_c^2 \frac{\sin \alpha}{\sin(\alpha+\beta)} h_i w \quad (32)$$

I inertial force on the shear plane
 V_c cutting velocity

The grain force acting on the pseudoblade is based on the weight of the layer cut and the inertia force and is given in Equation 33. The subscript d indicates that this force is for the case of dry sand.

$$K_{d2} = \frac{G_1 \sin(\beta+\varphi) + I \cos \varphi}{\sin(\alpha+\beta+\lambda+\varphi)} \quad (33)$$

Using vertical equilibrium of forces, the force acting on the blade can be determined according to Equation 34.

$$K_{d4} = \frac{K_{d2} \sin(\theta+\lambda+\varphi) + G_2 \sin \varphi}{\sin(\alpha+\delta+\varphi)} \quad (34)$$

K_{d2} grain force on the pseudoblade
 K_{d4} grain force on the blade
 λ internal friction angle on pseudoblade
 φ internal friction angle

Finally, this force can be dissolved in the horizontal and the vertical component as shown in Equations 35 and 36.

$$F_{d,h} = K_{d4} \sin(\alpha + \delta) \quad (35)$$

$$F_{d,v} = K_{d4} \cos(\alpha + \delta) \quad (36)$$

F_d force in dry sand [N]
 K_{d4} grain force on the blade for dry sand [N]
 α blade angle [rad]
 δ external friction angle [rad]

The wedge theory could also be used for saturated sand. The cutting forces are determined by the equilibrium of forces in horizontal and vertical direction at small cutting angles. Because there are three unknowns in these equations, a third equation is needed in order to solve the system. The principle of minimum energy is used in order to solve this system of equations. In Figure 34 and Figure 35 the forces on the layer cut and the wedge are shown in saturated sand. The forces on the wedge caused by water pressures are indicated by W (Miedema, 2014).

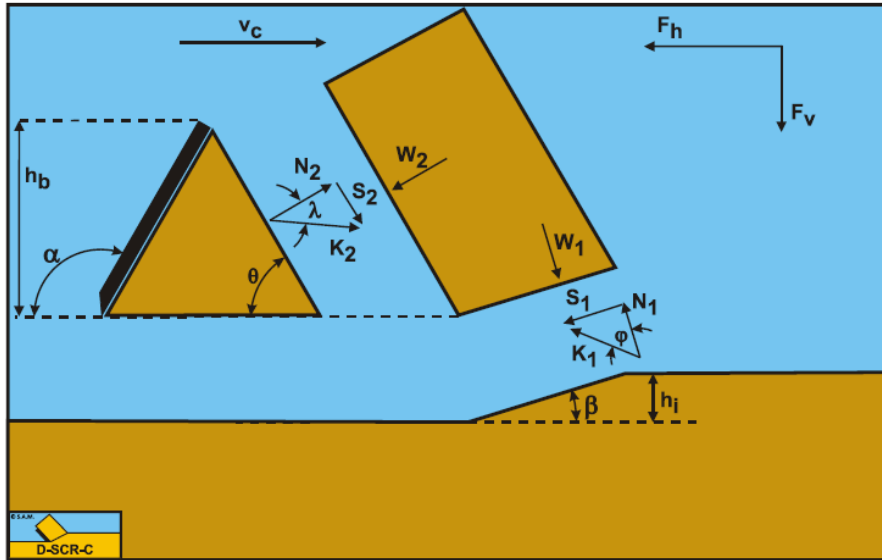


Figure 34: The forces acting on the layer cut including a wedge for the saturated sand case (Miedema, 2014)

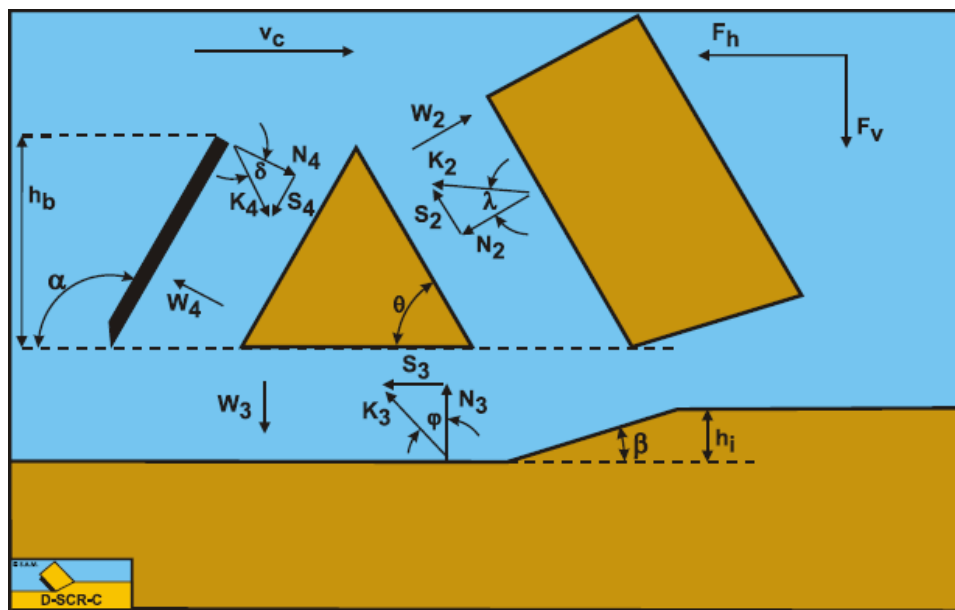


Figure 35: The forces acting on the wedge for the saturated sand case (Miedema, 2014)

Miedema calculates the average dimensionless pore pressures on the streamlines using the finite element method, the subscript indicates the position. The forces that are initiated by these water pressures are given below, starting with the force as a result of the water under pressure in the shear zone called W_1 , given in Equation 37.

$$W_1 = \frac{p_{1m} \rho_w g V_c h_i^2 \epsilon w}{k_{max} \sin \beta} \quad (37)$$

The force as a result of the water under pressure on the pressure called W_2 can be calculated according to Equation 38.

$$W_2 = \frac{p_{2m} \rho_w g V_c h_i h_b \epsilon w}{k_{max} \sin \theta} \quad (38)$$

The force as a result of the water pressure on the blade called W_4 can be calculated according to Equation 39.

$$W_4 = \frac{p_{4m} \rho_w g V_c h_i h_b \epsilon w}{k_{max} \sin \alpha} \quad (39)$$

W_1	water pressure force on the shear zone [N]
W_2	water pressure force on the pseudoblade [N]
W_4	water pressure force] on the blade [N]
p_{1m}	dimensionless pore pressure on the shear zone
p_{2m}	dimensionless pore pressure on the pseudoblade
p_{4m}	dimensionless pore pressure on the blade
p	pore pressure [Pa]
ϵ	volume strain [-]
k_{max}	maximum permeability [m/s]

The grain force acting on the pseudoblade can be calculated according to Equation 40. The subscript indicates that this force is for the case of saturated sand.

$$K_{s2} = \frac{W_2 \sin(\alpha + \beta + \varphi) + W_1 \sin \varphi}{\sin(\alpha + \beta + \lambda + \varphi)} \quad (40)$$

For the grain forces depend of the mobilized external friction angle. The mobilized external friction angle for a static wedged varies between $-\delta$ and $+\delta$, depending on the blade angle and the occurrence of cavitation. The grain force acting on the blade can be calculated according to Equation 41.

$$K_{s4} = \frac{K_{s2} \sin(\theta + \lambda + \varphi) + G_2 \sin \varphi}{\sin(\alpha + \delta_e + \varphi)} \quad (41)$$

Finally this force can be dissolved in the horizontal and the vertical component as shown in Equation 42 and 43.

$$F_{s,h} = -W_4 \sin \alpha + K_{s4} \sin(\alpha + \delta_e) \quad (42)$$

$$F_{s,v} = -W_4 \cos \alpha + K_{s4} \cos(\alpha + \delta_e) \quad (43)$$

F_s	force in saturated sand [N]
K_{s4}	grain force on the blade for saturated sand [N]
δ_e	mobilized effective external friction angle [rad]

In the end a comparison needs to be made for the results with and without the use of a wedge. The smallest force should be the right one, because nature will look for the least energy consuming mechanism.

12. Further approach based on the literature

The research questions are:

- What kind of research on this topic has already been done in the past?
- Which theories from literature could be compared with towing the chains through a sand layer?
- Which parameters influence the tow force and if they do, what influence do they have?

12.1. Conclusions from literature

Numerical models are made to study the drag force and penetration depth. In these models the gear component is usually modelled as a cylinder. Experiments can be done to check if this geometry is a good approximation of the more complicated shape of the gear. The numerical model as mentioned in Chapter 3 uses a cohesive soil, so the effect of using a non-cohesive soil (sand) and thus parameters like the internal friction angle, is not incorporated in this model. The model could be extended with different soil types and velocities. Towing tests are done before, however some parameters are not addressed in these tests, such as density, grain size, penetration depth and multiple chains. Therefore, additional experiments could be done to get a better idea of the drag force and how it is related to parameters as velocity, angle of attack, penetration depth, chain link diameter, grain size and density. Moreover, physical tests with multiple chains are not performed in the past that motivates to undertake this study. This could develop some understanding on the physics of multiple chain gear towing at the element level.

There are different disciplines in offshore engineering which are somehow similar to the towing of fishing gears through the seabed. Theories about stationary offshore equipment like plate anchors and pipeline burying are used to get a better understanding of sand behaviour and parameters, that could influence the uplift resistance, in other words the force that is needed to keep the equipment on its initial position. A relation between the relative density and internal friction is given. However, the tow force from a fishing gear is a dynamic force, because the gear is used to move along the seabed. Processes which involve equipment that moves along the seabed are ploughing and cutting. The process seems to be very similar to towing the tickler chain, although the shape of the tools is different. Experiments need to be done to validate or modify these formulas.

In addition to the basic parameters like density and velocity, additional parameters that could play a role are the degree of consolidation, the internal friction angle, the dilatancy angle. The passive pressure coefficient is increasing because of the increase of the internal friction angle.

12.2. Further approach

Overall, there is already a lot of knowledge on similar topics available. Theoretical and empirical relations exist for the prediction of the force experienced by a moving obstacle through saturated soils at certain velocities. It is not clear whether these relations are applicable on the towing of a chain. Chain links are difficult to model in a numerical model. Experiments with towing a chain at model scale can help to validate the different theories on this specific topic, see the influence of different parameters and fill the gaps in earlier tests. Parameters that can be varied are:

- grain size of sand
- density of sand
- number of chains
- velocity of the carriage
- angle of attack of the chains
- diameter of chain link
- penetration depth

A scaled setup of a chain towing system where the parameters can be controlled to a fixed value can provide more clarity on the influence of these parameters.

12.3. Expectations

The first chain in the row is cutting the sand and bringing it in suspension. It is plausible that the second chain is confronted with a suspension of sand in water, resulting in a lower towing force. A higher velocity of the carriage results in less time for the sand to settle before the next chain arrives, so the towing force is expected to decrease for the second and the third chain. After settling of the sand, the bed will be looser, which also is assumed to result in lower towing forces.

For a decrease in angle of attack from 90 up to 30 degrees, the projected area of the chain also decreases. The expectation is that the tow force will decrease as well. For an increase of velocity and penetration depth a higher tow force is expected. For the coarser grain size the depositing density is a little bit higher, the expectation is a small increase in force. For the case with no chain, a very low resistance is expected, because the influence of other materials than the chain is designed to be as low as possible.

Part II

13. Experimental design

In literature several theories are found that could be helpful to understand the tow force, however experiments are needed to check their validation for this problem. First the goal and the setup of the experiment will be described. After that the process and expectations will be mentioned, followed by the results. The results will be compared with the theory that has been discussed before. Finally, conclusions and discussion are given. Experimental tests are done at the Waterlab in Civil Engineering & Geosciences faculty of the TU Delft. In this chapter the setup and process of the experiment will be described.

13.1. Goal

These experiments will be done at TU Delft to study and validate a model of a chain element of a tickler chain. The goal is to understand the influence of the parameters mentioned in Chapter 12 and the ability to scale them. In Figure 36 the beam trawl system at model scale is shown.



Figure 36: Beam trawl system at model scale

In the experiment one element of the tickler chain with a constant length is used at a fixed penetration depth, unlike the model in Figure 36. The parameters are controlled to a fixed value and therefore it is suitable for analysing the effect of one single parameter on the tow force.

13.2. Setup

A carriage is mounted on the top of a flume. This flume is filled with a sand layer and a water layer above. The water layer makes it possible to include the influence of dissolved sand. A construction is attached to this carriage to hold one or multiple chains through the sand bed. The length of the chain is scaled down with a factor 60, the chain link diameter is scaled down with a factor 2. These chains could be rotated to represent different locations along a chain in catenary shape in practical conditions. The experiment is a captive test; the penetration depth of the chain is fixed during the towing, the only degree of freedom is translation in towing

direction. Forces in towing direction will be measured by force sensors installed at the chain end. The sensors are installed as close as possible to the sensors to exclude other resistance.

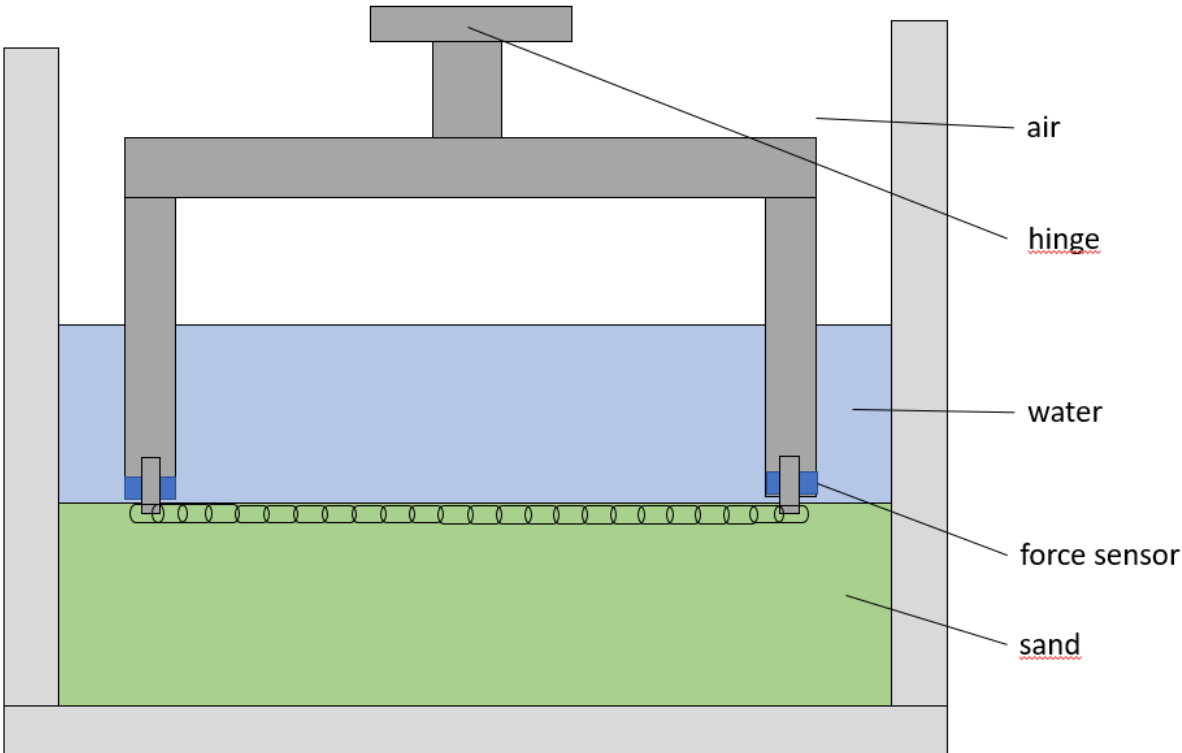


Figure 37: Schematic front view of the chain holder in the flume

In Figure 38 a total overview of the setup is shown, including the carriage, computer and camera.

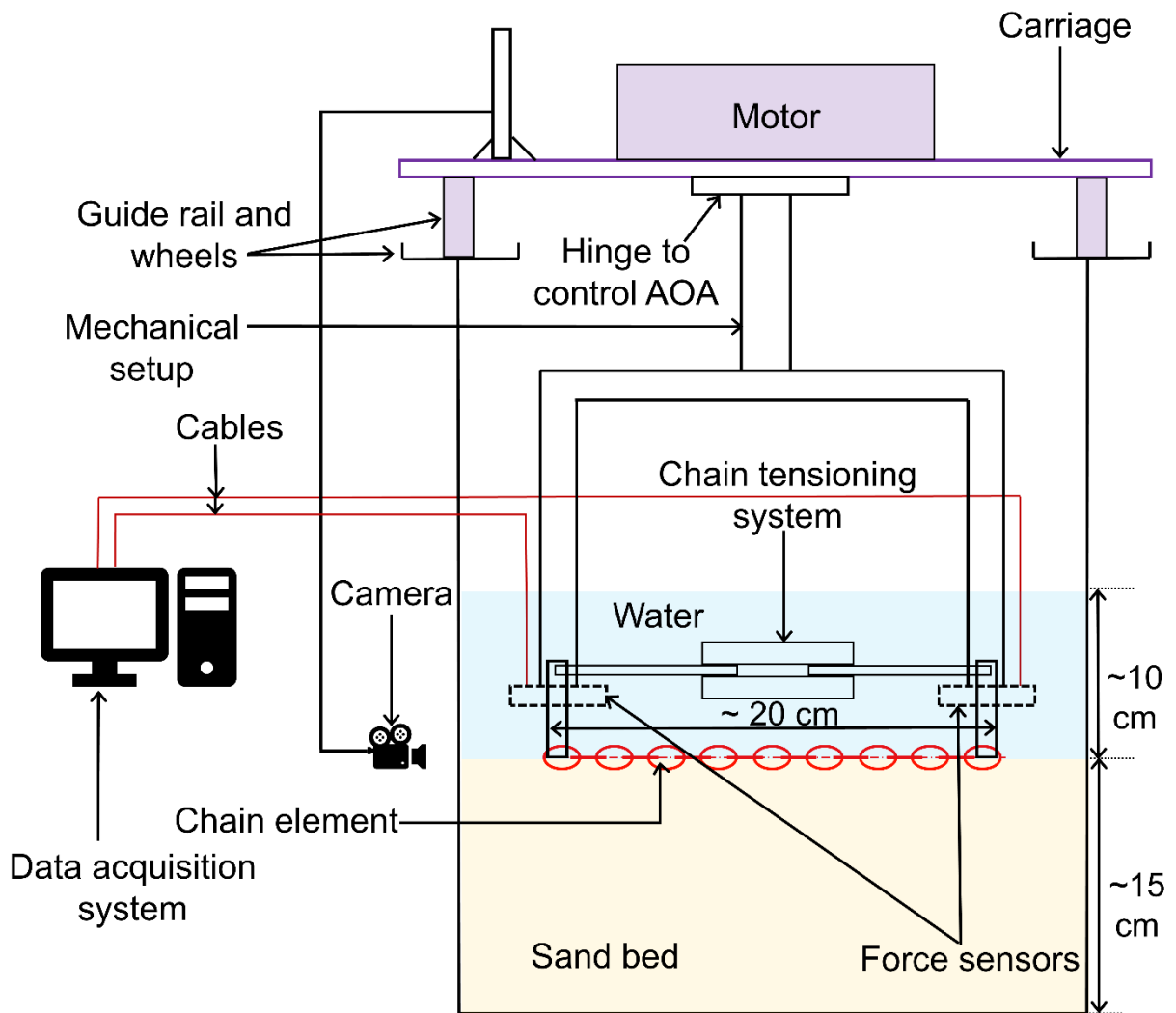


Figure 38: Total overview of the setup (figure by B. Ghorai)

In Figure 39 a top view is given including different configurations of the angle of attack.

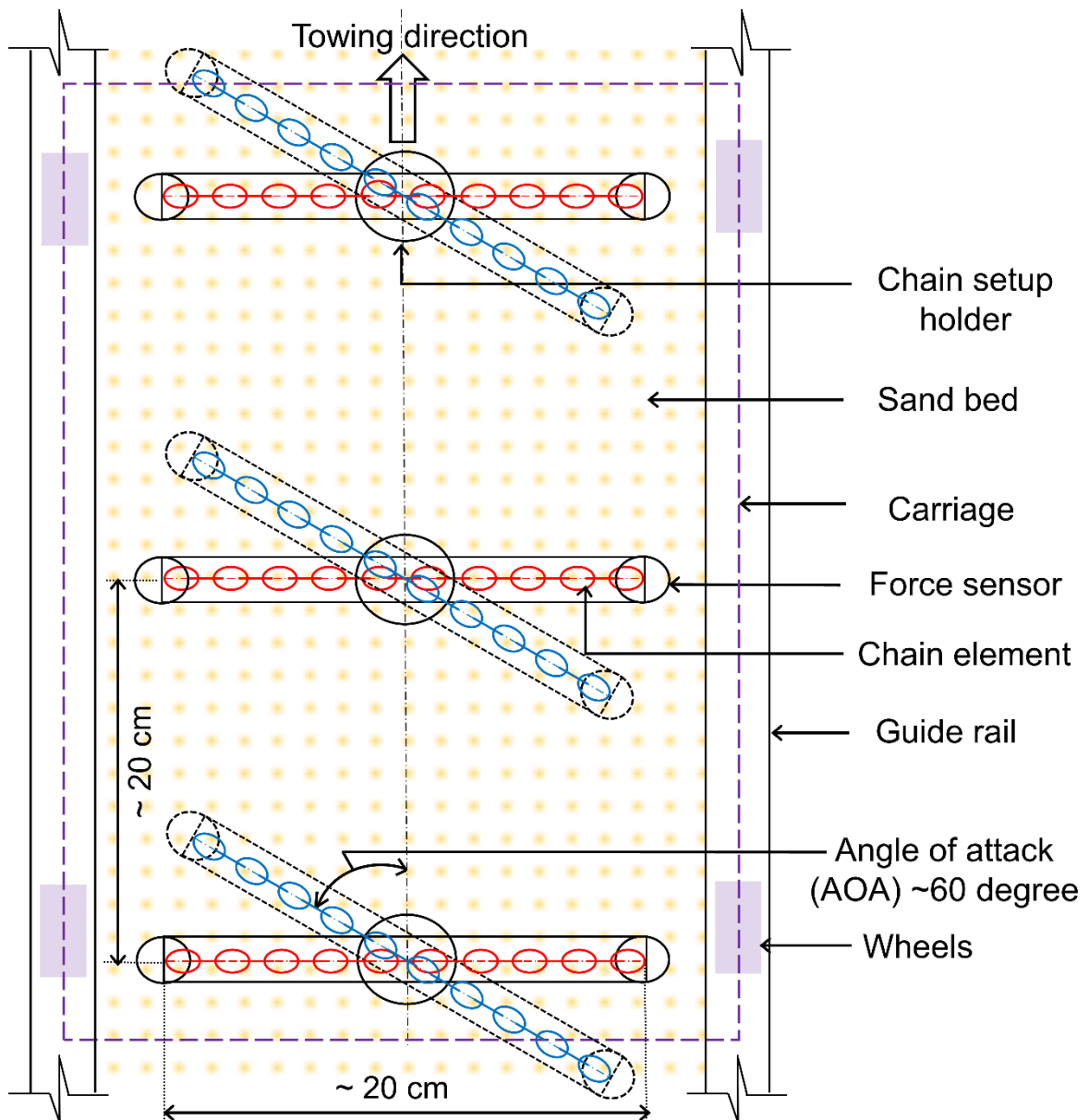


Figure 39: Schematic top view of the setup (figure by B. Ghorai)

Parameter	Value [m]
Length (begin – stop of the carriage)	3.4
Height sand (initial)	0.15
Height water	0.1
Width of the flume	0.4
Average length of the chain	0.2

Table 4: Dimensions of the setup

Three chain holders are connected after each other. In Figure 40 the chain holders are shown after disassembly, each with a different chain link diameter. In the experiment the chain link diameters are the same for the three chain holders.



Figure 40: Three chain holders with different chain link diameters

The experiment was executed in the Waterlab at the faculty Civil Engineering & Geosciences. The frontal flume in Figure 41 is used for the experiment.

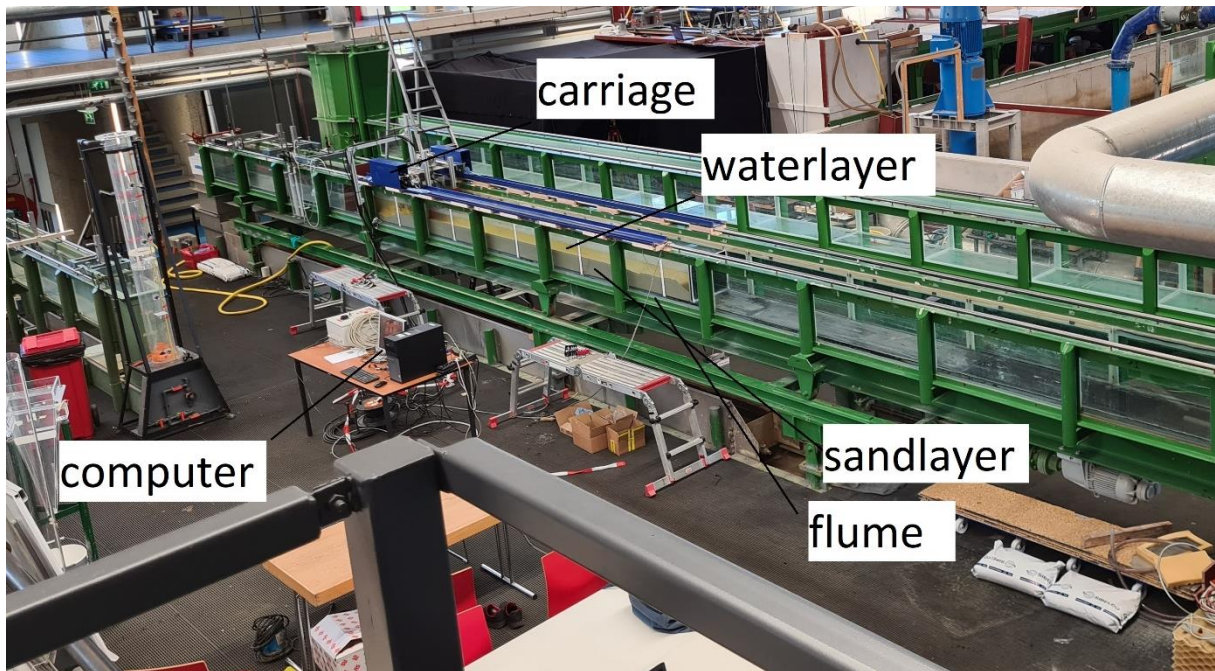


Figure 41: Picture of the experimental setup in the Waterlab

13.3. Process

The carriage is driving a route of 3.5 meter above the flume, towing the system of chains through the sand bed. During this route the forces will be measured on six positions. When the carriage reached its final position, the sand bed needs to be smoothed out. For this could a plate is installed at the front of the carriage (this is done before in experiments). This plate needs to be lowered after the experiment. When the carriage is driving back to the initial position, the plate is behind instead of in front of the carriage and smooths out the sand bed as shown in Figure 42. This is done to ensure a constant penetration depth for the next test.



Figure 42: The wooden plate that is used to level the sandbed

A vibration needle is used to increase the relative density. The mean density is measured by height of the sandbed. This height is reduced from 15 cm up to 13 cm with respect to the bottom of the flume which corresponds with a relative density increase.

13.4. Force sensors

Six force sensors are installed, type S beam load cell with IP68 rate (which means that they are water resistant to some degree), attached at each end of the chain. The sensors have a maximum capacity of 100 kg with a combined error of 0.02%. In *Appendix III* more details can be found. The force is measured perpendicular to the chain and will be corrected in the post processing for the cases with different angles of attack to get the force in the towing direction. The position of the load cells is given in Table 5.

Number	Position
1	Middle left
2	Middle right
3	Back left
4	Back right
5	Front left
6	Front right

Table 5: Position of the force sensors

The output of the load cell is an electric potential difference given in Volt. After calibration of the load cell the conversion factor from Volt to kilograms appears to be 10. The calibration is given in the specifications of the load and also checked in the laboratory (see chapter *Final calibration*). A conversion factor of 9.81 (gravitational constant) is used to obtain the force in Newton.

13.5. Parameters

Parameters that will be varied are:

- grain size of sand (2 options)
- density of sand (2 options)
- number of chains (3 options)
- velocity of the carriage (3 options)
- angle of attack of the chains (3 options)
- diameter of chain link (3 options)
- penetration depth (4 options)

Two different grain sizes of quartz sand are used, called M32 ($D_{50} = 0.26$ mm) and M34 ($D_{50} = 0.17$ mm). M34 is used as the main grain size, further tests are done with the M32 sand. More details on these sands can be found in *Appendix II*.

The loose state of the sand is used as the main case with a level of 15 cm. Further tests are done with dense sand. For this a vibration needle is used to densify the bed level to 13 cm. Other dimensions are not changed. This yields in 13% increase of mean relative density.

For the main case the setup consists of three chains connected after each other as indicated in Figure 39. In further tests one or two chains are removed.

Three different velocities are used, which could be indicated as slow (0.1 m/s), medium (0.3 m/s) and fast (0.6 m/s). For higher velocities a wave is generated in the flume which is not desirable. Before the series of experiments are done a calibration of the velocity of the carriage is done. The medium velocity is used as a reference case.

The chain holders can be installed to the motor plate at the three different angles of attack with respect to the towing direction: 90°, 60° and 30°. This is to model different parts of the chain which has in fact a catenary shape. The angle of 90° is used as a reference case. During the towing the angle of attack is fixed. The forces are measured perpendicular to the chain and will be converted to the force in the towing direction.



Figure 43: Towing the chain at an angle of 60 degrees with respect to the towing direction

Three different chains are used, which could be indicated on the basis of the chain link diameter as small (6 mm), medium (10 mm) and large (16 mm). The small chain is used as a reference case.



Figure 44: Three different chain link diameters, from top to bottom: 16 mm, 10 mm, 6 mm

In

Table 6 the masses of the chain parts including strips are given for each chain link diameter

Chain link diameter [mm]	Mass [kg]
6	0.475
10	0.948
16	1.803

Table 6: Masses for chain parts including strips for each chain link diameter

The penetration depth h_i is the distance between the top of the soil layer and the bottom of the chain. In Figure 45 a schematic definition for the penetration depth, indicated with h_i , is given.

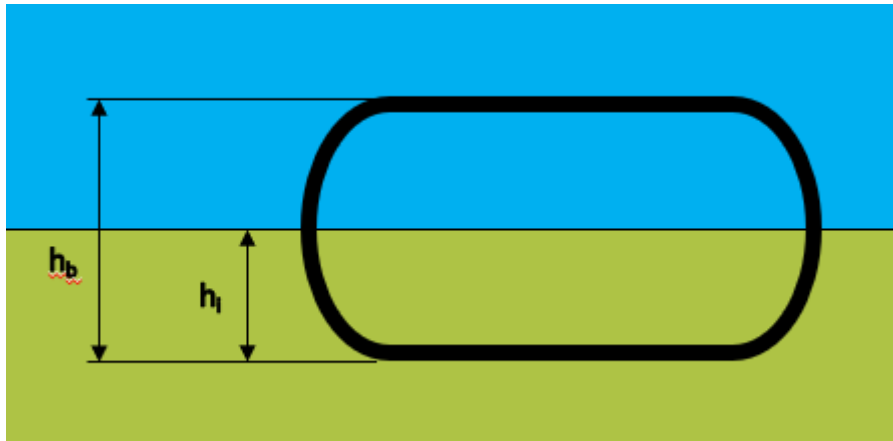


Figure 45: Definitions of penetration depth h_i and chain link height h_b

For penetration depth there is a distinction made between the same penetration for all the chains and different penetrations for each chain. The penetration depth is not the same for the different chain link diameters, because the vertical position of the centerline differs for each chain. The initial penetration of the chain (distance sandlayer – bottom of the chain) is given in Table 7: Initial penetration depths for different chain link diameters.

Chain link diameter [mm]	Initial penetration depth without disks [mm]	Penetration depth with one disk [mm]	Penetration depth with two disks [mm]
6	12	22	32
10	16	26	36
16	27	37	47

Table 7: Initial penetration depths for different chain link diameters

The penetration depth is increased by attaching one or two disks between the chain holder and the motor plate. The thickness of the disk is 1 cm, so with attaching one disk 1 cm extra penetration depth is realised, the same principle holds for attaching to disks. For the first case experiments are done with 0 cm, 1 cm and 2 cm penetration depth with respect to the initial penetration depth. For the second case the front chain will be positioned at 0 cm depth, the second chain at 1 cm depth and the third chain at 2 cm depth, all with respect to the initial penetration depth.

Tests without the attachment of a chain will be done to see the resistance caused by other equipment than the chain itself (for example chain holder, load cell, strip, screw).

In Table 8 an overview is given of the different parameters and the corresponding tests. In *Appendix VI* the complete test matrix is given.

Test number	Parameter	Value
1	Velocity	0.1 m/s
2		0.3 m/s
3		0.6 m/s
5	Additional penetration depth	10 mm
6		20 mm
10	Chain link diameter	6 mm
12		16 mm
14	Angle of attack	60°
15		30°
17	Density	Dense
18	Number of chains	1
19		2
22	Grain size	Coarse, $D_{50} = 0.26$ mm

Table 8: Overview of different parameters and corresponding tests

13.6. Reference case

In the experiment test 2 is used as the reference case. In most tests just one parameter is changed with respect to this reference case to determine the influence of this specific parameter. The reference case is shown in Table 9.

Parameter	Reference case
Velocity	0.3 m/s
Grain size	Fine, $D_{50} = 0.17$ mm
Density	Loose
Chain link diameter	6 mm
Penetration depth	12 mm (no disk)
Angle of attack	90°
Number of chains	3

Table 9: Reference case

14. Results

In this chapter the results are given for the towing force acting on all chains. Unfortunately, some tests gave bad results. Therefore the results of the 10 mm chain and cases with one and two chains are not useful.

14.1. Force calculation

The output of the load cell is a voltage in Volts as mentioned before. Before the run starts, the tow force should be zero. Therefore the value of voltage at $t = 0$ s is subtracted from all the voltages at higher t -values. Then the conversion from voltage (Volt) to force (Newton) is done by multiplication with the calibration factor and the gravitational constant as shown in Equation 44.

$$F_{tow} = (U - U_{t=0}) c_c g \quad (44)$$

For the experiments with a different angle of attack the normal force is measured perpendicular to the sensor. It is expected that the shear along the chain links also contributes to the tow force as shown in Figure 46.

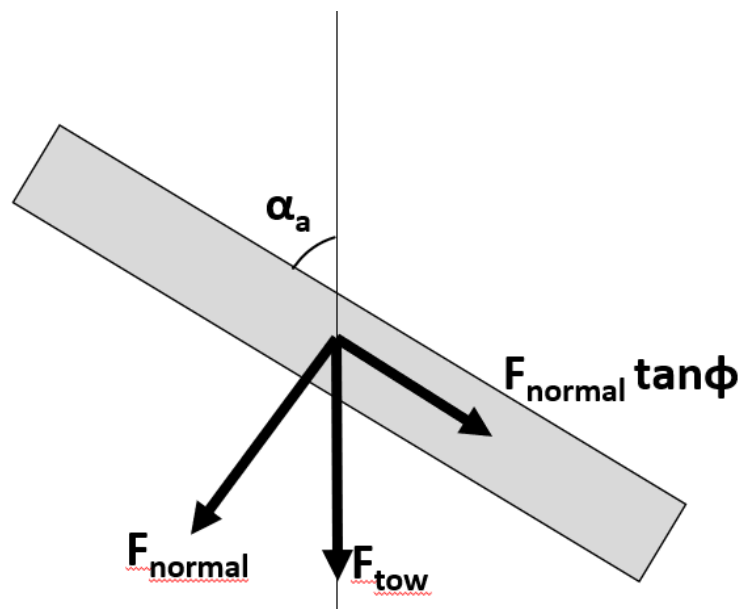


Figure 46: Forces for the case with rotated chains

An additional step needs to be taken to obtain the total force in towing direction as shown in Equation 45.

$$F_{tow} = (U - U_{t=0}) c_c g (\sin \alpha_a + \tan \phi \cos \alpha_a) \quad (45)$$

F_{tow}	tow force [N]
U	voltage [V]
c_c	mean calibration factor [kg/V]
g	gravitational constant [m/s^2]
α_a	angle of attack [rad]

The projected length is defined in Figure 47.

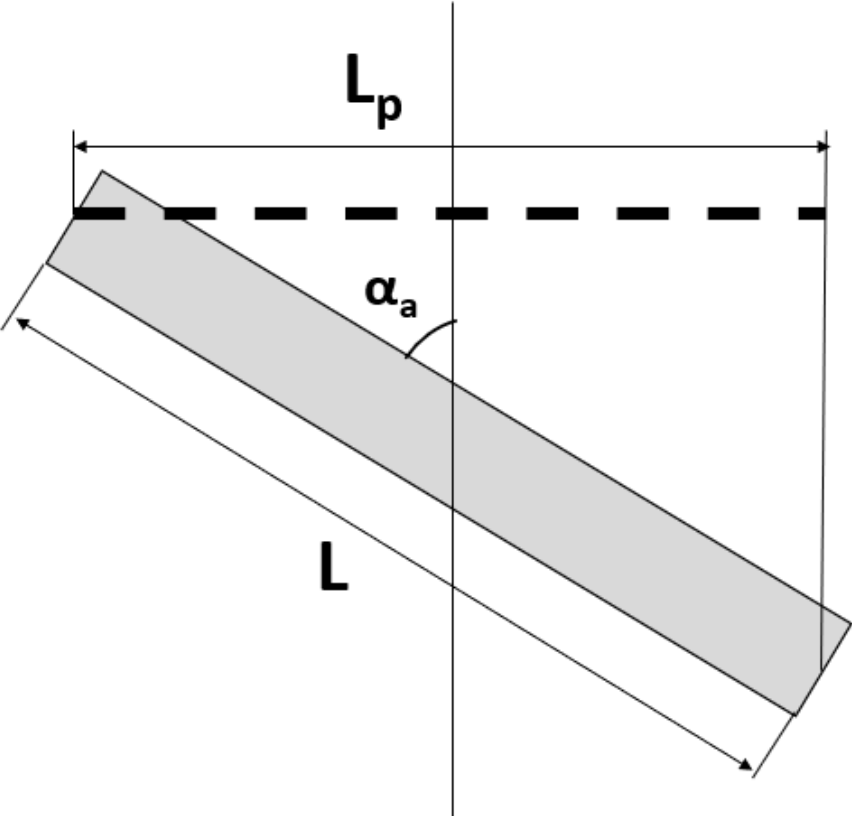


Figure 47: The projected length of the chain

The projected length decreases for increasing the angle of attack according to Equation 46.

$$L_p = L \sin \alpha_a \tag{46}$$

- L_p projected length [m]
- L length of the chain [m]
- α_a angle of attack [rad]

14.2. Comparisons with respect to the reference case

In this chapter the results are given with respect to the reference case as given in Table 9. The measured force is plotted versus time.

The force increases with an increase of the velocity for the 6 mm chain. The increase in force is larger comparing 0.1 m/s and 0.3 m/s and is less visible between 0.3 m/s and 0.6 m/s as shown in Figure 48.

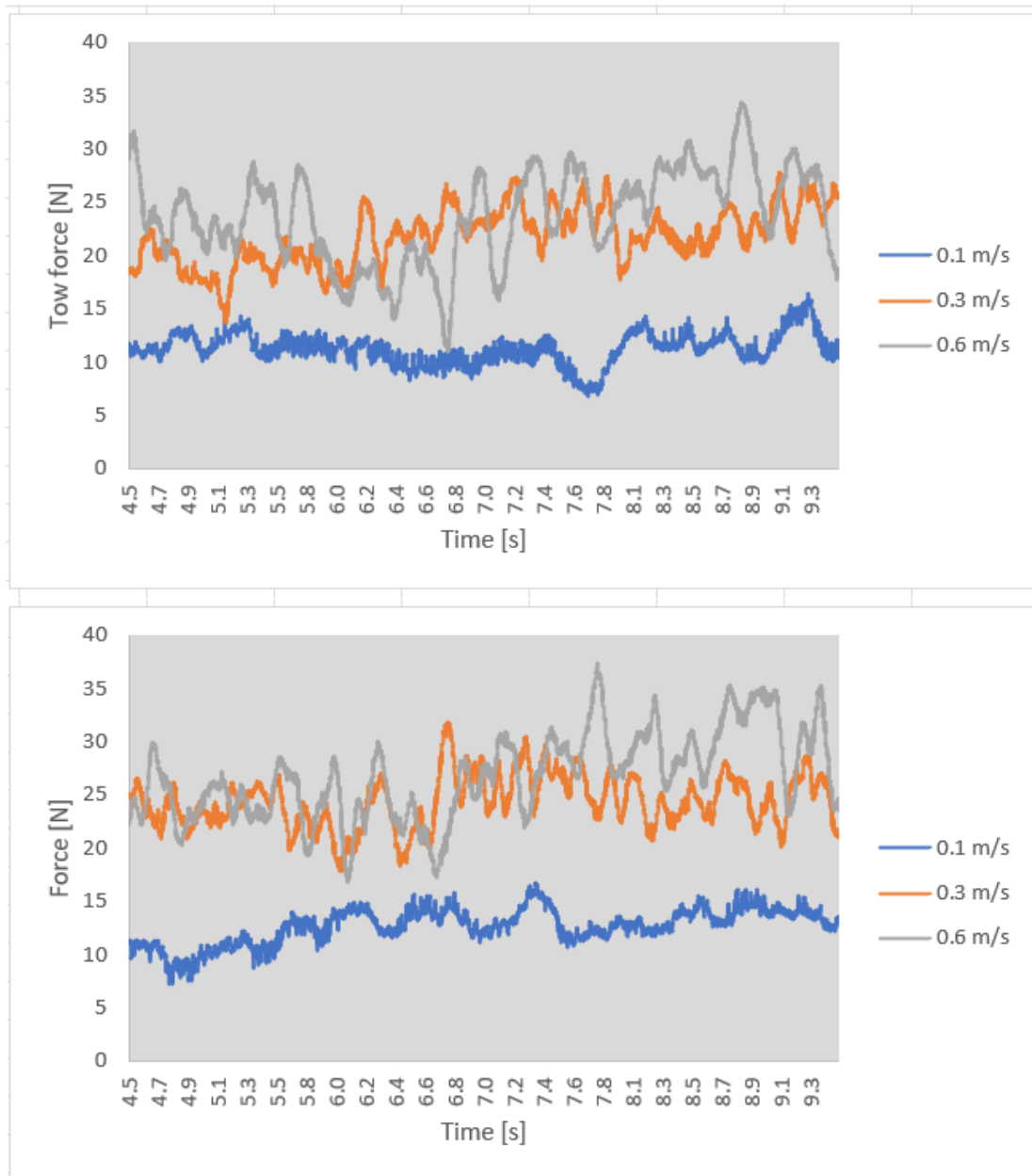


Figure 48: Force versus time different velocities in loose sand (test 1, 2 and 3)

The normal force decreases with a decrease of the angle of attack as shown in Figure 49. This can be explained by the decrease of the projected area of the chain for smaller angle of attacks.

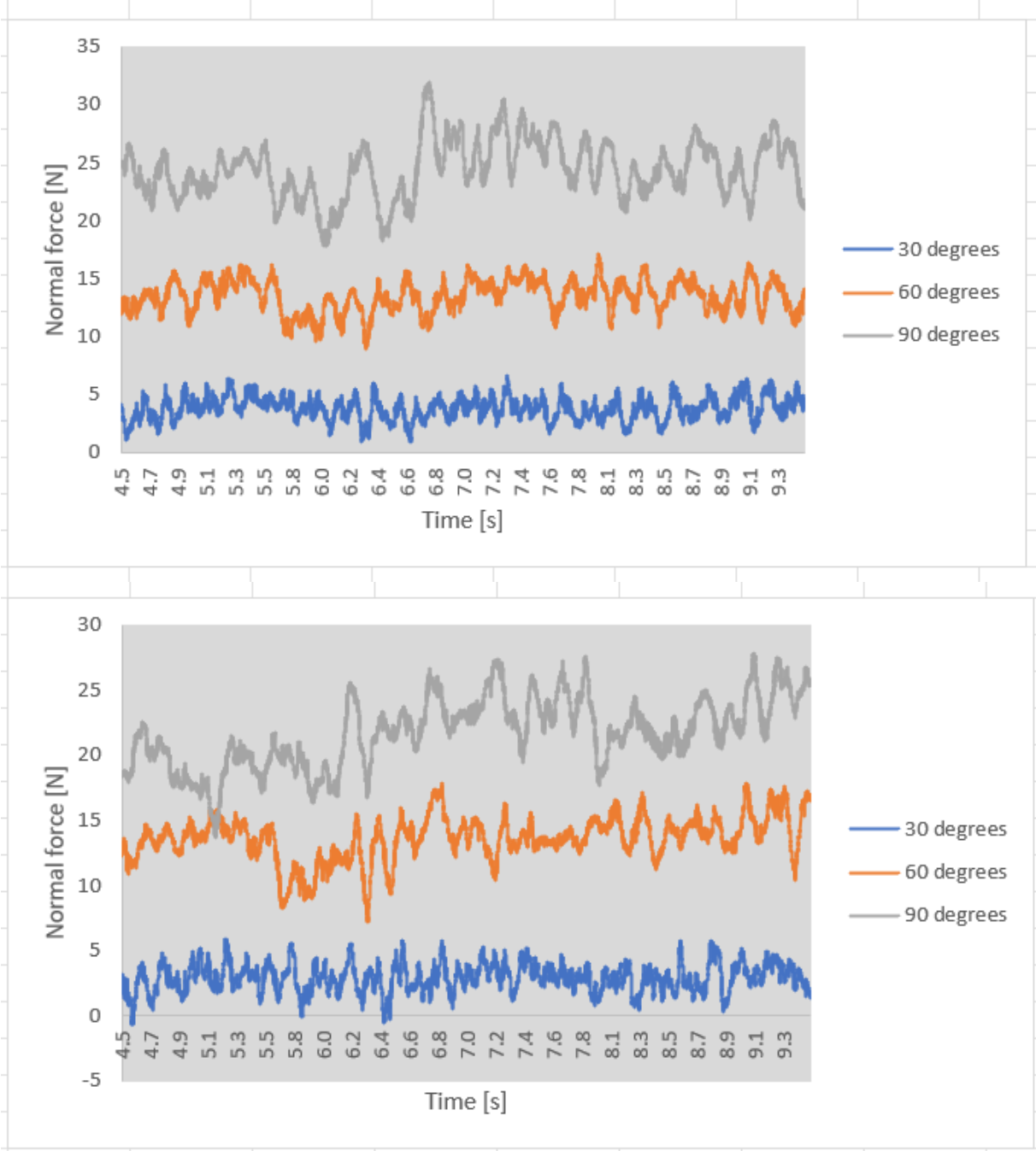


Figure 49: Normal force versus time for different angles of attack (test 2d, 14b and 15c)

In Figure 50 the force in towing direction versus angle of attack is plotted. This force is calculated according to Equation 45.

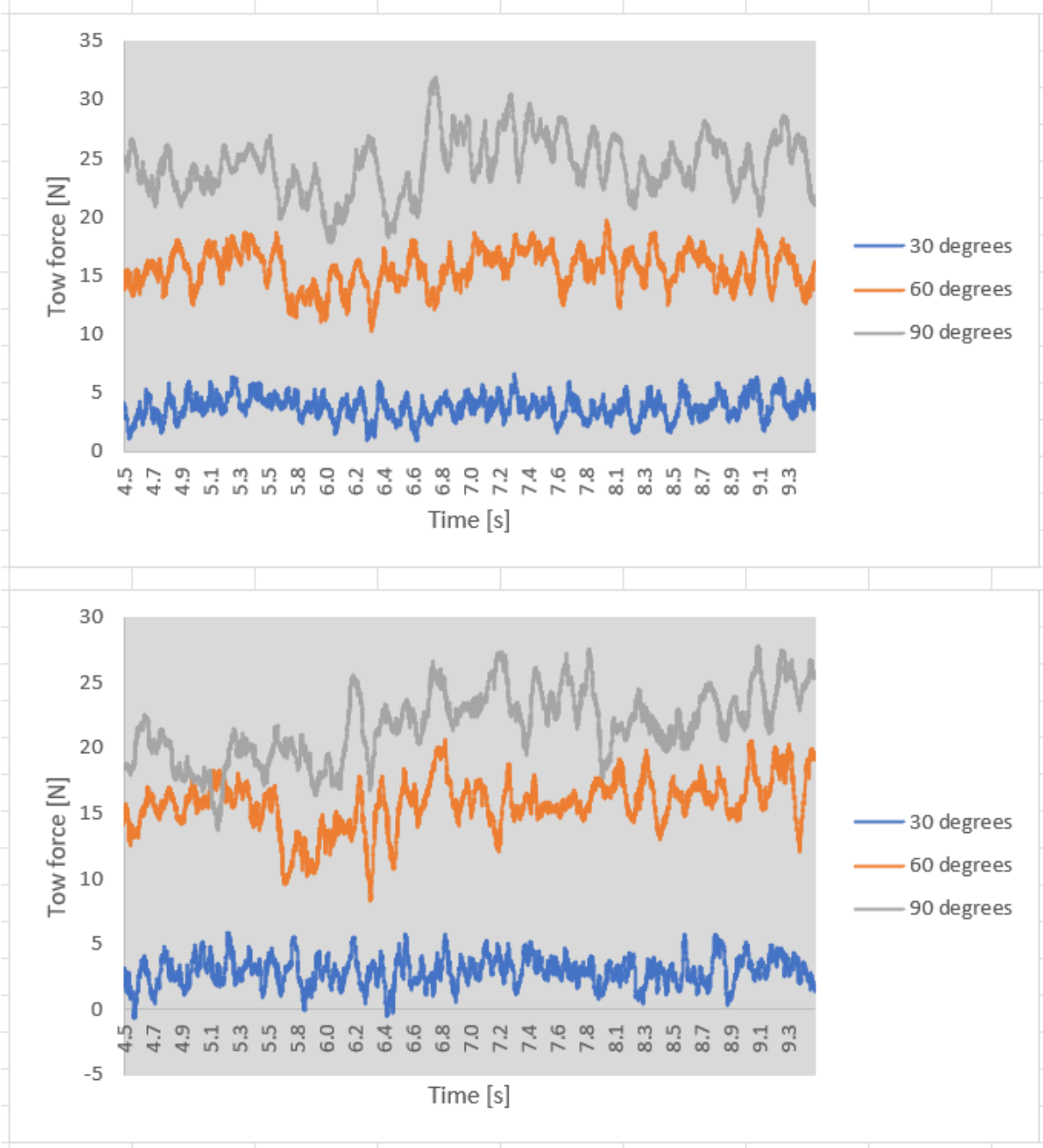


Figure 50: Force versus time for different angles of attack (test 2, 14 and 15)

In Figure 51 the force per unit length versus the angle of attack is plotted. The force obtained from Equation 45 is divided by the projected length of the chain, defined in Equation 45. There is still a decrease in force per unit length, especially for the case for an angle of attack of 30 degrees, which indicates that the decrease of the projected length is not the only cause of decrease in force.

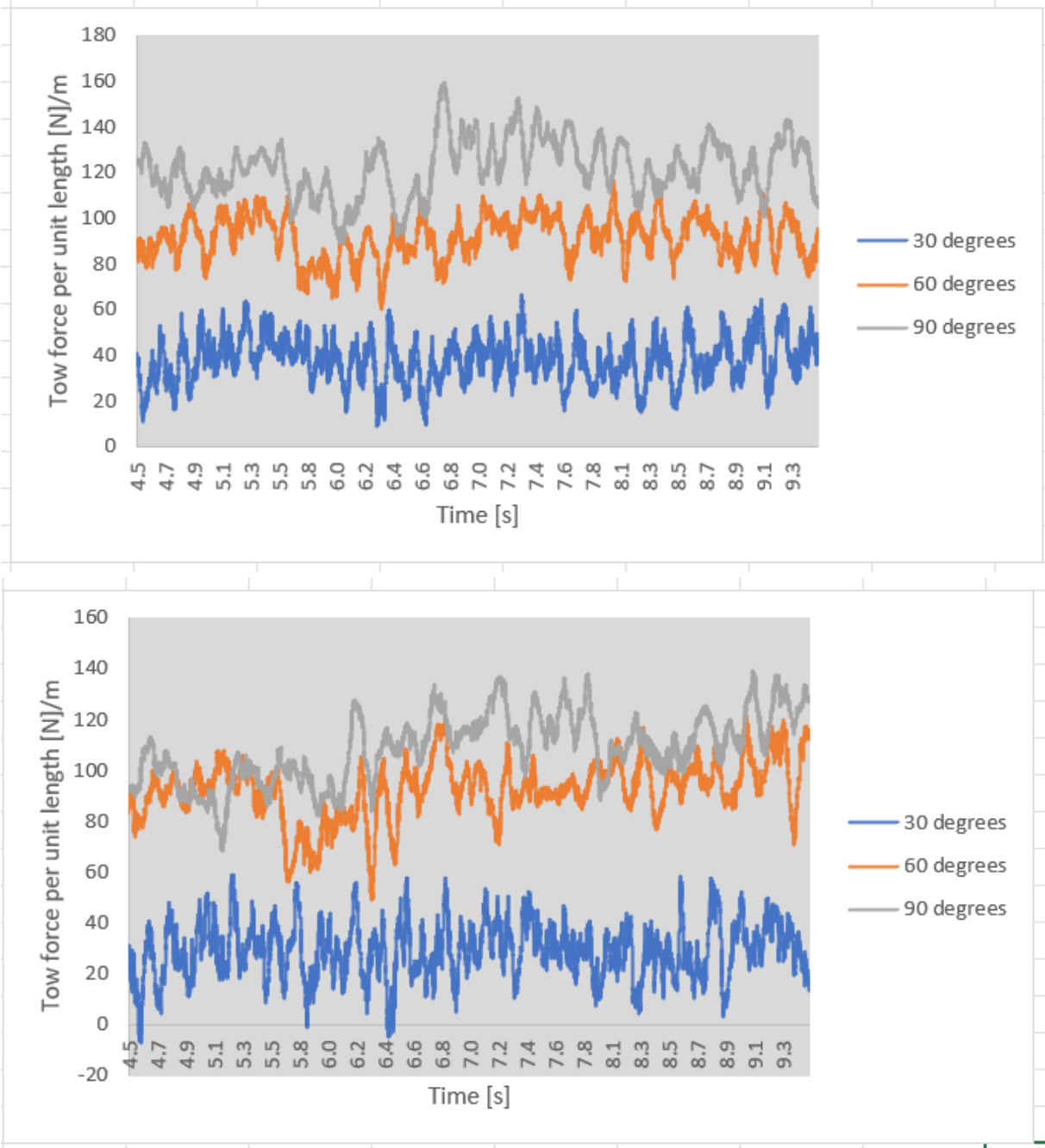


Figure 51: Force per unit length versus time for different angles of attack (test 2, 14 and 15)

In

Figure 52 the force is plotted against time for 16 mm chain. The force increases with an increase of the velocity. In the first test there is a high fluctuation for the 16 mm chain. In the second test this force is more constant.

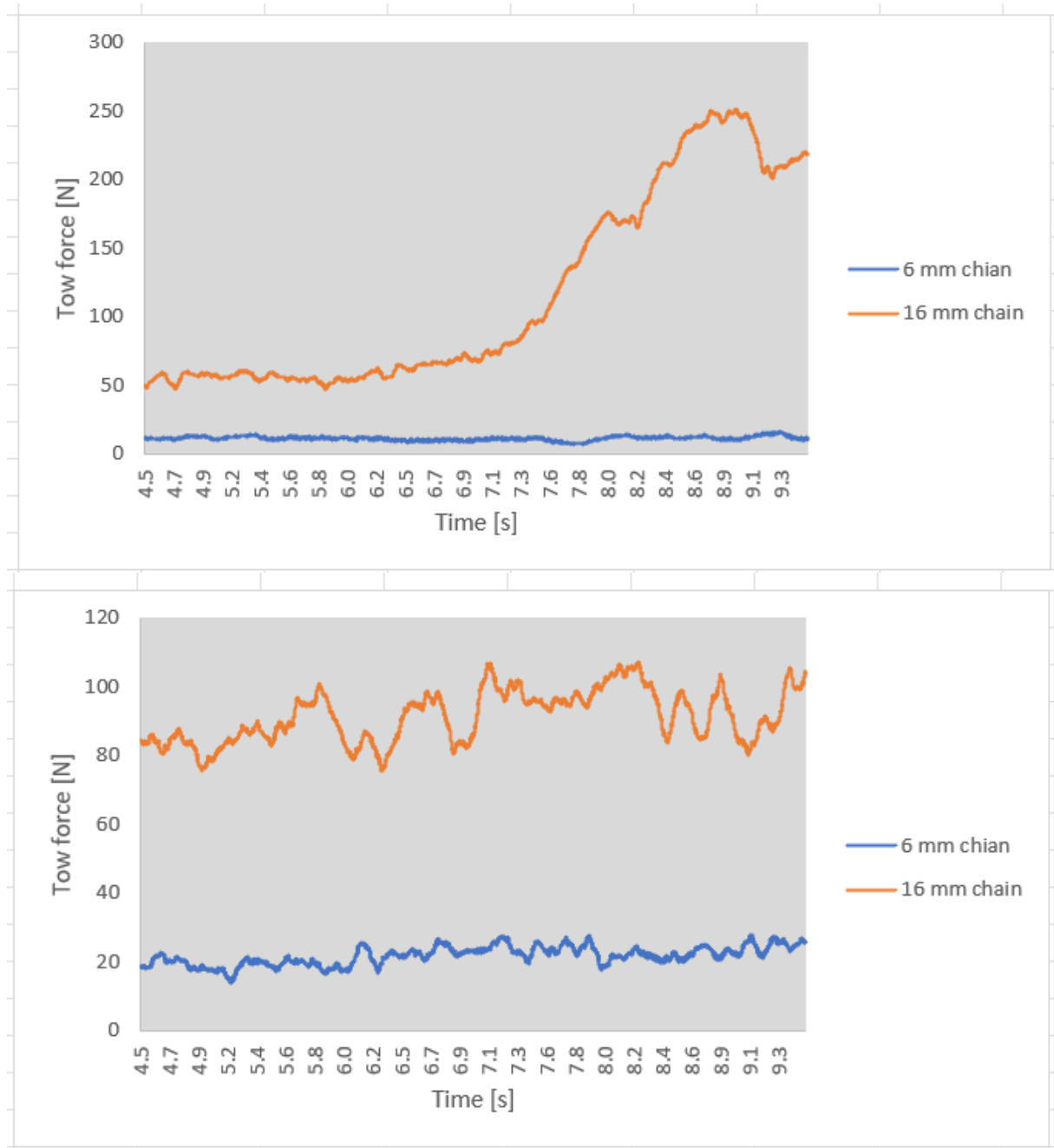


Figure 52: Force versus time for different chain link diameters (test 2 and 12)

In

Figure 53 the force versus time is plotted for different additional penetration depths. The force increases with an increase of the relative penetration depth. Note that the initial penetration depth is indicated as 0 cm in the legenda. while, there is already a little penetration, that depends on the chain link diameter. Therefor a comparison for different chain link diameters seemed to be hard.

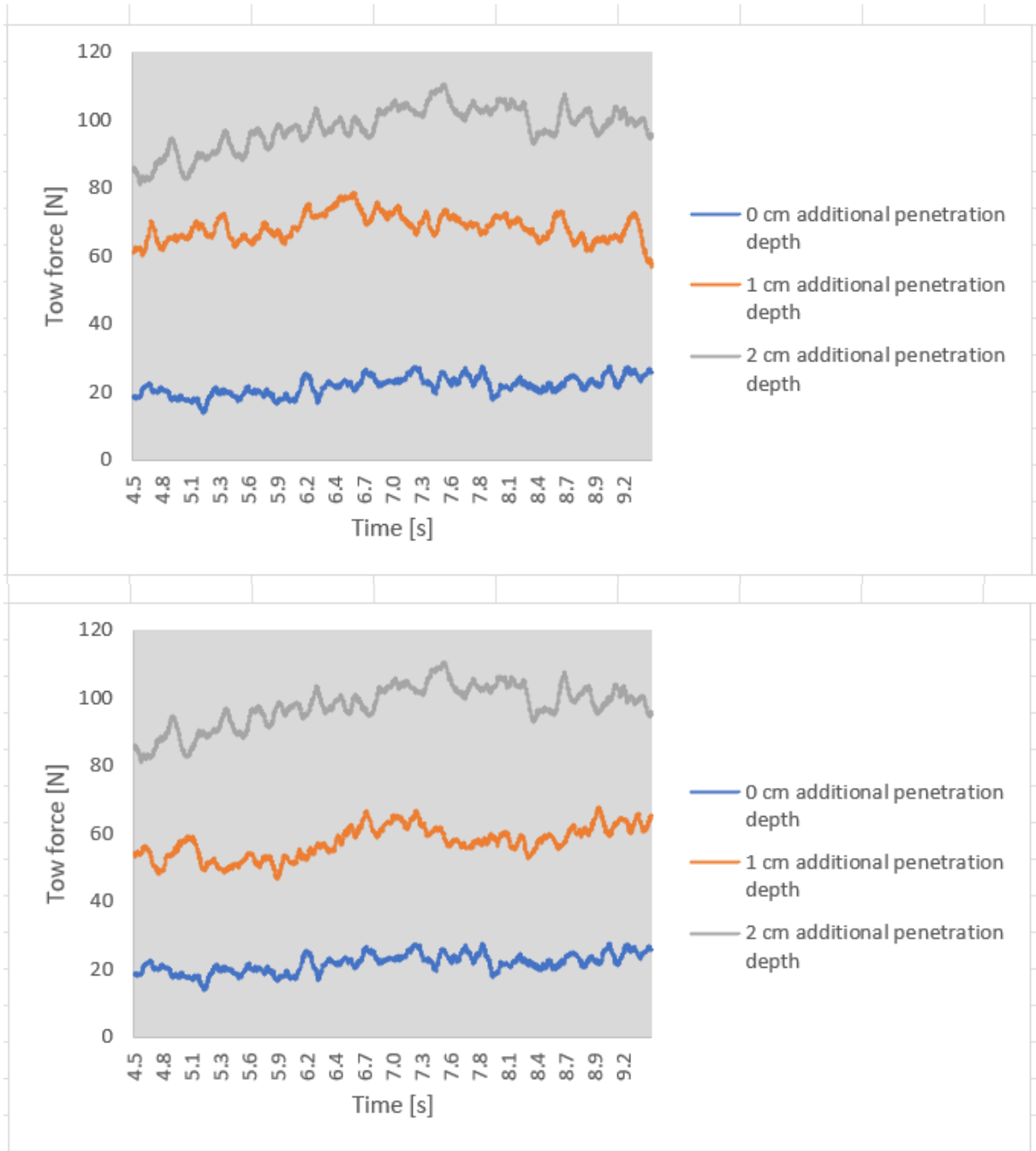


Figure 53: Force versus time for additional penetration depth (test 2, 5 and 6)

The force increases with an increase of the density as shown in Figure 54. In the first test the sandbed level was a bit too low. Therefore the force difference is higher in the second test.

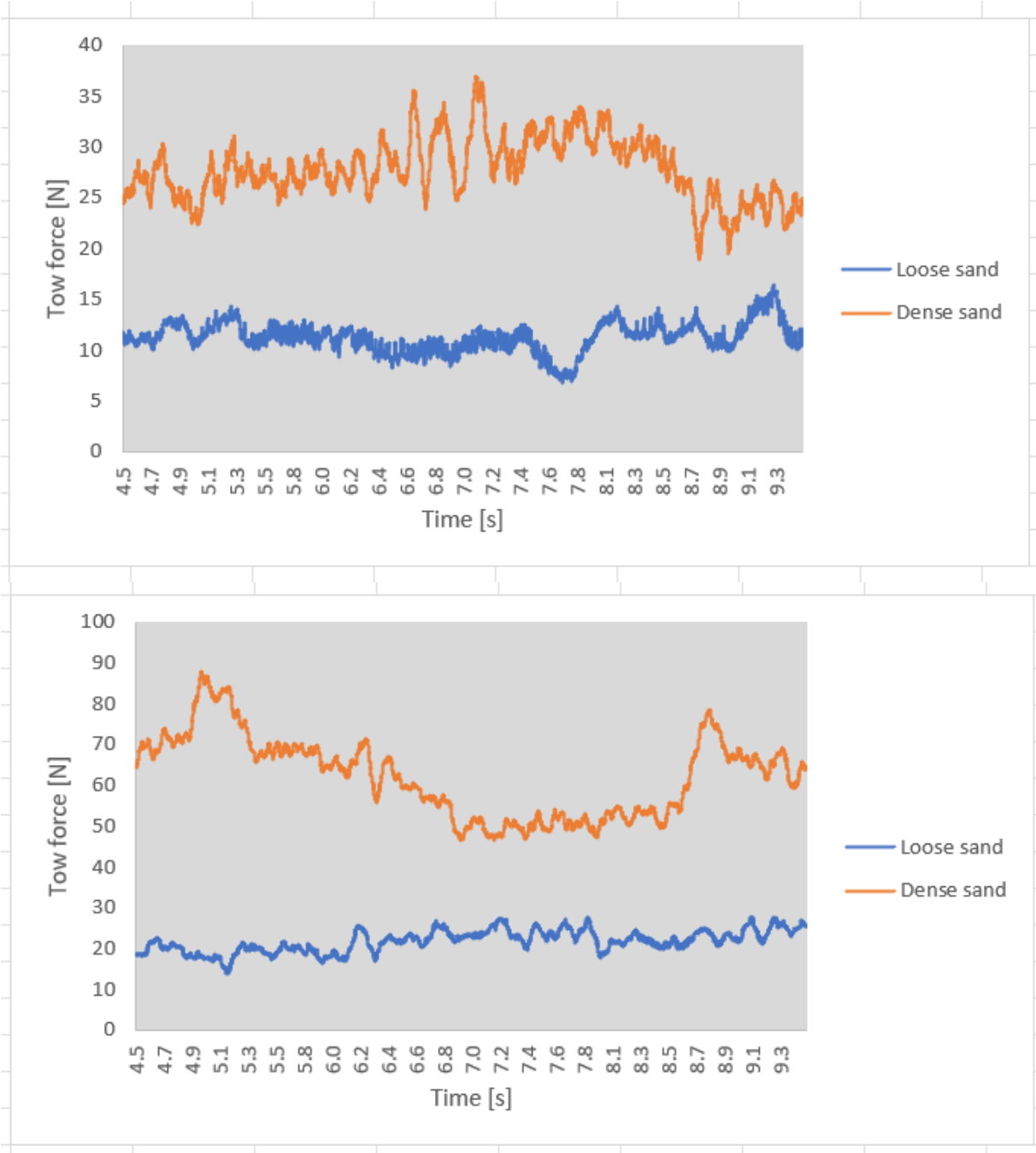


Figure 54: Loose versus dense for the fine grain (test 2 and 17)

There is no constant difference in force for the coarse grain than versus the fine grain as shown in Figure 55.

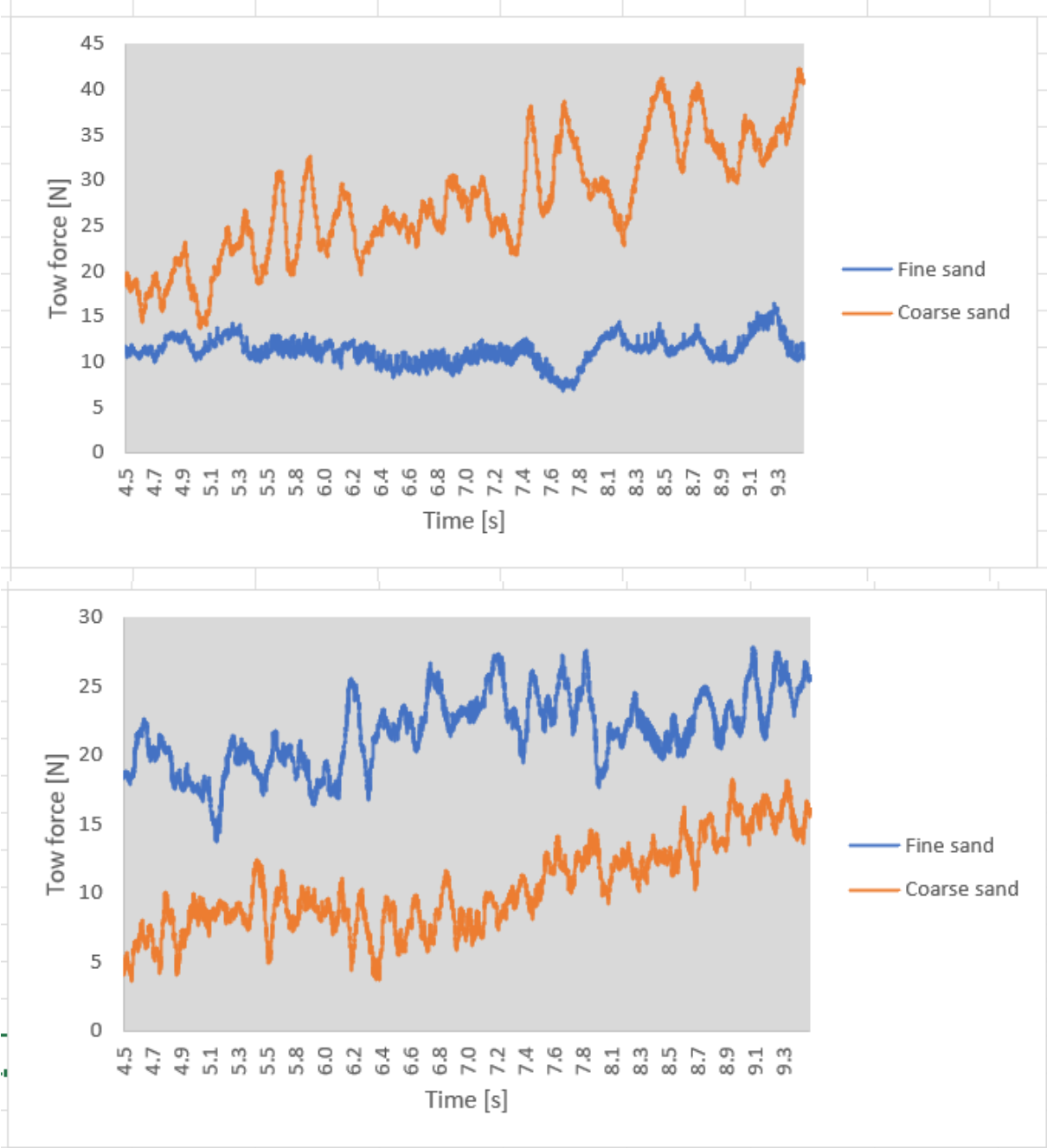


Figure 55: Fine versus coarse grain for loose sand (test 2d and 22e)

The resistance of the system without a chain appeared to be less than 5 N as shown in Figure 56.

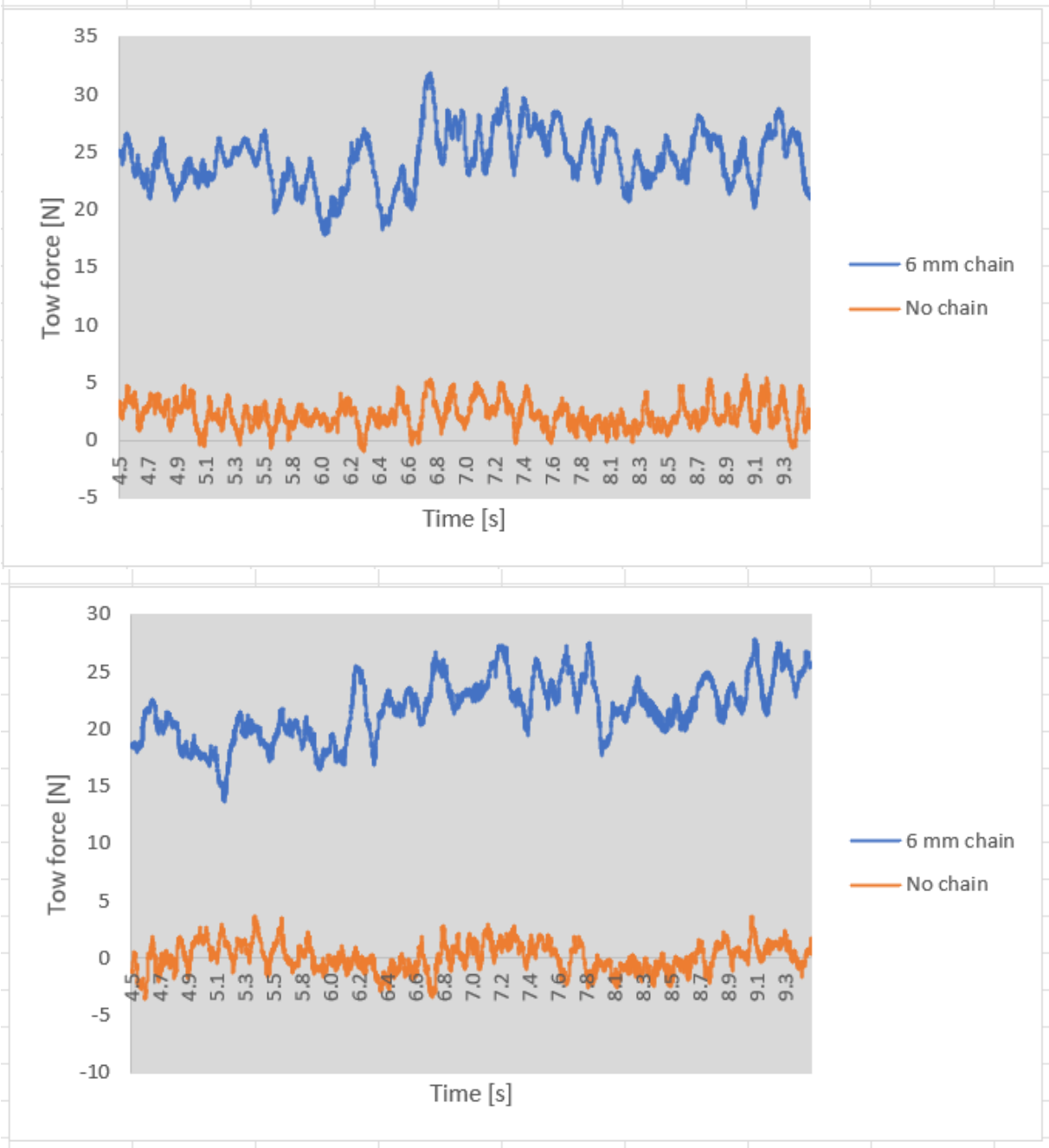


Figure 56: Force versus time for presence and absence of a chain (test 2 and 23)

14.3. Additional comparisons

In this chapter additional comparisons are given. Therefore, the average force in time history for all chains from the tests are used to plot this force versus other parameters like the velocity and angle of attack. This average is calculated for a period of 10 s in which there is the least noise, based on the force versus time history. Finally, these values are averaged for duplicated tests.

For a higher chain link diameter, the increase of the force is steeper with increasing velocity as shown in Figure 57 for the front chain.

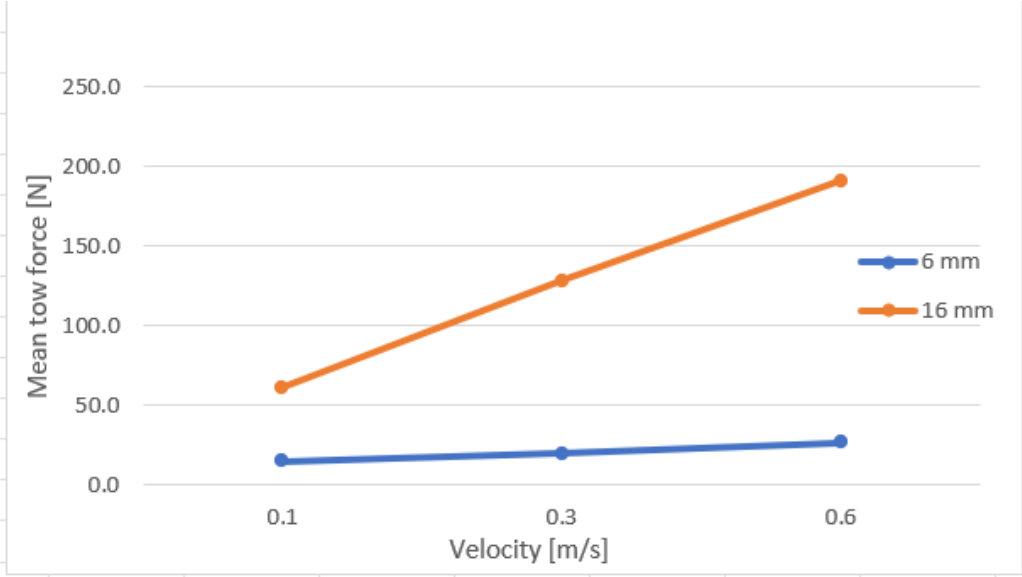


Figure 57: Force versus velocity of attack for different chain link diameters (test 2 and 12a-g) in loose soil

In Figure 58 the force versus angle attack is shown for two different chain link diameters. In this plot the shear force along the chain links is excluded.

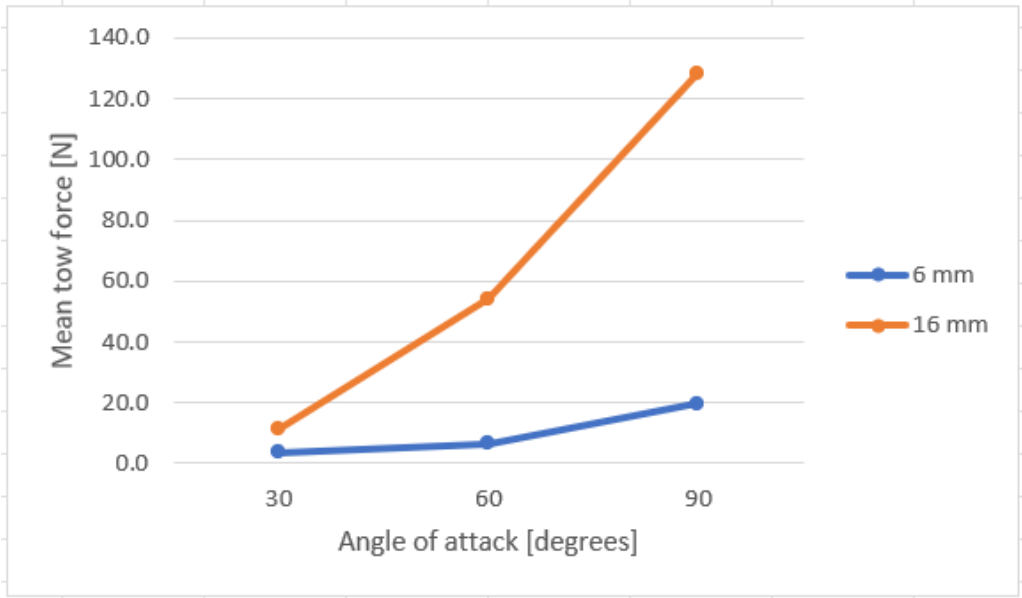


Figure 58: Force against angle of attack for different chain link diameters (test 2, 12h-k, 14, 15) in loose soil

In Figure 59 the force per unit length versus time history is given for the 16 mm chain. In the first test there is a high fluctuation in force for the angle of attack of 90 degrees. In the second

test this force is more constant. The difference in force per unit length is larger than for 6 mm chain, which is given in the previous chapter.

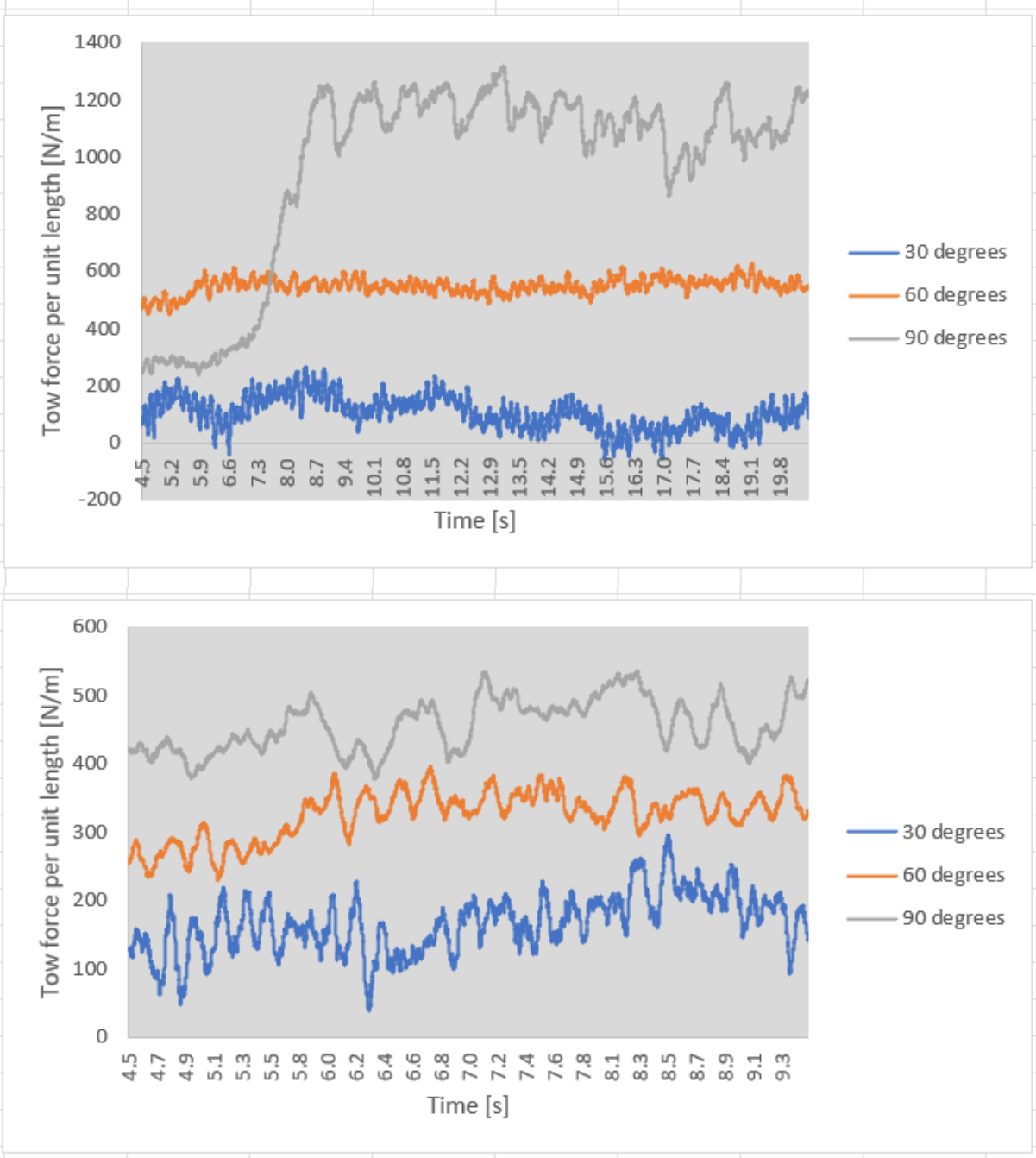


Figure 59: Force per unit length versus time for different angles of attack for the sixteen millimeter chain (test 12a,b,h-k)

Comparing loose sand with dense sand for different velocities as shown in Figure 60, the increase of force is steeper for dense sand than for loose sand.

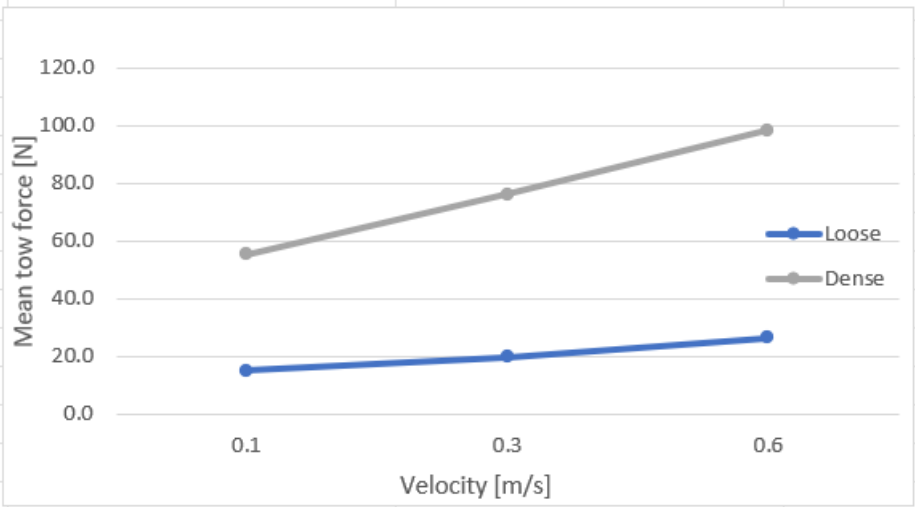


Figure 60: Force against velocity for two different density cases (test 2 and 17)

14.3. Differences between the three chains

In overall the frontal chain experience the highest force. The lowest force is in some cases experienced by the middle chain, while in other cases it is experienced by the back chain, as shown in Table 10.

Test number	Test condition	Force front [N]	Force middle [N]	Force back [N]
2	Fine loose	6.2	2.9	10.6
5	1 cm penetration	59.2	7.7	20.8
6	2 cm penetration	112.4	14.7	29.1
17	Fine dense	51.2	15.4	9.6
22l-m	Coarse loose	20.9	6.1	5.7
22r-s	Coarse dense	47.1	23.6	9.3

Table 10: Differences between the three chains

For dense sand, the force experienced by the front chain is higher than the force experienced by the other two chains as shown in Figure 61.

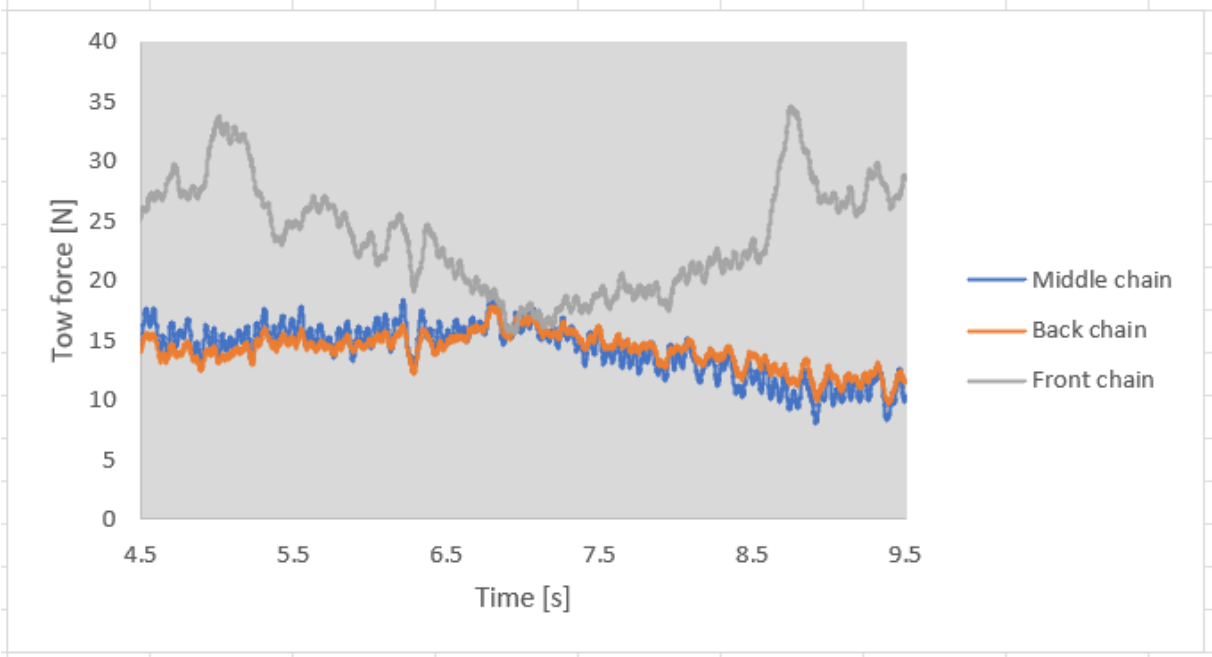


Figure 61: Tow forces for the individual chains in dense sand (test 17g)

14.4. Final calibration

Some results show a difference between the left and right sensor. At the end of the series of tests a calibration has been done to exclude that differences are caused by the load cells themselves. Also the calibration that is given in the specifications of the load cell can be validated. A weight of 2 kg is used to put a force on the sensors as shown in Figure 62.



Figure 62: Calibration setup

In Figure 63, Figure 64 and Figure 65 the force is plotted against time for the different chain holders (back, middle and front). First the weight is attached to the sensor on the right side (sensor 2, 4, 6). After that the weight is replaced to the sensor on the left side (sensor 1, 3, 5). There is hardly any difference between left and right.

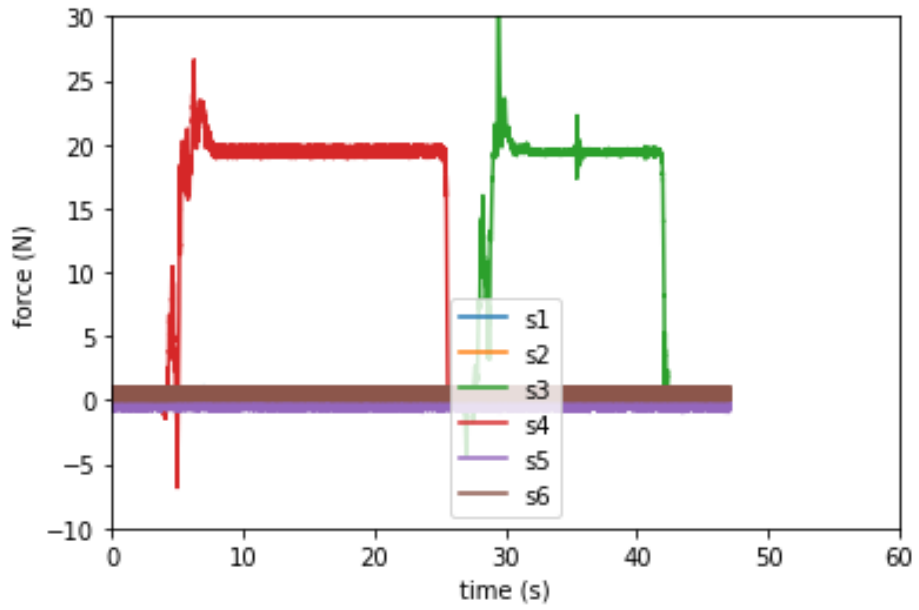


Figure 63: Calibration of the sensors at the back

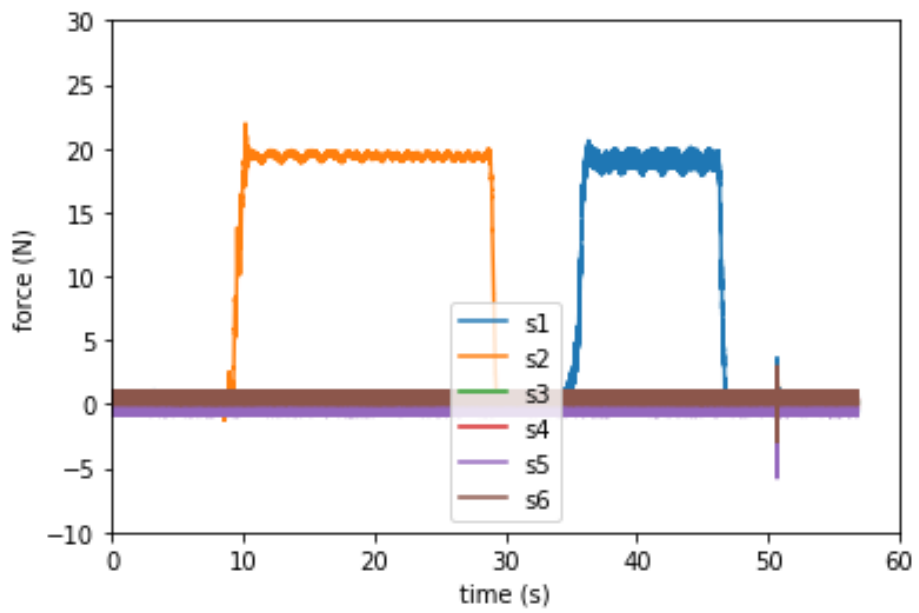


Figure 64: Calibration of the sensors at the middle

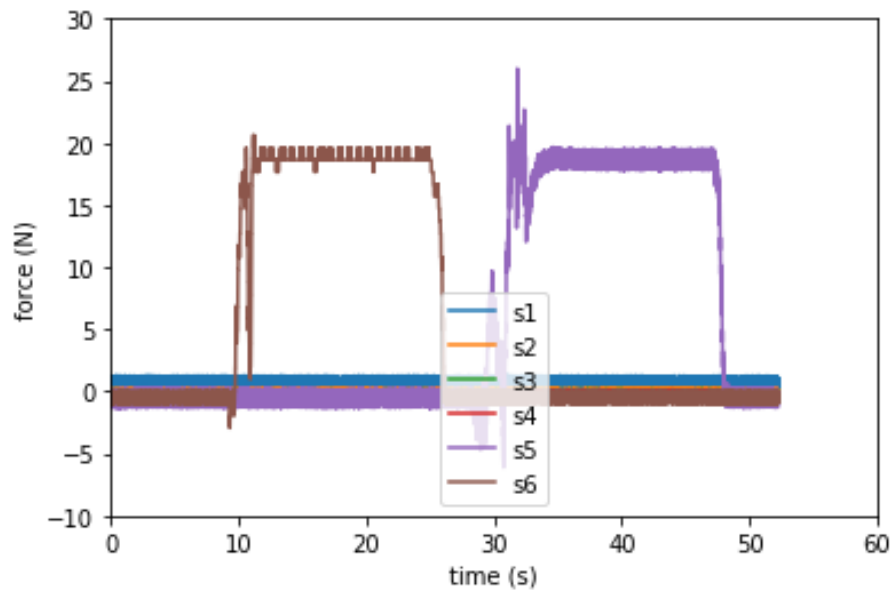


Figure 65: Calibration of the sensors at the front

15. Comparison with theories

In this chapter the results of the experiment are compared with the ploughing theory and the cutting theory. In these comparisons the average forces in the time history of the three individual chains are added together. For both theories the following assumptions are considered:

- Water pressures are absent.
- The initial internal friction angle is 30° .
- The dimensions of the setup in the experiment are considered.

15.1. Ploughing theory

In the calculations for the ploughing theory the following coefficients are used.

- For the dimensionless friction coefficient c_w 0.4 is used (Cathie & Wintgens, 2001).
- For the passive pressure coefficient c_s 3 is used, based on the internal friction angle.
- For the dynamic rate coefficient c_d $0.042 \text{ t}^*h/m^3$ is used (Cathie & Wintgens, 2001).

The dynamic rate coefficient needs to be converted to $\text{N}^*\text{s}/\text{m}^3$ to calculate the force in Newton. The increase is steeper for ploughing theory than for the experiment as shown in Figure 66.

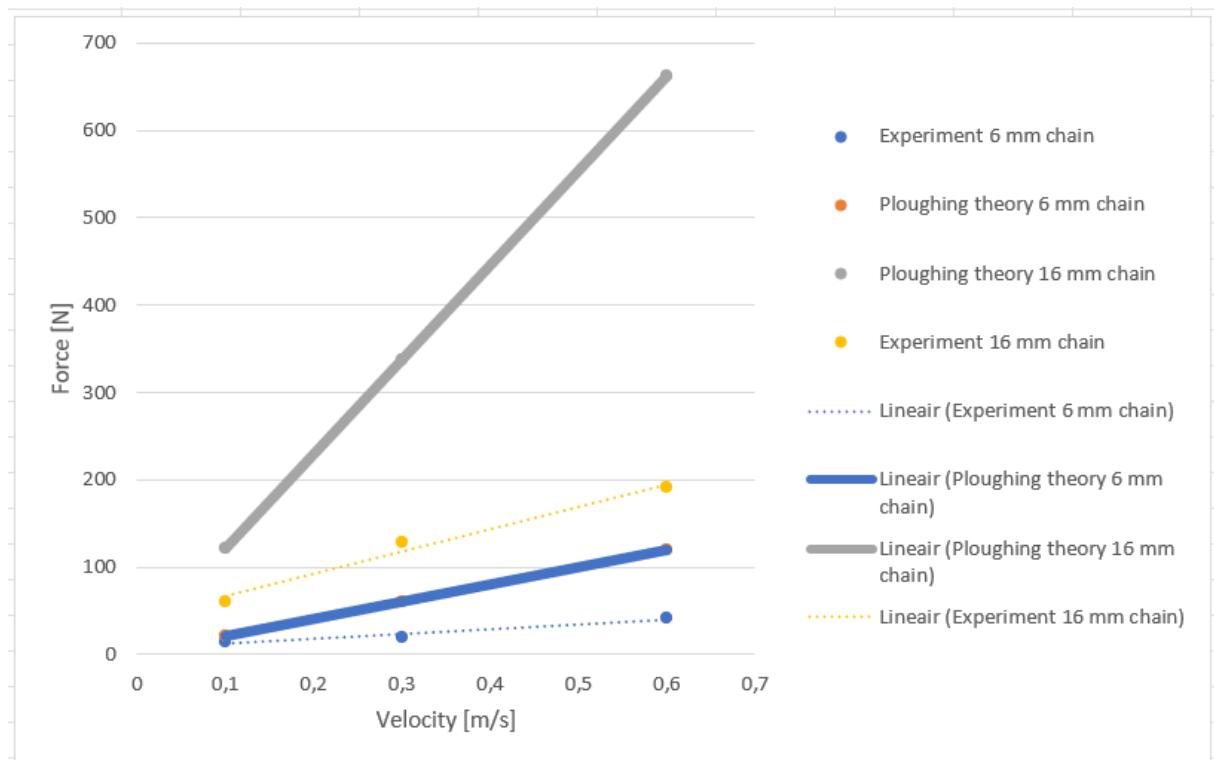


Figure 66: Plough force versus plough velocity for two chain link diameters, experimental data (test 1, 2, 3 and 12) and ploughing theory

The same holds for the increase of the penetration depth. The increase of the force is steeper for the ploughing theory than for the experiment as shown in Figure 67.

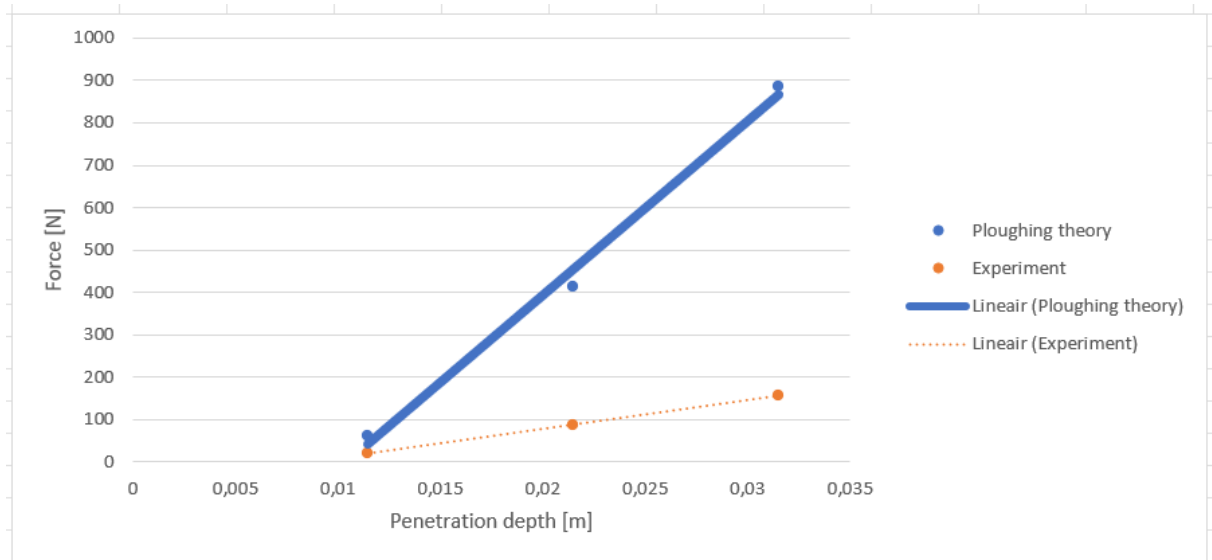


Figure 67: Plough force versus penetration depth, experimental data (test 2, 5 and 6) and ploughing theory for a velocity of 0.3 m/s

The dynamic rate coefficient is uncertain and therefore a comparison is hard to make. Cathie & Wintgens determined this coefficient on the basis of plough test results and backward calculations for different grain sizes and densities. The grain sizes are given as d_{10} , densities are not specified. The effect of the increase of the penetration depth is larger for the ploughing theory than for the experiment.

15.2. Cutting theory

Loose sand could be modelled using the dry sand theory. For dry sand, the cutting force can be calculated using Miedema's wedge theory for dry sand, because of the large blade angle. In these calculations the additional assumptions are:

- The external friction angle is $2/3$ of the internal friction angle.
- The internal friction angle on the pseudo blade is the same as the internal friction angle on the blade.

In Figure 68 the tow force against the tow velocity is plotted for the cutting theory and for the experiment. The 16 mm chain doesn't seem to match with the theory for high velocities.

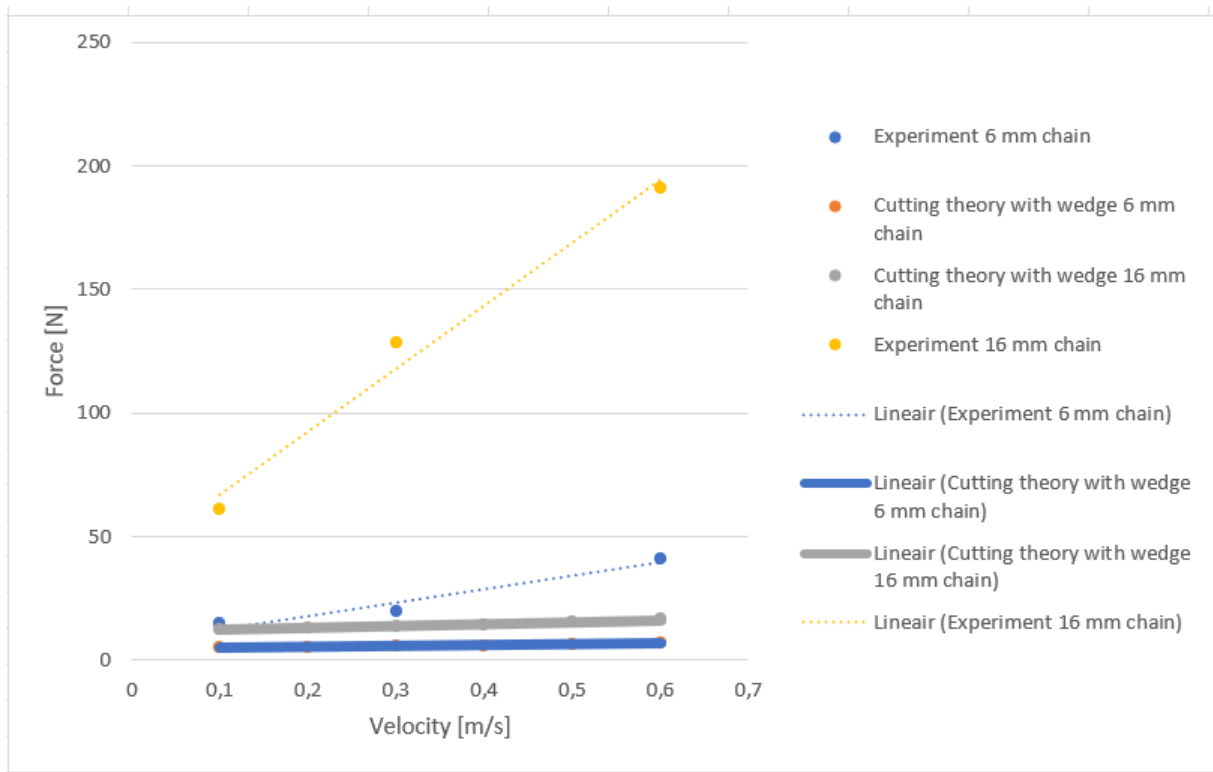


Figure 68: The tow force against the tow velocity for different chain link diameters, experimental data (test 1, 2, 3 and 12) and cutting theory

In

Figure 69 the tow force against the penetration depth is plotted for the cutting theory and the experiment. For an increase of the penetration depth the increase of the force is much steeper for the experiment than for the cutting theory.

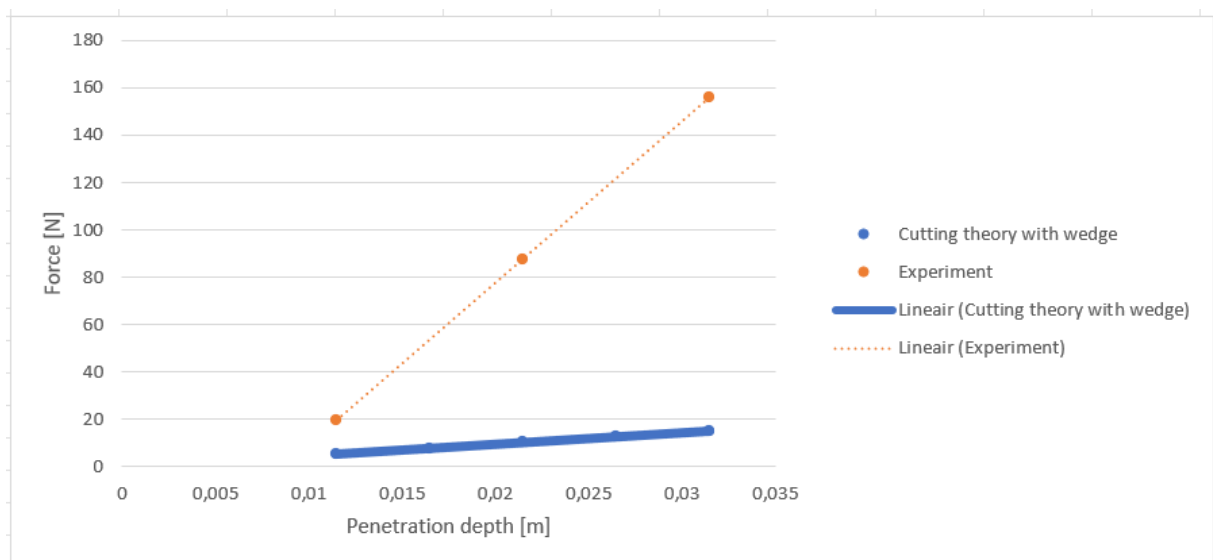


Figure 69: The tow force against the penetration depth for the experimental data (test 2, 5 and 6) and the cutting theory for a velocity of 0.3 m/s

In the cutting theory, the effect of the increase of the penetration depth is smaller than for the experiment, contrary to the ploughing theory.

15.3. Consolidation

A possible explanation of the differences between the theories and the experiment can be the degree of consolidation. The water pressures are not measured during the experiment. According to Verruijt the value of the consolidation coefficient c_v for sand used in the experiment is between 0.01 and 0.1 m^2/s . For both the 6 mm as the 16 mm chain the value for $c \cdot t/h^2$ is higher than 2 (the minimum value is 3.8), which means that the degree of consolidation $U = 1$ (see Figure 15). More details on the calculation can be found in Appendix XI in Table 14 and Table 15. *Table 14: Minimum value of the consolidation coefficient for both chain link diameters.* So, for both chain link diameters the soil can be considered as drained. For both the ploughing theory and the cutting theory calculation the sand is assumed to be dry, without influence of water pressures. That means that the difference in force is not caused by a difference in consolidation.

15.4. Influence of the internal friction angle

In Figure 60 a large difference is shown for a relatively small increase of density is visible. One possible explanation for the increase of the force for dense soil caused by densifying or having a deeper penetration of the chain is that these change in conditions have an influence on the internal friction angle. As shown in Figure 70 for a low confining pressure (less than 10 kPa for the experiment, see also Appendix XI, Table 16) a relatively small change in density yields a high change in internal friction angle (Bolton, The strength and dilatancy of sands, 1986). In Figure 70 the pressure coefficients against the internal friction angle are plotted. An increase of the internal friction angle leads to an exponential increase of the passive pressure coefficient K_p as shown in Figure 70. Passive soil pressure is soil pressure caused by an external force, like a tow force as in the experiment.

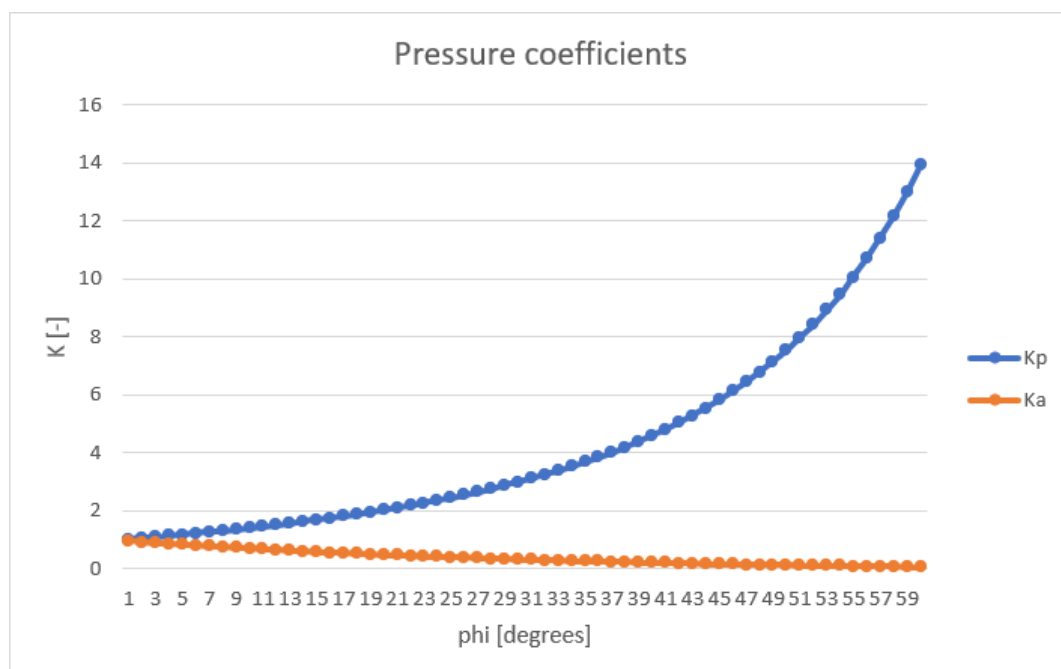


Figure 70: Pressure coefficients versus internal friction angle

In the theories the internal friction angle is defined independent of the density and penetration depth, when in fact it is increasing for higher densities according to Bolton. This can be an explanation of the differences between the experiment and the theoretical data. In Figure 71 and

Figure 72 the comparison between the experimental data and the cutting theory is made again, but now with a higher value of 50° for the internal friction angle in the cutting theory.

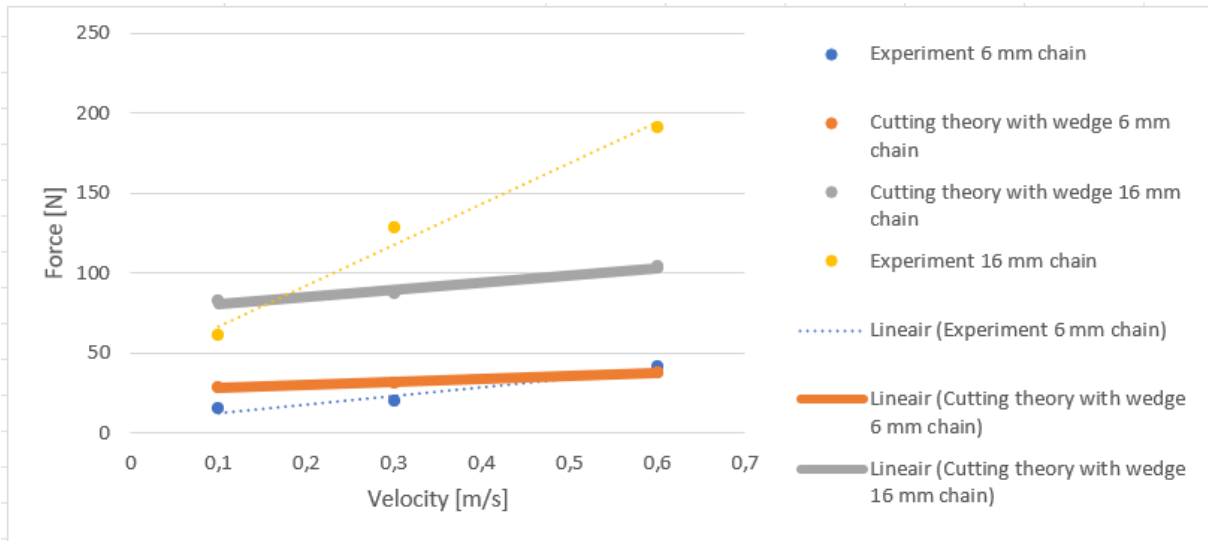


Figure 71: The tow force against the tow velocity for different chain link diameters, experimental data (test 1, 2, 3 and 12) and cutting theory for an internal friction angle of 50°

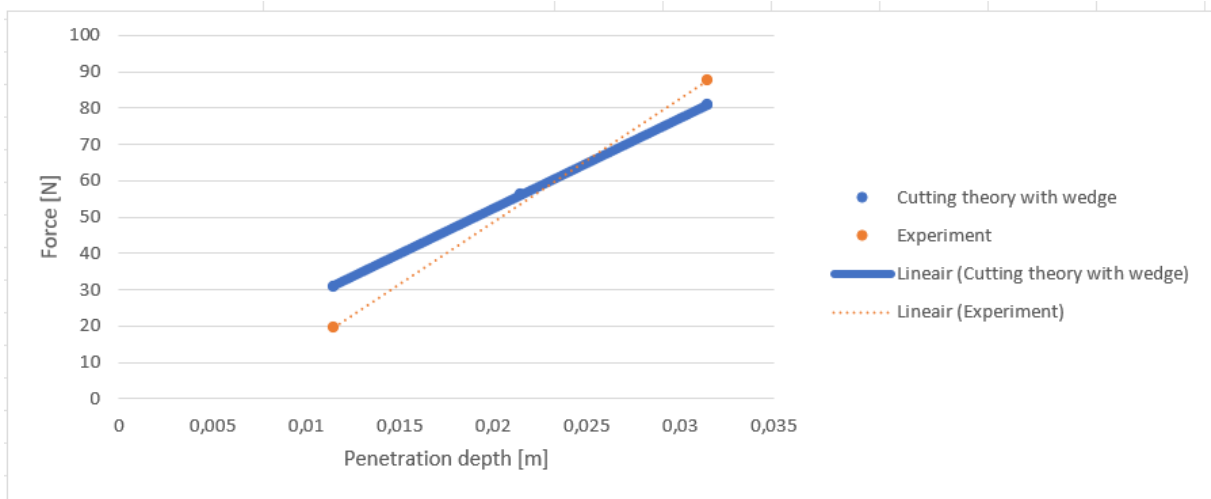


Figure 72: The tow force against the penetration depth, experimental data (test 2, 5 and 6) and cutting theory for an internal friction angle of 50°

16. Dimensionless forces

There are five parameters involved in the experiment: the force (per unit length), density, gravity, penetration depth and velocity. The length of the chain is fixed and therefore combined with the force, this parameter becomes the force per unit length. These parameters use three basic units: meters, seconds and kilograms as shown in Table 11. According to the Buckingham Pi theorem two dimensionless Pi groups are needed to describe this problem.

Parameter	SI unit
Force per unit length	kg*m*s ⁻³
Density	kg*m ⁻³
Gravity	m*s ⁻²
Penetration depth	m
Velocity	m*s ⁻¹

Table 11: Parameters and corresponding units

The first group is the dimensionless tow force. The force is made dimensionless by dividing the measured force by the weight of the soil as shown in Equation 47 (Guo & Stolle, Lateral pipe–soil interaction in sand with reference to scale, 2005). The weight of the soil resists moving it and therefore it affects the towing. Because the measured force from the experiment is in Newtons instead of Newton per meter as used by Guo and Stolle (unit of their ultimate force), the penetration depth is squared for the weight of the soil.

$$F_d = \frac{F}{\rho_s g L h_i^2} \quad (47)$$

F_d	dimensionless force [-]
F	average tow force from experiment [N]
ρ_s	density of the soil [kg/m ³]
g	gravitational constant [m/s ²]
L	length of the chain [m]
h_i	penetration depth of the chain [m]

The weight of the soil is now defined as the gravitation acting on a beam of soil that needs to be lifted to allow the chain to pass as shown in Figure 73. The length of this beam equals the length of the chain.

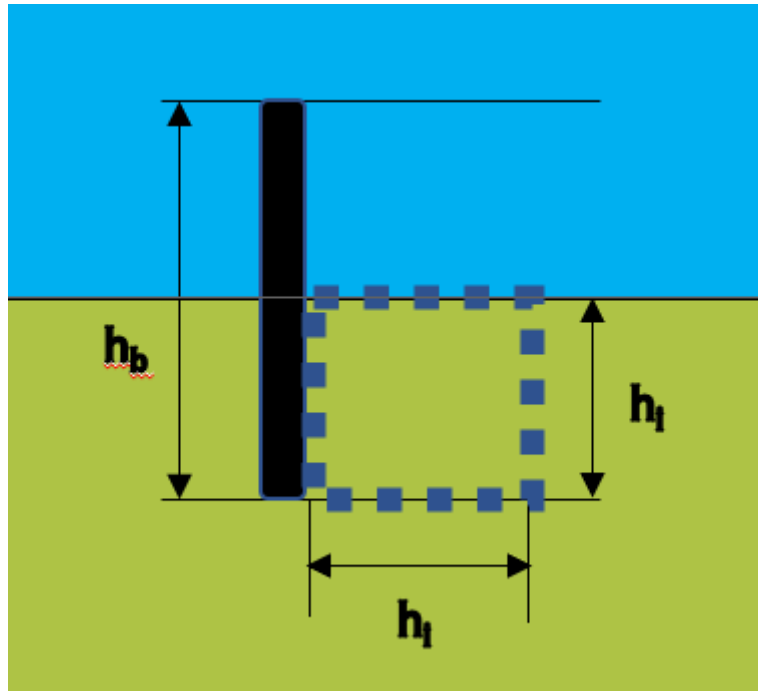


Figure 73: Definition in 2D of the beam of soil that needs to be removed

The second group is the Froude number. Besides the weight of the soil, there is also inertia that affects the towing. because the soil needs to accelerate. The used velocity is made dimensionless by using the Froude number with the chain link diameter as length parameter as shown in Equation 48. The Froude number represents the ratio between the inertia of the mobilized soil and the gravitation acting on the same soil element.

$$Fr = \frac{V}{\sqrt{g h_i}} \quad (48)$$

Fr	Froude number
V	tow velocity [m/s]
g	gravitational constant [m/s ²]
h _i	penetration depth [m]

In Figure 74 the dimensionless force is plotted against the Froude number. The force from the experiment is the summation of the force acting on the three individual chains. This is done to decrease the noise in the data. The blue line shows that increase of density leads to a much higher force. Note that the three individual chains experience different densities in this case. The yellow line represents the force of the front chain only, multiplied by a factor 3 to make it comparable with the other lines.

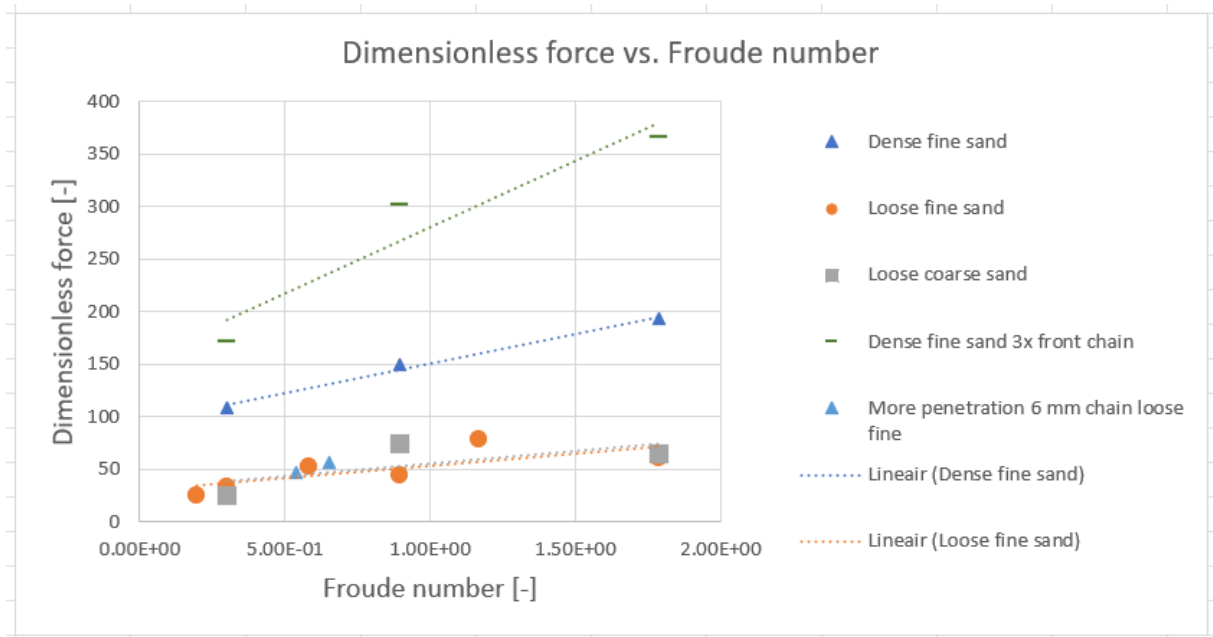


Figure 74: Dimensionless force versus the Froude number for experimental data (test 1, 2, 3, 5, 6, 12, 17, 22)

In Figure 75 the data of Figure 74 is given again, however an extra line in orange is added with the dimensionless force for dense front chain case (the yellow line) divided with a factor 5.2. This factor represents the average increase of the passive pressure coefficient for a denser soil with an internal friction angle of 62° according to Figure 70. The orange line matches well with the data for loose soil, so the increase of the passive pressure coefficient could be a good explanation for the higher values of the dense soil.

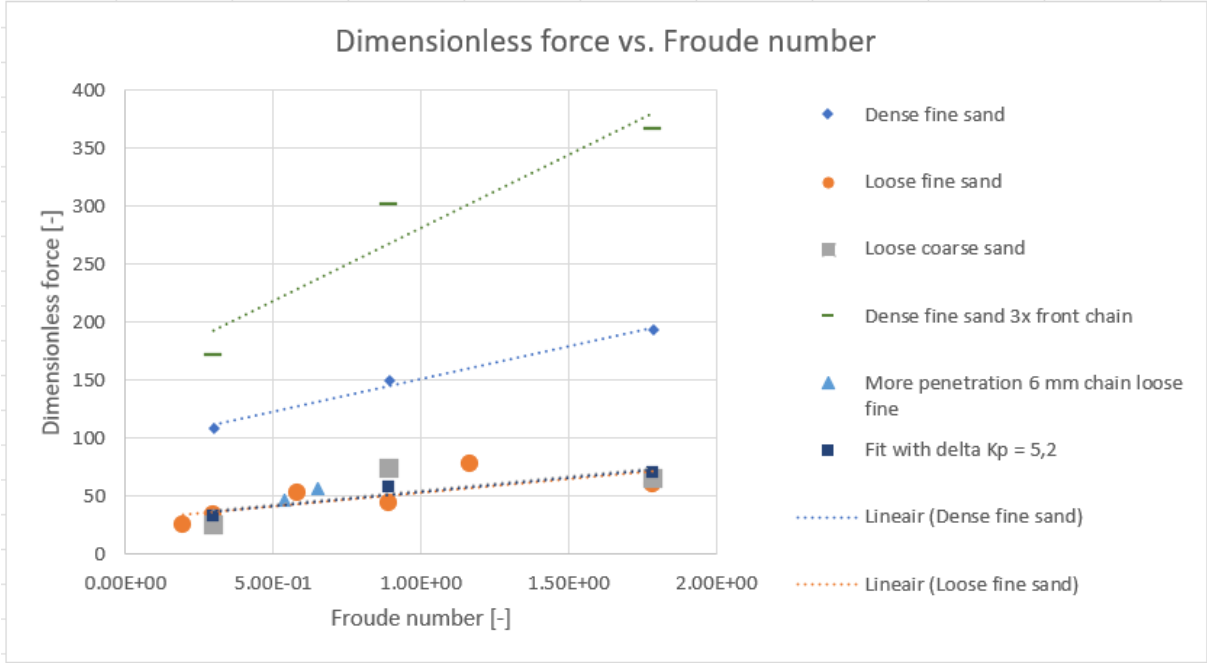


Figure 75: Dimensionless force versus the Froude number for experimental data (test 1, 2, 3, 5, 6, 12, 17, 22)

In Figure 76 the increase of the passive pressure coefficient defined as the ratio between the actual passive pressure coefficient with respect to its initial value ($K_{p,loose}$), is integrated in the weight of the soil. In Equation 48 this modification on Equation 46 is shown.

$$F_d = \frac{F}{\frac{K_p}{K_{p,loose}} K_{p,loose} \rho_s g L h_i^2} = \frac{K_{p,loose}}{K_p} \frac{F}{K_{p,loose} \rho_s g L h_i^2} \tag{49}$$

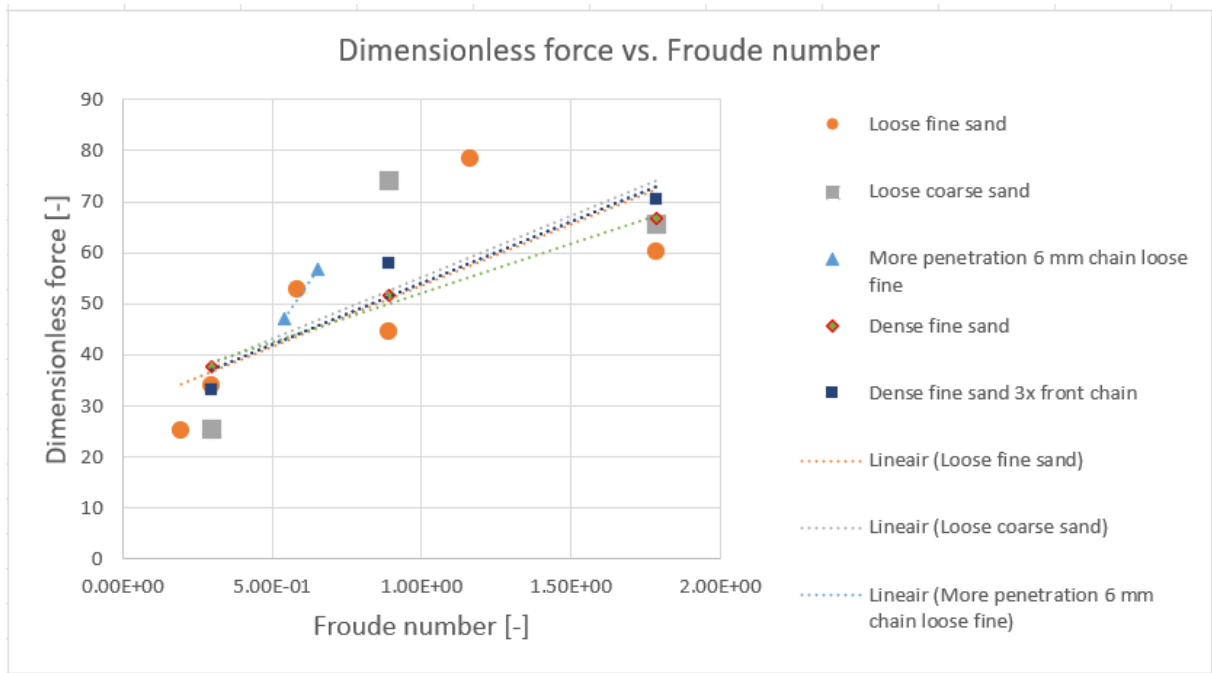


Figure 76: Dimensionless force versus the Froude number corrected with passive pressure coefficient for experimental data (test 1, 2, 3, 5, 6, 17, 22)

In Figure 76 the initial value of the passive pressure coefficient K_p is 1. A common value for the internal friction angle is 30° , resulting in a passive pressure coefficient of 3. In Figure 77 is shown that the dimensionless force decreases with a factor 3, but the trend remains the same.

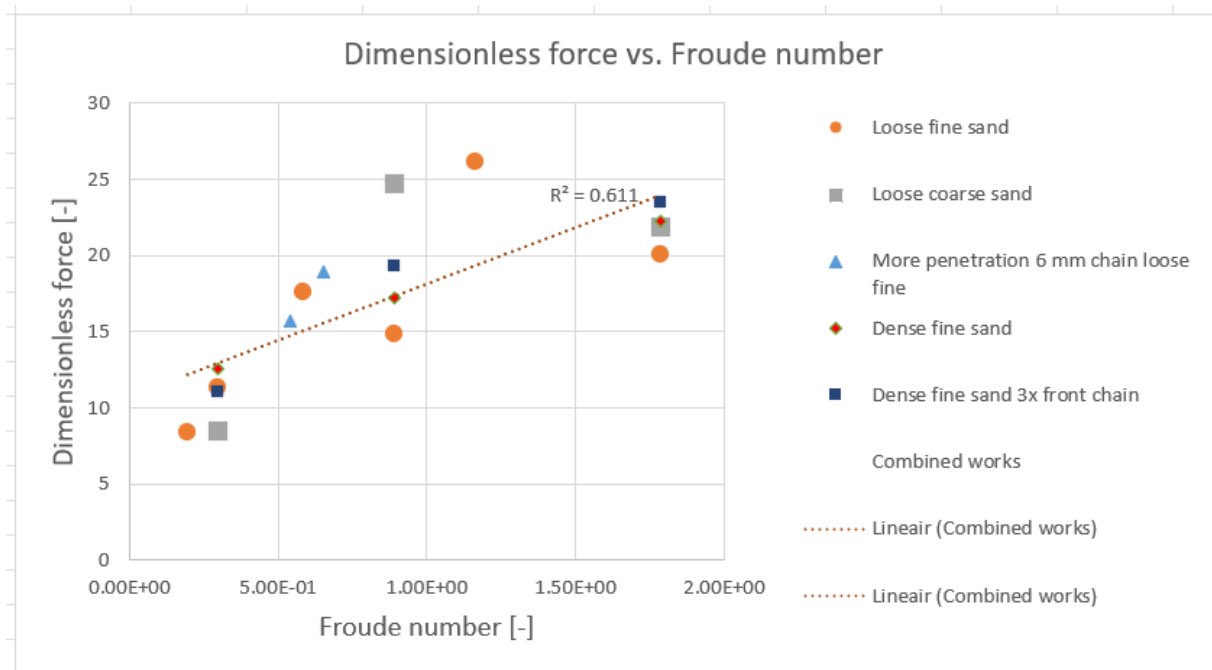


Figure 77: Dimensionless force versus the Froude number corrected with passive pressure coefficient for experimental data (test 1, 2, 3, 5, 6, 17, 22)

One trend curve for the dimensionless tow force versus the Froude number could be made. This curve can be used as an indicator for further chain designs.

17. Conclusion and discussion

Not all test results are in line with the cutting theory. The results for the 16 mm chain tests and the dense tests are higher than expected. An increase of density can lead to significant higher forces for fully drained soil. This can be certified with the significant increase of the internal friction for low confining pressures according to Bolton's theory, resulting in a higher value for the passive pressure coefficient. Cathie & Wintgens also mention an increase of the passive pressure coefficient for higher densities. Based on the two defined dimensionless groups, namely the Froude number and the ratio between the measured force and the weight of the soil, a linear trend line represents the data for loose soil. The increase of the force for dense soil can be clarified by an increase of the passive pressure coefficient, which is quite possible according to Bolton. An estimate for the increase of the passive pressure coefficient can include the data for dense soil on this trendline. It represents the data with reasonable accuracy of $R^2 = 0.611$.

For small angles of attack, the decrease in force cannot be explained solely by the decrease of the corresponding projected length. Further research on possible cutting mechanisms that take place can be done.

The influence of the internal friction angle is a possible explanation for the increase in force for dense soil. Additional measurements on the internal friction angle or the passive pressure coefficient can be done on this parameter after densifying the soil or increasing the penetration depth to verify the estimate of this increase.

In the experiments the force is measured in longitudinal direction. Additional experiments can be done to measure the force in vertical direction. This force can give more insight in terms of the penetration depth. This parameter was fixed in these experiments, but it varies in reality. The ratio between this force and the weight of the chain can give more insight in the chain behaviour.

Bibliography

- Albiker, J., Achmus, M., Frick, D., & Flindt, F. (2017). 1g Model tests on the displacement accumulation of large-diameter piles under cyclic lateral loading. *Geotechnical testing journal*.
- Bolton, M. (1986). The strength and dilatancy of sands. *Geotechnique* 36, No. 1., pp. 65-78.
- Bolton, M. (1986). The strength and dilatancy of sands. *GCotechnique* 36, No. 1., pp. 65-78.
- Boomkor. (2022, September 2). Retrieved from Goede vissers:
https://www.goedevissers.nl/vis_van_goede_vissers/vismethodes.html?id=49
- Broadhurst, M. (2021). *Improving penaeid-trawl efficiencies via ground gear with tickler chains*.
- Cathie, D., & Wintgens, J. (2001). *Pipelin trenching using plows: performance and geotechnical hazards*. Houston.
- Creutzberg, F., Duineveld, G., & Noort, G. v. (1987). The effect of different numbers of tickler chains on beam-trawl catches. *ICES journal of marine science*, 159-168.
- Depestele, J., & e.a. (2016). Measuring and assessing the physical impact of beam trawling. *ICES Journal of Marine Science* 73 (Supplement 1), pp. i15–i26.
- Eigaard, O., & e.a. (2016). Estimating seabed pressure from demersal trawls, seines and dredges based on gear design and dimensions vol 73. *ICES Journal of Marine Science*, pp. i27–i43.
- Enerhaug, B. (2011). Contact forces between seabed and fishing gear components. *Contributions on the theory of fishing gears and related marine systems vol. 7*, pp. 237-246.
- Esmaeili, M., & Ivanovic, A. (2014). Numerical modelling of bottom trawling ground gear element on the seabed. *Ocean engineering* 91, 316-328.
- Foglia, A., & Ibsen, L. (2014). Bucket foundations: a literature review. *DCE Technical Report No. 176*.
- Guo, P., & Stolle, D. (2005). Lateral pipe–soil interaction in sand with reference to scale. *J. Geotech. Geoenviron. Eng.* 131(3), pp. 338-349.
- Guo, P., & Stolle, D. (2005). Lateral pipe-soil interaction in sand with reference to scale effect. *Journal of Geotechnical and Geoenvironmental Engineering*, 131(3), pp. 338–349.
- Hirsch, C. (2007). *Numerical computation of internal & external flows: Volume 1 the fundamentals of computational fluid dynamics*. Elsevier.

- Huysmans, M., & Dassargues, A. (2005). Review of the use of Péclet numbers to determine the relative importance of advection and diffusion in low permeability environments. *Hydrogeology Journal* volume 13, pp. 895–904.
- Ivanovic, A., & e.a. (2015). *Predicting the physical impact by towed demersal gears from fishing gear characteristics*.
- Ivanovic, A., & O'Neill, F. (2015). Towing cylindrical fishing gear components on cohesive soils. *Computers and geotechnics* 65, pp. 212-219.
- Miedema, S. (2014). *The Delft sand, clay & rock cutting model*. Amsterdam: IOS Press.
- Penca, J. (2022). *Science, precaution and innovation for sustainable fisheries: the judgement by the Court of Justice of the EU regarding the electric pulse fishing ban*.
- Rhee, C. v., & Steeghs, H. (1991). Multi-blade ploughs in saturated sand; model cutting tests. *Dredging and port construction*.
- Rijnsdorp, A., & e.a. (2017). *Assessing and mitigating impact of bottom trawling*.
- Rijnsdorp, A., & e.a. (2021). *Sediment mobilization by bottom trawls: a model approach applied to the Dutch North Sea beam trawl fishery*.
- Roy, K., Hawlader, B., Kenny, S., & Moore, I. (2016). *Finite element modeling of lateral pipeline–soil interactions in dense sand*.
- Schriek, G. v. (2014). *Dredging technology*. Aerdenhout: GLM van der Schriek.
- Verruijt, A. (2006). *Offshore soil mechanics*. Delft.
- Verruijt, A. (2006). *Offshore soil mechanics*. Papendrecht.
- Verruijt, A., & Broere, W. (2012). *Grondmechanica*. Delft: VSSD.
- Vissen met korren*. (2022, March 22). Retrieved from Vist ik het maar!: <https://vistikhetmaar.nl/onderwijs/lesmodules/vissen-met-korren-2/>
- White, D., Cheuk, C., & Bolton, M. (2008). The uplift resistance of pipes and plate anchors buried in sand. *Geotechnique* 58, No 10, pp. 771-779.
- White, F. (2011). *Fluid mechanics*. McGraw Hill.
- Woesnner, W., & Pieter, E. (2020). *Hydrogeologic properties of earth materials and principles of groundwater flow*. Guelph: Groundwater Project.

Appendix I: Soil mechanical scaling

Lauder described scaling laws for a pipeline plough study (Lauder, 2010). In Table 12 scale factors are given for several quantities.

Quantity	Scale factor
Length	$1/N$
Stress	$1/N$
Mass	$1/N^3$
Force	$1/N^3$
Viscosity	1
Permeability	1

Table 12: Scale factors (Lauder, 2010)

Appendix II: Mapping of the density of silica sands

A classification of silica sands is given in Table 13. (Lauder, 2010)

Description	Relative density [%]	Cone resistance [MPa]
Very loose	<15	<0.6
Loose	15-25	0.6-1.5
Medium	35-65	1.5-7.0
Dense	65-85	7.0-16
Very dense	85-100	>16

Table 13: Relative density and cone resistance (Lauder, 2010)

Appendix III: Cutting coefficients

Dimensionless parameter describing the contribution of the inertial forces (Miedema, 2014)

$$\lambda_i = \frac{V_c^2}{g h_i} \frac{\rho_s - \rho_w}{\rho_s} \tag{50}$$

- V_c cutting velocity
- g gravitational constant
- h_i layer tickness
- ρ_s density of soil
- ρ_w density of water

Fraction of the inertial force contributing to the horizontal force (Miedema, 2014)

$$f_i = \frac{1}{1 - e^{-2 \log(\lambda_i/5)}} \tag{51}$$

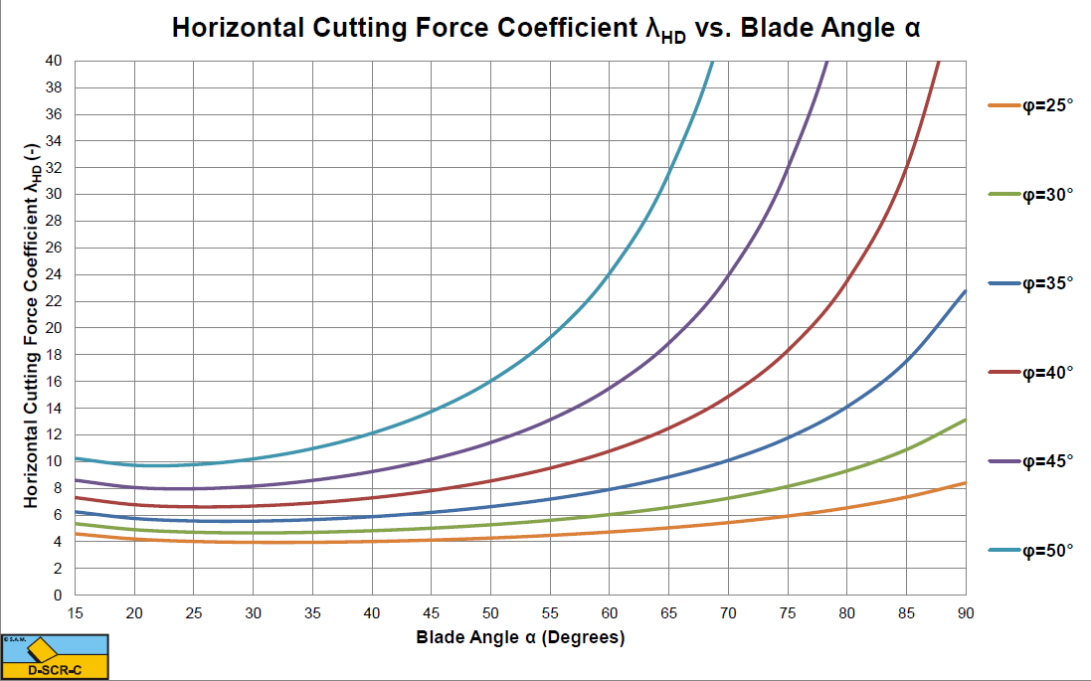


Figure 78: Horizontal cutting force coefficient for $h_b/h_i = 2$ (Miedema, 2014)

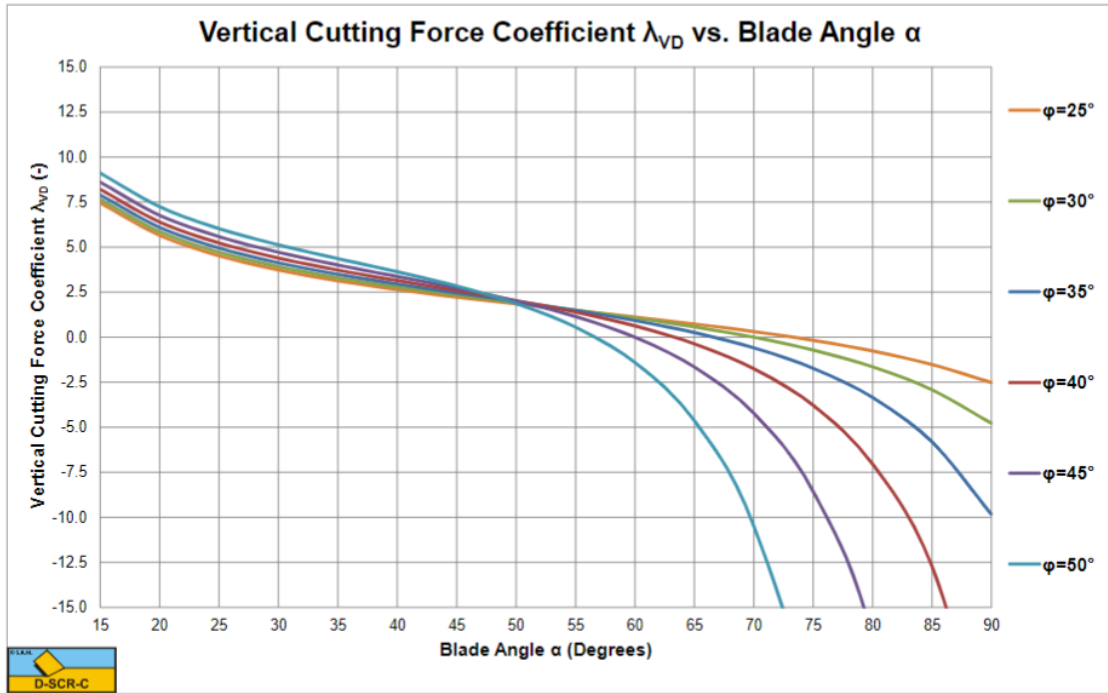


Figure 79: Vertical cutting force coefficient for $h_b/h_i = 2$ (Miedema, 2014)

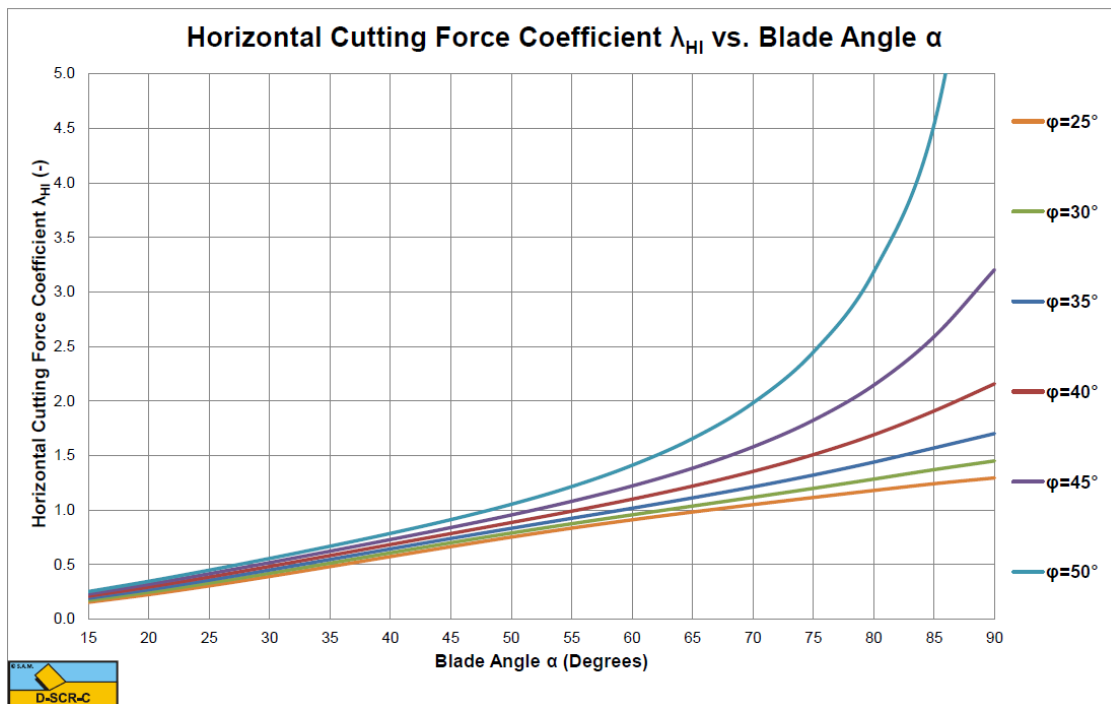


Figure 80: Horizontal cutting force coefficient for inertia effects (Miedema, 2014)

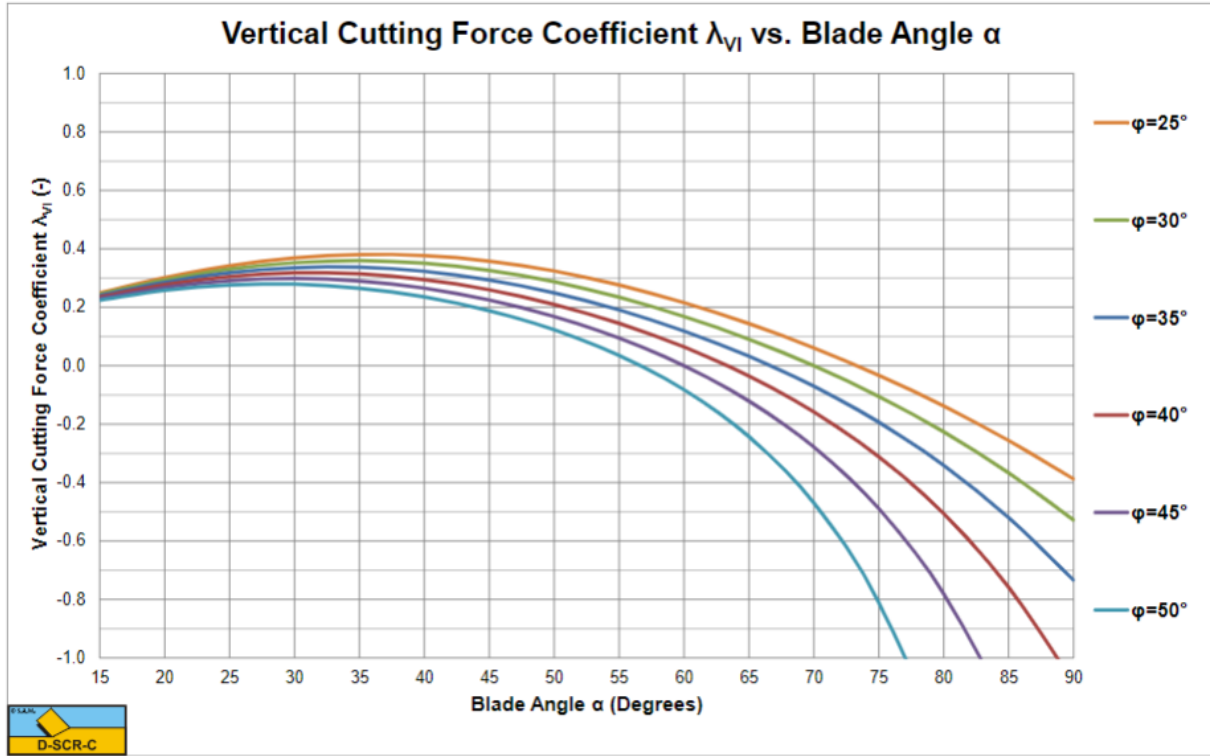


Figure 81: Vertical cutting force coefficient for inertia effects (Miedema, 2014)

In these equations 1 stands for the horizontal direction and 2 stands for the vertical direction.

Non cavitating cutting process (Miedema, 2014)

$$c_1 = \frac{\left(p_{1m} \frac{\sin \varphi}{\sin \beta} + p_{2m} \frac{h_b \sin(\alpha + \beta + \varphi)}{h_i \sin \alpha} \right) \sin(\alpha + \delta)}{\sin(\alpha + \beta + \delta + \varphi)} - p_{2m} \frac{h_b \sin \alpha}{h_i \sin \alpha} \quad (52)$$

$$c_2 = \frac{\left(p_{1m} \frac{\sin \varphi}{\sin \beta} + p_{2m} \frac{h_b \sin(\alpha + \beta + \varphi)}{h_i \sin \alpha} \right) \cos(\alpha + \delta)}{\sin(\alpha + \beta + \delta + \varphi)} - p_{2m} \frac{h_b \cos \alpha}{h_i \sin \alpha} \quad (53)$$

p_{1m}	average pore pressure in the shear zone
p_{2m}	average pore pressure on the blade
h_b	blade height
h_i	initial layer thickness
α	blade angle
β	shear angle
δ	soil/steel interface / external friction angle
φ	angle of internal friction

Cavitating cutting process (Miedema, 2014)

$$d_i = \frac{\left(\frac{\sin \varphi}{\sin \beta} + \frac{h_b \sin(\alpha + \beta + \varphi)}{h_i \sin \alpha}\right) \sin(\alpha + \delta)}{\sin(\alpha + \beta + \delta + \varphi)} - \frac{h_b \sin \alpha}{h_i \sin \alpha} \quad (54)$$

$$d_2 = \frac{\left(\frac{\sin \varphi}{\sin \beta} + \frac{h_b \sin(\alpha + \beta + \varphi)}{h_i \sin \alpha}\right) \cos(\alpha + \delta)}{\sin(\alpha + \beta + \delta + \varphi)} - \frac{h_b \cos \alpha}{h_i \sin \alpha} \quad (55)$$

Appendix IV: Water pressure forces and grain forces

Weights in dry sand (Miedema, 2014)

$$G_1 = \rho_s g h_i w \frac{\sin(\alpha + \beta)}{\sin \beta} \left(\frac{h_b + h_i \sin \alpha}{\sin \alpha} + \frac{h_i \cos(\alpha + \beta)}{2 \sin \beta} \right) \quad (56)$$

$$G_2 = \rho_s g \frac{h_b^2}{2} \left(\frac{1}{\tan \theta} - \frac{1}{\tan \alpha} \right) w \quad (57)$$

ρ_s	density of soil
ρ_w	density of water
w	width of the blade
α	blade angle
β	shear angle
φ	angle of internal friction
θ	wedge angle

The grain forces for dry sand (Miedema, 2014)

$$K_1 = \frac{G_1 \sin(\alpha + \lambda) + I \cos(\alpha + \beta + \lambda)}{\sin(\alpha + \beta + \lambda + \varphi)} \quad (58)$$

$$K_2 = \frac{G_1 \sin(\beta + \varphi) + I \cos \varphi}{\sin(\alpha + \beta + \lambda + \varphi)} \quad (59)$$

$$K_3 = \frac{K_2 \sin(\alpha + \delta - \theta - \lambda) + G_2 \sin(\alpha + \delta)}{\sin(\alpha + \delta + \varphi)} \quad (60)$$

$$K_4 = \frac{K_2 \sin(\theta + \lambda + \varphi) + G_2 \sin \varphi}{\sin(\alpha + \delta + \varphi)} \quad (61)$$

I	inertial force on the shear plane
λ	angle of internal friction between wedge and layer cut

The force W_1 is the water pressure force acting on the shear plane. In a situation without cavitation the water pressure forces can be determined using Equation 45-48 (Miedema, 2014).

$$W_1 = \frac{p_{1m} \rho_w g V_c h_i^2 \epsilon w}{k_{max} \sin \beta} \quad (62)$$

$$W_2 = \frac{p_{2m} \rho_w g V_c h_i h_b \epsilon w}{k_{max} \sin \theta} \quad (63)$$

$$W_3 = \frac{p_{3m} \rho_w g V_c h_i h_b \epsilon w}{k_{max}} \left(\frac{\cos \alpha}{\sin \alpha} - \frac{\cos \alpha}{\sin \alpha} \right) \quad (64)$$

$$W_4 = \frac{p_{4m} \rho_w g V_c h_i h_b \epsilon w}{k_{max} \sin \alpha} \quad (65)$$

k_{max} maximum permeability
 p_m average pore pressure on a surface
 ϵ volume strain

The grain forces for saturated sand (Miedema, 2014):

$$K_1 = \frac{W_2 \sin \lambda + W_1 \sin(\alpha + \beta + \lambda)}{\sin(\alpha + \beta + \lambda + \varphi)} \quad (66)$$

$$K_2 = \frac{W_2 \sin(\alpha + \beta + \varphi) + W_1 \sin \varphi}{\sin(\alpha + \beta + \lambda + \varphi)} \quad (67)$$

$$K_3 = \frac{-W_2 \sin(\alpha + \delta_e + \theta) + K_2 \sin(\alpha + \delta_e - \theta - \lambda)}{\sin(\alpha + \delta_e + \varphi)} + \frac{W_3 \sin(\alpha + \delta_e) + W_4 \sin(\delta_e)}{\sin(\alpha + \delta_e + \varphi)} \quad (68)$$

$$K_4 = \frac{-W_2 \sin(\theta + \varphi) + K_2 \sin(\theta + \lambda + \varphi)}{\sin(\alpha + \delta_e + \varphi)} + \frac{W_3 \sin \varphi + W_4 \sin(\alpha + \varphi)}{\sin(\alpha + \delta_e + \varphi)} \quad (69)$$

Appendix V: Scaling laws

Scaling laws are used to convert the results about the model to information about the prototype. In fluid mechanics dimensionless numbers are used for scaling, these numbers need to be constant for both the model as the prototype.

V.1. Reynolds scaling

The Reynolds number is the ratio of viscous forces to the inertia forces, as given in Equation 1 (White F. , 2011)).

$$Re = \frac{VD}{\nu} \quad (70)$$

Re	Reynolds number [-]
V	flow velocity [m/s]
D	diameter [m]
ν	kinematic viscosity of the fluid [m ² /s]

The Reynolds number can only be ignored in high velocity regimes. Reynolds scaling is used when the viscous and inertia forces are leading in the flow. This ratio should be equal for both the prototype and the model. One difficulty concerning Reynolds scaling is the scale factor for the hydrodynamic force α_F equals to unity. This means that the forces for the prototype and the model should be equal, which is not always possible.

V.2. Froude scaling

The Froude number is the ratio between inertia forces and gravity forces, as given in Equation 2 (White F. , 2011)

$$Fr = \frac{V}{\sqrt{gL}} \quad (71)$$

Fr	Froude number [-]
V	velocity [m/s]
g	gravitational constant [m/s ²]
L	length [m]

Gravity forces play a role in situations with a free water surface. The Froude number could be used to make a velocity dimensionless.

V.3. Peclet scaling

The Peclet number is the ratio between the advective transport rate and the diffusive transport rate. It can be defined in different ways. In Equation 3 it has been defined as the ratio between the velocity and the porosity (Huysmans & Dassargues, 2005).

$$Pe = \frac{V_D L}{n_e D_L} \quad (72)$$

Pe	Peclet number [-]
V_D	Darcy velocity [m/s]
L	reference length [m]
n_e	effective porosity for advection [m/s]
D_L	longitudinal hydrodynamic dispersion coefficient [m]

The Darcy velocity represents the water volume that flows through a cross sectional area of porous media per unit time. The effective porosity is defined as the fractional volume of pores that are connected. (Woesnner & Pieter, 2020). The evolution of the nominator is dominated by convection when the Peclet number is larger than one. If the Peclet number is lower than one, it will be dominated by diffusion (Hirsch, 2007).

Appendix VI: Overview of the experiment

Date	Time	Name test	Name data file	Chain link diameter [mm]	Velocity [m/s]	Angle of attack [°]	Penetration depth [mm]	Density	Grain size [mm]	Number of chains	Remarks
"	13:57	Test 19a	two chains test_1_1	6	0,3	90	0	Loose	0,17	2	
"	-	Test 19b	-	6	0,3	90	0	Loose	0,17	2	No data
"	14:28	Test 19c	two chains test_2_1	6	0,3	90	0	Loose	0,17	2	
"	14:59	Test 18a	one chain test_1_1	6	0,3	90	0	Loose	0,17	1	
"	15:08	Test 18b	one chain test_2_1	6	0,3	90	0	Loose	0,17	1	
"	16:44	Test 10a	ten mm test_1_1	10	0,3	90	0	Loose	0,17	3	
"	16:54	Test 10b	ten mm test_2_1	10	0,3	90	0	Loose	0,17	3	
Friday 29-4	9:23	Test 10c	ten mm test_3_1	10	0,1	90	0	Loose	0,17	3	
"	10:04	Test 10d	ten mm test_4_1	10	0,1	90	0	Loose	0,17	3	
"	10:07	Test 10e	ten mm test_5_1	10	0,1	90	0	Loose	0,17	3	
"	10:18	Test 10f	ten mm test_6_1	10	0,6	90	0	Loose	0,17	3	
"	11:19	Test 10g	ten mm test_7_1	10	0,6	90	0	Loose	0,17	3	
"	11:22	Test 10h	ten mm test_8_1	10	0,3	60	0	Loose	0,17	3	
"	11:31	Test 10i	ten mm test_9_1	10	0,3	60	0	Loose	0,17	3	
"	12:00	Test 10j	ten mm test_10_1	10	0,3	30	0	Loose	0,17	3	
"	12:03	Test 10k	ten mm test_11_1	10	0,3	30	0	Loose	0,17	3	
Tuesday 3-5	10:34	Test 12a	sixteen mm test_1_1	16	0,3	90	0	Loose	0,17	3	
"	10:43	Test 12b	sixteen mm test_2_1	16	0,3	90	0	Loose	0,17	3	
"	11:03	Test 12c	sixteen mm test_3_1	16	0,1	90	0	Loose	0,17	3	
"	11:11	Test 12d	sixteen mm test_4_1	16	0,1	90	0	Loose	0,17	3	
"	11:27	Test 12e	sixteen mm test_5_1	16	0,1	90	0	Loose	0,17	3	
"	12:12	Test 12f	sixteen mm test_6_1	16	0,6	90	0	Loose	0,17	3	
"	12:19	Test 12g	sixteen mm test_7_1	16	0,6	90	0	Loose	0,17	3	
"	13:29	Test 12h	sixteen mm test_8_1	16	0,3	60	0	Loose	0,17	3	
"	14:06	Test 12i	sixteen mm test_9_1	16	0,3	60	0	Loose	0,17	3	
"	14:09	Test 12j	sixteen mm test_10_1	16	0,3	30	0	Loose	0,17	3	
"	14:21	Test 12k	sixteen mm test_11_1	16	0,3	30	0	Loose	0,17	3	

Date	Time	Name test	Name data file	Chain link diameter [mm]	Velocity [m/s]	Angle of attack [°]	Penetration depth [mm]	Density	Grain size [mm]	Number of chains	Remarks
Wednesday 4-5	10:33	Test 23a	no chain test_1_1	-	0,3	90	0	Loose	0,17	0	
"	10:39	Test 23b	no chain test_2_1	-	0,3	90	0	Loose	0,17	0	
"	10:47	Test 23c	no chain test_3_1	-	0,1	90	0	Loose	0,17	0	
"	10:52	Test 23d	no chain test_4_1	-	0,1	90	0	Loose	0,17	0	
"	10:59	Test 23e	no chain test_5_1	-	0,6	90	0	Loose	0,17	0	
"	11:42	Test 23f	no chain test_6_1	-	0,6	90	0	Loose	0,17	0	
"	11:44	Test 23g	no chain test_7_1	-	0,3	60	0	Loose	0,17	0	
"	11:50	Test 23h	no chain test_8_1	-	0,3	60	0	Loose	0,17	0	
"	12:11	Test 23i	no chain test_9_1	-	0,3	30	0	Loose	0,17	0	
"	12:17	Test 23j	no chain test_10_1	-	0,3	30	0	Loose	0,17	0	
Wednesday 11-5	10:18	Test 22a	coarse sand test_1_1	6	0,3	60	0	Loose	0,26	3	
"	10:33	Test 22b	coarse sand test_2_1	6	0,3	60	0	Loose	0,26	3	
"	11:16	Test 22c	coarse sand test_3_1	6	0,3	30	0	Loose	0,26	3	
"	11:25	Test 22d	coarse sand test_4_1	6	0,3	30	0	Loose	0,26	3	
"	11:53	Test 22e	coarse sand test_5_1	6	0,3	90	0	Loose	0,26	3	Velocity not set correctly
"	12:03	Test 22f	coarse sand test_6_1	6	0,26	90	0	Loose	0,26	3	
"	12:14	Test 22g	coarse sand test_7_1	6	0,3	90	0	Loose	0,26	3	
"	13:13	Test 22h	coarse sand test_8_1	6	0,1	90	0	Loose	0,26	3	
"	13:21	Test 22i	coarse sand test_9_1	6	0,1	90	0	Loose	0,26	3	
"	13:32	Test 22j	coarse sand test_10_1	6	0,6	90	0	Loose	0,26	3	Forces very low
"	13:45	Test 22k	coarse sand test_11_1	6	0,6	90	0	Loose	0,26	3	"

Date	Time	Name test	Name data file	Chain link diameter [mm]	Velocity [m/s]	Angle of attack [°]	Penetration depth [mm]	Density	Grain size [mm]	Number of chains	Remarks
Thursday 12-5	10:10	Test 22i	coarse sand test_12_1	-	0,3	90	0	Loose	0,26	3	
"	10:16	Test 22m	coarse sand test_13_1	-	0,3	90	0	Loose	0,26	3	
"	11:12	Test 22n	coarse sand test_14_1	-	0,3	90	20	Loose	0,26	3	
"	11:19	Test 22o	coarse sand test_15_1	-	0,3	90	20	Loose	0,26	3	
"	12:24	Test 22p	coarse sand test_16_1	6	0,3	90	20	Loose	0,26	3	
"	12:31	Test 22q	coarse sand test_16_1	6	0,3	90	20	Loose	0,26	3	
"	14:19	Test 22r	coarse sand test_17_1	6	0,3	90	0 (20)	Dense	0,26	3	
"	14:32	Test 22s	coarse sand test_19_1	6	0,3	90	0 (20)	Dense	0,26	3	
"	15:37	Test 22t	coarse sand test_20_1	-	0,3	90	0 (20)	Dense	0,26	3	
"	15:45	Test 22u	coarse sand test_21_1	-	0,3	90	0 (20)	Dense	0,26	3	
Thursday 30-6	9:36	Test 10i	ten mm test_12_1	10	0,3	90	0	Loose	0,17	3	Repetition previous tests
"	10:27	Test 10m	ten mm test_13_1	10	0,3	90	20	Loose	0,17	3	"
"	10:49	Test 10n	ten mm test_14_1	10	0,3	90	20	Loose	0,17	3	"
"	13:30	Test 17e	dense test_5_1	6	0,3	90	0 (20)	Dense	0,17	3	" , 13 cm
"	13:48	Test 17f	dense test_6_1	6	0,3	90	0 (20)	Dense	0,17	3	" , 13 cm
"	14:45	Test 17g	dense test_7_1	6	0,3	90	0 (20)	Dense	0,17	3	" , 13,5 cm
"	14:54	Test 17h	dense test_8_1	6	0,6	90	0 (20)	Dense	0,17	3	" , 13,5 cm
"	15:05	Test 17i	dense test_9_1	6	0,1	90	0 (20)	Dense	0,17	3	" , 13,5 cm

Appendix VII: Technical data sand

	M31	M32	M34	
D50	370	260	170	µm
AFS	45	50	75	
> 1000 µm	1			%
> 710 µm	5			%
> 500 µm	25			%
> 355 µm	53	7		%
> 250 µm	85	57	3	%
> 180 µm	98	93	30	%
> 125 µm			91	%
< 63 µm	sporen	≤ 0,1	≤ 0,3	%
soortelijk gewicht	2,65	2,65	2,65	kg/dm ³
stortgewicht	1,6	1,5	1,4	kg/dm ³
hardheid	7	7	7	Mohs
pH	7	7	7	
gloeiverlies	0,15	0,15	0,15	%
kleur	L*	70	70	Minolta CM-3610 D65/10°
	a*	2,63	2,79	
	b*	9,58	9,82	
		72	72	
		1,93	1,93	
		7,76	7,76	

CHEMISCHE SAMENSTELLING (XRF) %

	M31	M32	M34
SiO ₂	99,5	99,5	99,0
Fe ₂ O ₃	0,04	0,03	0,07
Al ₂ O ₃	0,20	0,20	0,60
TiO ₂	0,03	0,03	0,06
K ₂ O	0,03	0,05	0,30
CaO	0,01	0,01	0,02

Appendix VIII: Technical data force sensor

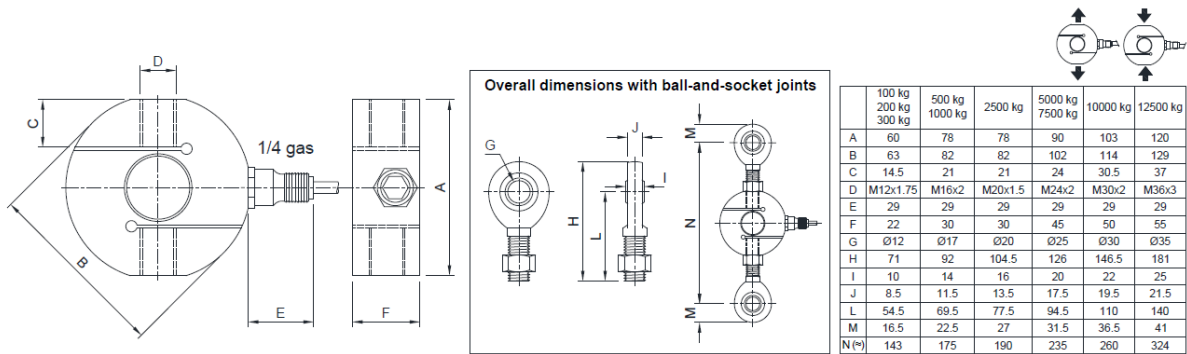
Capacity from 100 kg to 12500 kg



- 17-4 PH STAINLESS STEEL
- COMBINED ERROR $\leq \pm 0.02\%$
- PROTECTION CLASS IP68

CAPACITY	kg	ACCURACY CLASS				NET WEIGHT (kg)	CODE
100		C3				0.7	CTL100

DIMENSIONS (mm)



Appendix IX: Drawings of the setup

These drawings are made by André van den Bosch.

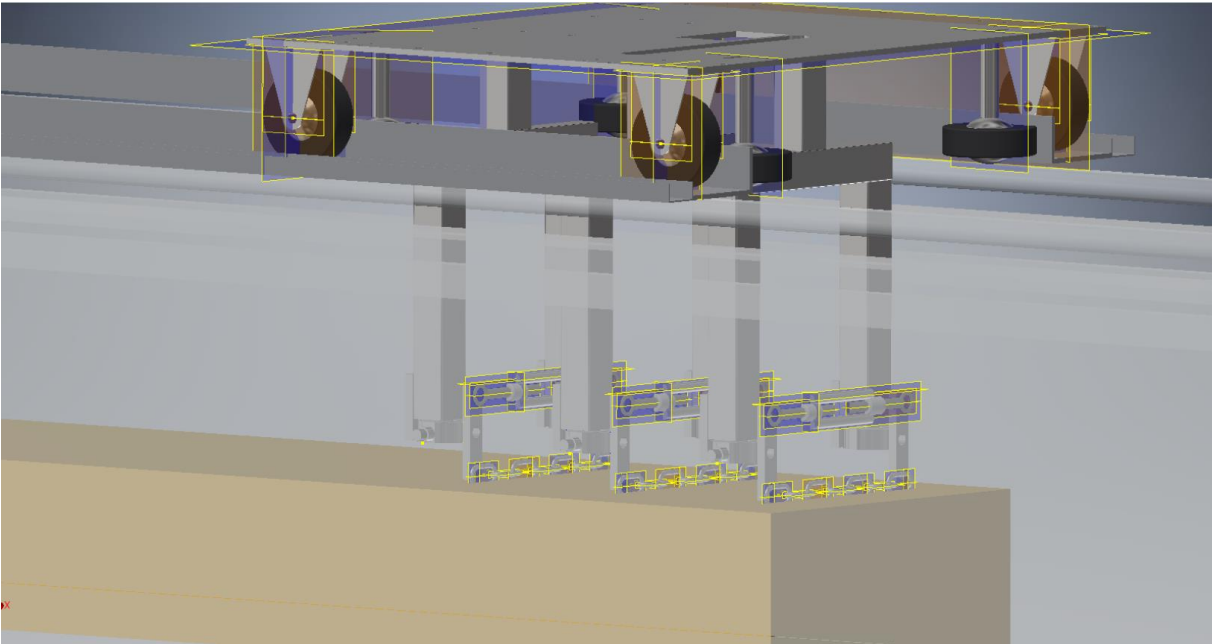


Figure 82: Overview of the setup (drawing by B.A. van den Bosch)



Figure 83: Chain holder (drawing by B.A. van den Bosch)

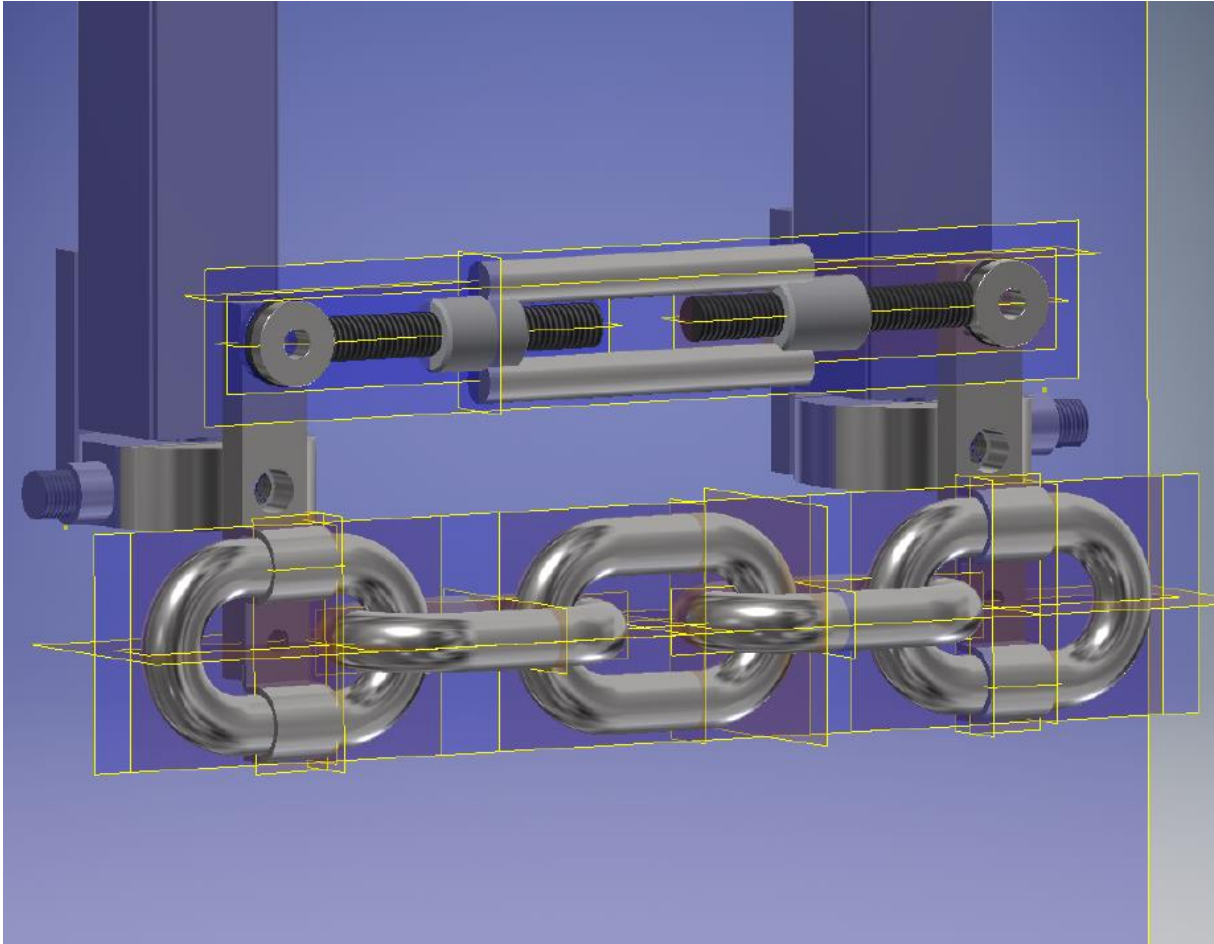


Figure 84: Chain connected to the chain holder (drawing by B.A. van den Bosch)

Appendix X: Additional plots front chain

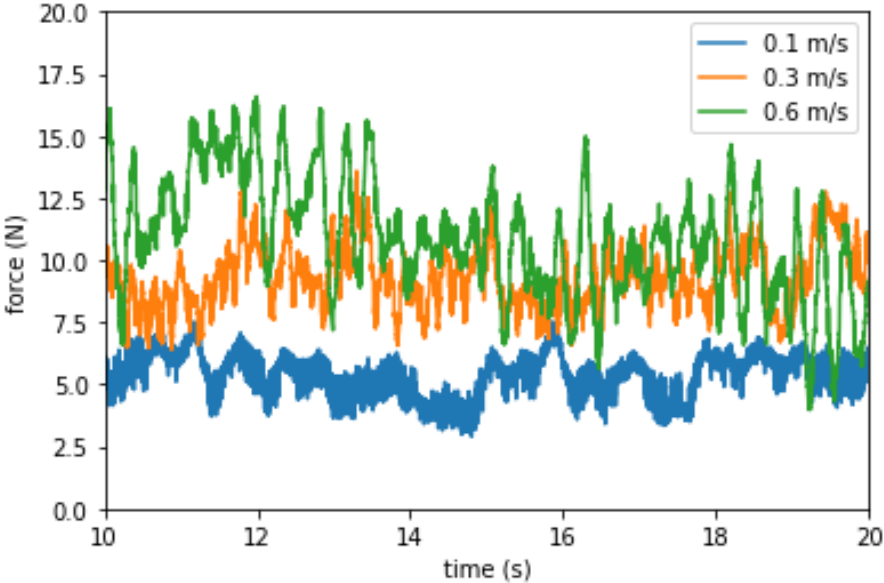


Figure 85: Figure 9: Force versus time for different velocities in loose sand

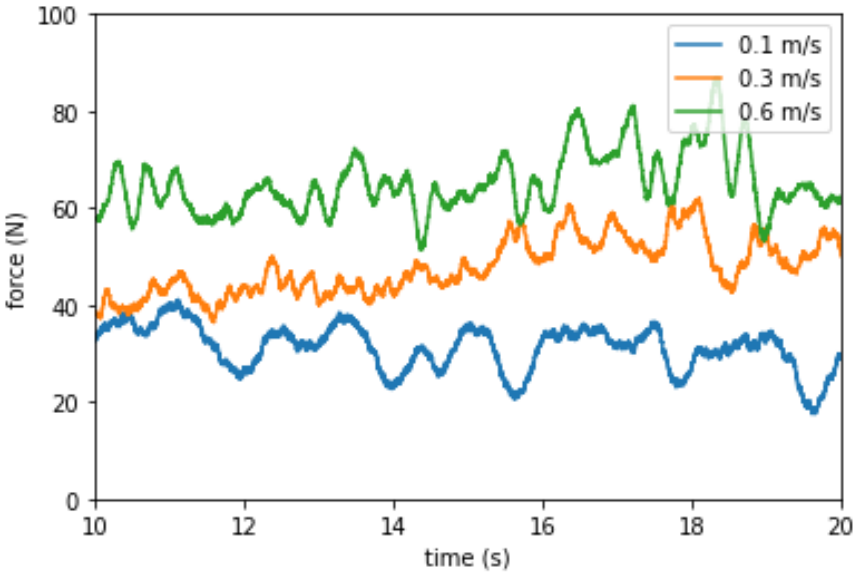


Figure 86: Force versus time for different velocities in dense sand

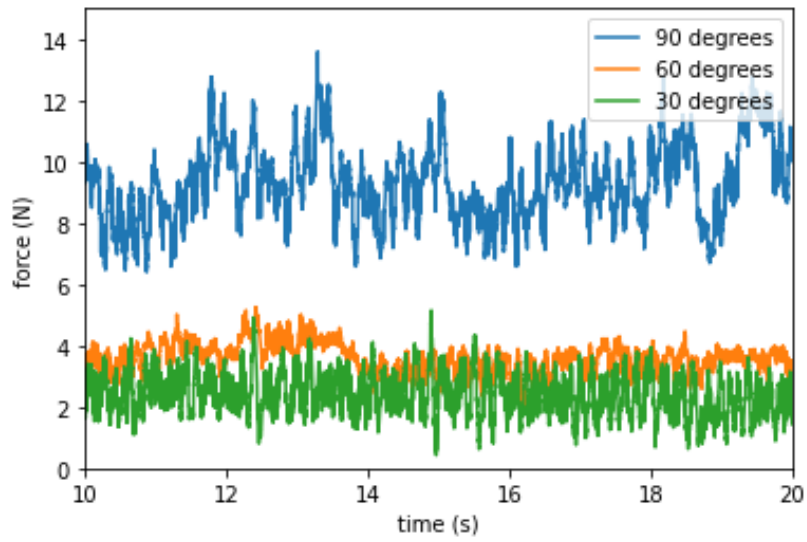


Figure 87: Figure 9: Force versus time for different angles of attack

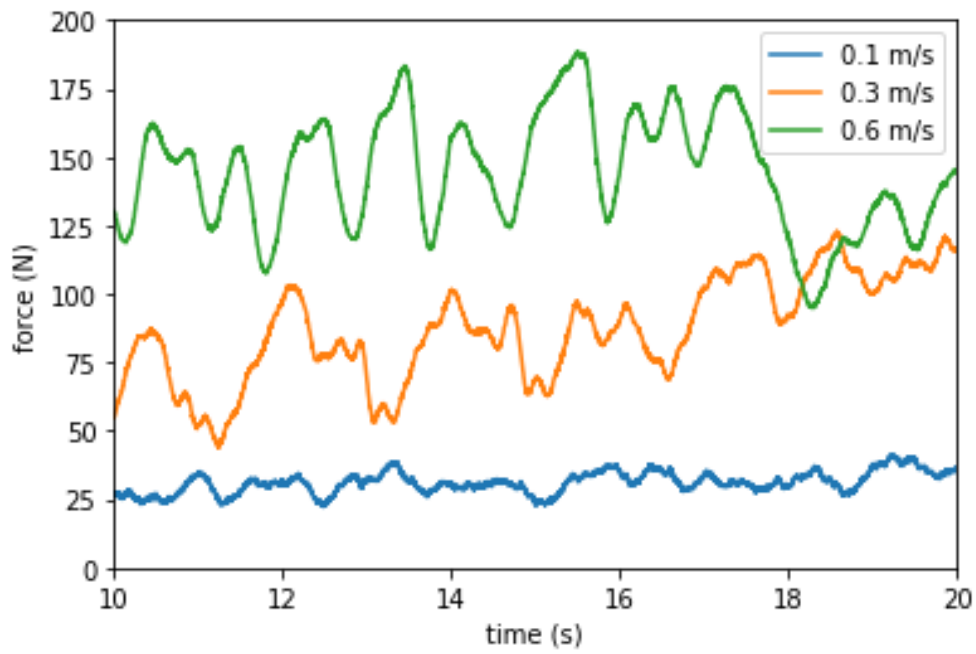


Figure 88: Force versus time for the 16 mm chain

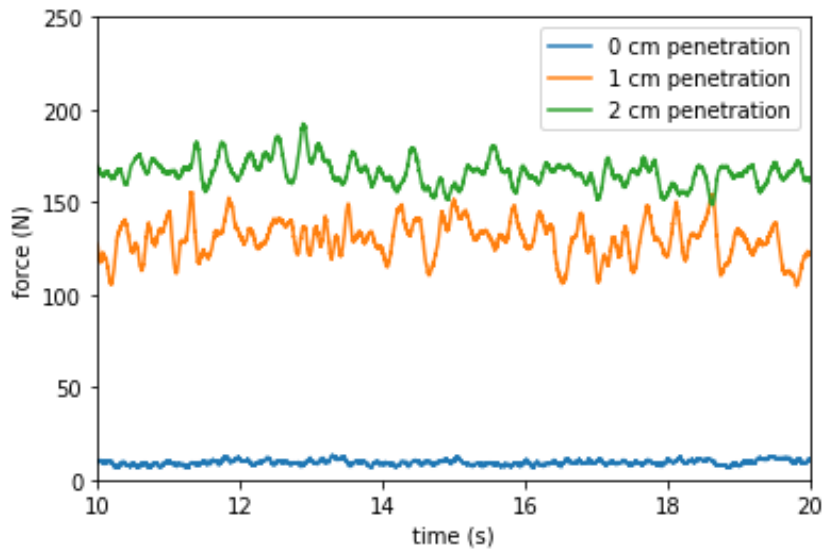


Figure 89: Force versus time for additional penetration depth

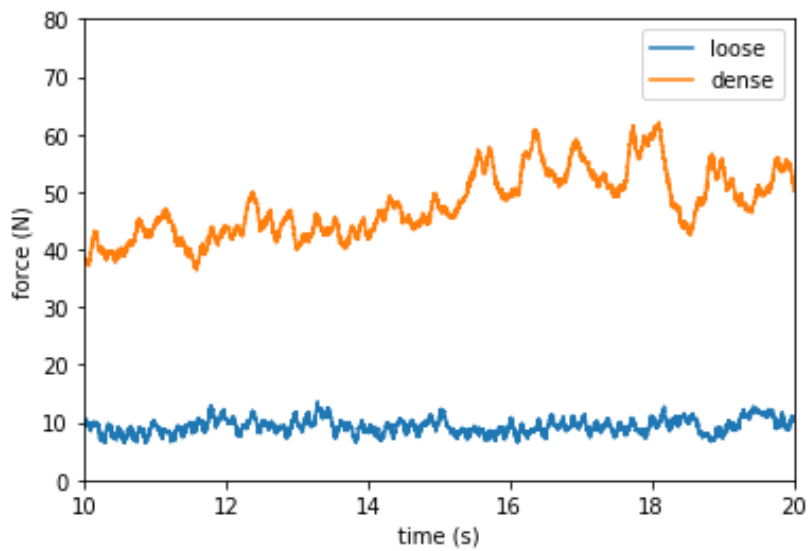


Figure 90: Loose versus dense for the fine grain

In the coarse grain the forces are higher for both densities, the relative increase is less compared with the fine grain, about 2.3 times.

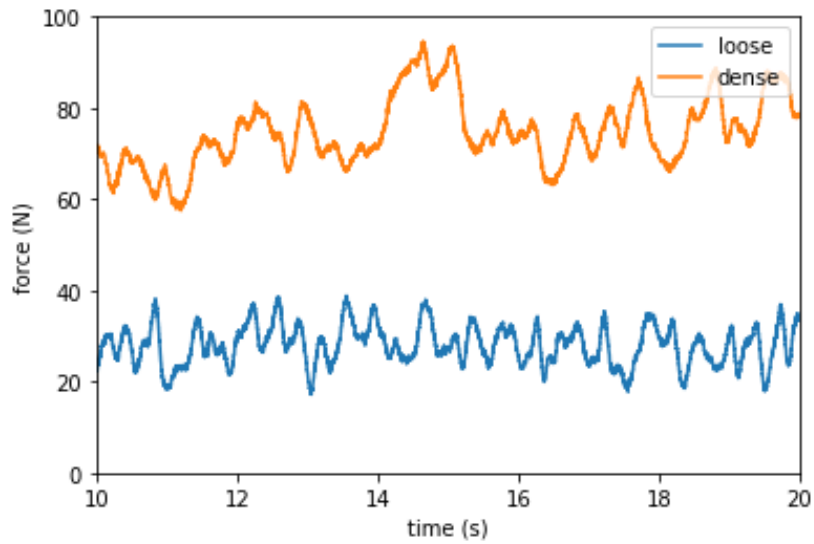


Figure 91: Loose versus dense for the coarse grain

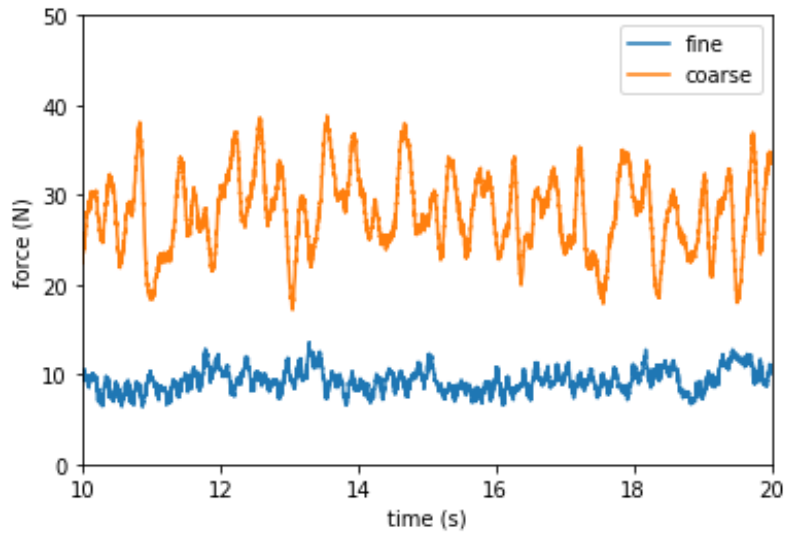


Figure 92: Fine versus coarse grain for loose sand

After densifying the force increases for both grain sizes. The absolute difference seems to remain the same.

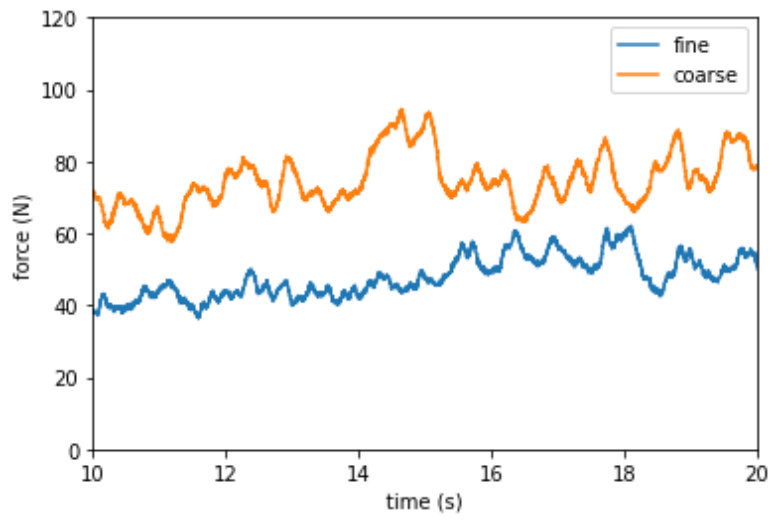


Figure 93: Fine versus coarse grain for dense sand

Appendix XI: Consolidation and confining pressure calculations

Parameter	Symbol	Unit	6 mm	16 mm
	c_v^*u/h	-	0.088640695	0.03775437
Consolidation coefficient	c_v	-	0.01019368	0.01019368
Characteristic time	t	s	0.115	0.27
Penetration depth	h	m	0.0115	0.027
Towing velocity	u	m/s	0.1	0.1
	c_v^*t/h^2	-	8.864069494	3.775437007

Table 14: Minimum value of the consolidation coefficient for both chain link diameters

Parameter	Symbol	Unit	6 mm	16 mm
	c_v^*u/h	-	0.886406949	0.377543701
Consolidation coefficient	c_v	-	0.101936799	0.101936799
Characteristic time	t	s	0.115	0.27
Penetration depth	h	m	0.0115	0.027
Towing velocity	u	m/s	0.1	0.1
	c_v^*t/h^2	-	88.64069494	37.75437007

Table 15: Maximum value of the consolidation coefficient for both chain link diameters

Parameter	Symbol	Unit	Minimum	Maximum
Density	ρ	kg/m ³	1700	1961.5
Gravitational constant	g	m/s ²	9.81	9.81
Penetration depth	h_i	m	0.0115	0.0315
Confining pressure	p'	Pa	191.7855	606.1329225

Table 16: Minimum and maximum value for the confining pressure